

South Dakota State University

## Open PRAIRIE: Open Public Research Access Institutional Repository and Information Exchange

---

Electronic Theses and Dissertations

---


2019

# Classification of North Africa for Use as an Extended Pseudo Invariant Calibration Sites (Epics) for Radiometric Calibration and Stability Monitoring of Optical Satellite Sensors

Mahesh Shrestha

*South Dakota State University*

Follow this and additional works at: <https://openprairie.sdstate.edu/etd>

 Part of the [Electrical and Computer Engineering Commons](#), [Physical and Environmental Geography Commons](#), and the [Remote Sensing Commons](#)

---

### Recommended Citation

Shrestha, Mahesh, "Classification of North Africa for Use as an Extended Pseudo Invariant Calibration Sites (Epics) for Radiometric Calibration and Stability Monitoring of Optical Satellite Sensors" (2019). *Electronic Theses and Dissertations*. 3404.  
<https://openprairie.sdstate.edu/etd/3404>

This Dissertation - Open Access is brought to you for free and open access by Open PRAIRIE: Open Public Research Access Institutional Repository and Information Exchange. It has been accepted for inclusion in Electronic Theses and Dissertations by an authorized administrator of Open PRAIRIE: Open Public Research Access Institutional Repository and Information Exchange. For more information, please contact [michael.biondo@sdstate.edu](mailto:michael.biondo@sdstate.edu).

CLASSIFICATION OF NORTH AFRICA FOR USE AS AN EXTENDED PSEUDO  
INVARIANT CALIBRATION SITES (EPICS) FOR RADIOMETRIC CALIBRATION  
AND STABILITY MONITORING OF OPTICAL SATELLITE SENSORS

BY

MAHESH SHRESTHA

A dissertation submitted in partial fulfillment of the requirements for the

Doctor of Philosophy

Major in Geospatial Science and Engineering

Specialization in Remote Sensing Engineering

South Dakota State University

2019

CLASSIFICATION OF NORTH AFRICA FOR USE AS AN EXTENDED PSEUDO  
INVARIANT CALIBRATION SITES (EPICS) FOR RADIOMETRIC CALIBRATION  
AND STABILITY MONITORING OF OPTICAL SATELLITE SENSORS

MAHESH SHRESTHA

This dissertation is approved as a creditable and independent investigation by a candidate for the doctor of philosophy in Geospatial Science and Engineering degree and is acceptable for meeting the thesis requirements for this degree. Acceptance of this thesis dissertation does not imply that the conclusions reached by the candidate are necessarily the conclusions of the major department.

— Dennis Helder, PhD  
Dissertation Major Advisor

Date

Larry Leigh  
Dissertation Advisor

Date

George Hamer, PhD  
Acting Head, Department of Electrical  
Engineering and Computer Science

Date

Dean, Graduate School

Date

I dedicate this dissertation to my father Madan Shrestha and mother Bishnu Shrestha.



## ACKNOWLEDGEMENTS

First and foremost, I would like to express my sincere thank my major advisor, Dr. Dennis Helder, who introduce me in the world of radiometry. I am indebted for his continuous guidance, support, and encouragement for this research work. His mentorship and guidance over these last three years has helped me grow significantly both as a professional and a person.

I am also very grateful to my advisor Mr. Larry Leigh for his invaluable and continuous guidance for this work. He always helped to solve some of the most challenging problems in the field of satellite sensor calibration. I attribute my growth as a researcher and scientist to him. His confidence on me and constant support were the key factors that always kept me motivating for my work.

Both Mr. Leigh and Dr. Helder have always taken great care of me and I would give them most of the credit for becoming the kind of researcher and scientist I am today.

I would also like to thank my current and former PhD advisor committee members, Dr. Thomas R. Loveland (USGS/EROS), Dr. Michael Wimberly (University of Oklahoma), Dr. Rasmus Houborg (Planet Labs, CA) and graduate faculty representatives Dr. Michael Gonda and Dr. Larry Holler for helping thorough the dissertation process.

Special thanks to Dr. Thomas R. Loveland for guiding us regarding landcover classification of North Africa. I would also like to thank Tim Ruggles for his tremendous help in improving my journal writing and providing valuable feedbacks. I am also grateful to Mr. Nahid Hasan for helping me during my research work.

I am very thankful to Dr. Cibeles Teixeira Pinto and Mrs. Morakot Kaewmanee for their thoughtful comments and suggestions during weekly meeting. Similarly, I would also like to acknowledge SDSU Image Processing Lab crew, past and present, for improving me by giving valuable feedbacks and for creating such a wonderful learning environment.

I am very grateful to my girlfriend Abhilasha Bajracharya for her continuous support and motivation and always being there for me during this endeavor.

Finally, I would like to express my deepest gratitude to my brother Manoj Shrestha, sister-in-law Laxmi Shrestha, Rojesh Maharjan, Lok Raj Joshi, Sudeep Ghimire, and Tirth Uprety for their constant inspiration and support.

This research was funded by NASA (grant number NNX15AP36A) and USGS EROS (grant number G14AC00370).

## TABLE OF CONTENTS

LIST OF TABLES .....	x
LIST OF FIGURES .....	xi
ABSTRACT.....	xvi
 <b>Chapter 1: Classification of North Africa for Use as an Extended Pseudo Invariant Calibration Sites (EPICS) for Radiometric Calibration and Stability Monitoring of Optical Satellite Sensors (Published in Remote Sensing Journal)</b>	
<b>1. Introduction.....</b>	<b>1</b>
1.1 Historical Approach for Identifying Candidate PICS .....	2
1.2 Limitations of using traditional PICS.....	2
1.3 Previous Classification of North Africa .....	3
1.4 Current Approach for Extending PICS .....	3
<b>2. Materials and Methods.....</b>	<b>4</b>
2.1. Google Earth Engine (GEE).....	4
2.2. SDSU Derived Data Product.....	4
2.3 Mosaic Image of North Africa .....	5
2.4 Classification of North African Land Cover .....	5
<b>3. Results and Validation.....</b>	<b>7</b>
3.1 Classification of North Africa .....	7
3.2. Spatial Uncertainty of Clusters .....	8
3.3. Cluster Spectral Signatures .....	9
3.4. Comparison of Traditional PICS and Cluster 13 behaviour .....	10
3.5. Validation of North African Classification .....	11
<b>4. Discussion.....</b>	<b>12</b>
4.1 Long Term Monitoring of Sensor Radiometric Stability .....	14
4.2. Hyperspectral Data Availability for Cross Calibration .....	15
<b>5. Conclusions.....</b>	<b>16</b>
<b>References .....</b>	<b>17</b>

**Chapter 2: Derivation of Hyperspectral Profile of North Africa Land Cover Types for Use in Sensor Calibration (Under Review Remote Sensing Journal)**

<b>1. Introduction.....</b>	<b>20</b>
1.1 Limitation of Region of Interest (ROI) Based Cross-Calibration Approach .....	21
1.2 Proposed Solution to the ROI Based Cross-Calibration Approach.....	21
1.3 EPICS based Absolute Calibration Model .....	22
1.4 Hyperion Sensor Description and Previous Radiometric Calibration Performance	23
<b>2. Methodology .....</b>	<b>23</b>
2.1 Hyperion Acquisitions Over North Africa .....	23
2.2 Collection of Hyperspectral Data for Cluster 13.....	25
2.3 Hyperspectral Data for Cluster 13.....	26
2.3.1. Data Filtering .....	27
2.3.2. Corrections to Hyperspectral Data .....	27
2.3.2.1. Drift correction and Calibration Gain/Bias Application.....	28
2.3.2.2. Four Angle Bidirectional Reflectance Distribution Function (BRDF) Correction .....	28
2.3.2.3 Estimation of a Representative Cluster 13 Hyperspectral Profile .....	29
<b>3. Results .....</b>	<b>30</b>
3.1 Pre-processing of Hyperspectral Profiles of Cluster 13 .....	30
3.2 Collection of Hyperspectral Profiles of Cluster 13 .....	31
3.3 Investigation of Relative Change of HyperSpectral Profiles of Cluster 13 .....	32
3.4 Estimation of a Representative Hyperspectral Profile of Cluster 13 .....	33
3.6 Estimation of a Representative Hyperspectral Profile for Different Reflectance Clusters.....	34
3.7 Validation of the Estimated Hyperspectral Profile for Cluster 13 .....	35
3.7.1 Hyperspectral Domain.....	35
3.7.2 Multispectral Domain.....	37
<b>4. Discussion.....</b>	<b>39</b>
<b>5. Conclusions.....</b>	<b>43</b>
<b>Appendix A .....</b>	<b>44</b>
<b>References .....</b>	<b>760</b>

<b>1. Introduction.....</b>	<b>55</b>
1.1. Pseudo-Invariant Calibration Sites (PICS).....	56
1.2. Cross-Calibration of Optical Satellite Sensors.....	56
1.3. Current Limitation of Cross Calibration .....	56
1.4. Current Approach of Cluster-Based Cross Calibration.....	57
<b>2. Data and Methods .....</b>	<b>58</b>
2.1. Sensor Description .....	58
2.1.1. Landsat 8 OLI.....	58
2.1.2. Sentinel 2A MSI.....	58
2.2. Site and Cluster Selection .....	59
2.2.1. Libya 4 Test Site.....	59
2.2.2. North African Cluster 13 .....	59
2.3. Scene Pairs .....	60
2.4. Conversion to TOA Reflectance .....	60
2.4.1. Spectral Band Adjustment Factor (SBAF) .....	61
2.4.2. Bidirectional Reflection Distribution Function (BRDF) .....	61
<b>3. Results .....</b>	<b>63</b>
3.1. Coincident and Near-Coincident Acquisitions.....	63
3.2. SBAF for Libya 4 CNES ROI and Cluster 13 .....	65
3.3. Comparison of TOA Reflectance of Landsat 8 and Sentinel 2A .....	66
3.4. Comparison of Cross-Calibration Gain ratios from ROI-Based and Cluster-Based Approach .....	68
<b>4. Discussion.....</b>	<b>71</b>
<b>5. Conclusions.....</b>	<b>74</b>
<b>Appendix A .....</b>	<b>75</b>
<b>References .....</b>	<b>76</b>
<b>Chapter4: Conclusions.....</b>	<b>80</b>

## LIST OF TABLES

<b>Table No.</b>	<b>Title</b>	<b>Page</b>
<b>Chapter 1</b>		
Table 1.	Salient characteristics of Landsat 8 Operational Land Imager (OLI).	4
Table 2.	Cluster spatial uncertainty, by band.	9
Table 3.	Comparison of K-Means Cluster 13 Statistics and Scene-Based Cluster 13 Statistics.	12
<b>Chapter 3</b>		
Table 1.	Salient features of Landsat 8 OLI and Sentinel 2A MSI.	58
Table 2.	Coincident dates between Landsat 8 OLI and Sentinel 3A MSI for Libya 4 CNES ROI. Bold are cloud-free images.	63
Table 3.	Cloud-free Coincident acquisitions between Landsat 8 OLI and Sentinel 2A for Cluster 13.	64
Table 4.	Near-coincident data between Landsat 8 OLI and Sentinel 2A MSI for Libya 4 CNES ROI.	65

## LIST OF FIGURES

<b>Figure No.</b>	<b>Title</b>	<b>Page</b>
<b>Chapter 1</b>		
Figure 1.	SDSU Data Tile Layers Derived from Google Earth Engine.	5
Figure 2.	North Africa Mosaic After Filtering Temporally Unstable Pixels.	7
Figure 3.	K-Means Classification of North Africa to 5% Spatial Uncertainty	8
Figure 4.	Number of pixels in each North African cluster.	8
Figure 5.	Spectral Signature of Clusters, by Band.	9
Figure 6.	Comparison between traditional PICS (Libya 4) and Cluster 13 behavior. The figure on the left and right show the trending of Libya 4 and Cluster 13, since launch to August 2018, using Landsat 8 OLI respectively.	10
Figure 7.	Comparison between the temporal mean and its standard deviation between traditional PICS (Libya 4 CNES ROI) and Cluster 13. Red and Blue symbol represent the temporal mean of Libya 4 CNES ROI and Cluster 13 respectively.	11
Figure 8.	Lifetime OLI TOA Reflectance of Cluster 13 using Landsat 7, No BRDF Correction.	12
Figure 9.	Cluster 13 coverage over North Africa and corresponding WRS-2 paths and rows	15
Figure 10.	Cluster 13 Extent Across North Africa with Corresponding Hyperion Coverage.	16

## Chapter 2

Figure 1.	K-Means Classification of North Africa to 5% Spatial Uncertainty.	22
Figure 2.	Hyperion coverage over North Africa.	24
Figure 3.	Number of hyperspectral spectra over different North African clusters.	25
Figure 4.	Extent of cluster 13 over North Africa. Blue color represents cluster 13 pixels. Black rectangle boxed represent the regions used for validation.	26
Figure 5.	Number of hyperspectral spectra corresponding to each WRS-2 Paths and Row of Cluster 13.	26
Figure 6.	Cluster 13 Binary Masks: a) Path/ Row 181/40 (Libya 4), b) Path/ Row 179/41 (Egypt 1) c) Path/ Row 182/42 d) Path/Row 198/47. Black pixels represent Cluster 13 pixels from the Hyperion images.	27
Figure 7.	Corrections applied to the hyperspectral profile. Red curve represents the original spectrum and blue represents the corrected hyperspectral data.	31
Figure 8.	Hyperspectral data of cluster 13. Green represents the spectra from EO-1's launch to 2007. Blue represents the spectra from 2008 through 2015 and red represent the spectral from 2016 to its decommissioning in March 2017.	32
Figure 9.	Absolute difference between the individual normalized hyperspectral data with the mean Cluster 13 hyperspectral data.	33



Figure 10.	Estimated representative hyperspectral profile of Cluster 13 and its resultant uncertainty.	34
Figure 11.	Estimated representative hyperspectral profile of Cluster 4 and its resultant uncertainty.	34
Figure 12.	Estimated representative hyperspectral profile of Cluster 1 and its resultant uncertainty.	35
Figure 13.	Validation of hyperspectral spectrum of Cluster 13.	36
Figure 14.	Validation of hyperspectral spectrum of Cluster 4.	36
Figure 15.	Validation of hyperspectral spectrum of Cluster 1.	37
Figure 16.	Cluster 13 binary masks (a) Sentinel 2A MSI Libya 4 (b) Sentinel 2A MSI Egypt 1 (c) Landsat 7 Libya 4 (d) Landsat 7 Egypt 1. Black color pixel represents the Cluster 13 pixels.	38
Figure 17.	Plot of simulated multispectral SBAF / Multispectral TOA Reflectance Ratio Comparison (1 sigma).	39
Figure 18.	Comparison of the hyperspectral profile of different clusters with its temporal uncertainty (1-sigma). The solid line represents a representative hyperspectral profile of a cluster and its corresponding temporal uncertainty is represented by the dotted line of the same color.	41
Figure 19	Comparison of resultant standard deviation (1 sigma) of clusters 13 and 4. The blue and red solid lines represent the resultant standard deviation of clusters 13 and 4.	41
Figure 20	Comparison of temporal uncertainty of all 19 clusters of North Africa.	43

### Chapter 3

Figure 1.	Shrestha's K-means classification of North Africa to 5% spatial uncertainty.	57
Figure 2.	Libya 4 image by Landsat 8 OLI (larger rectangle) and Sentinel 2A MSI (smaller rectangle). The red solid rectangle represents Libya 4 Centre National d'Etudes Spatiales (CNES) region of interest (ROI).	59
Figure 3.	Extent Cluster 13 across North Africa. Blue color represents cluster 13 pixels.	60
Figure 4.	The intersection of Cluster 13, Landsat 8 OLI, and Sentinel 2A MSI. Red boundaries represent the Cluster 13 boundaries across North Africa. White and blue rectangular boxes represent Landsat 8 OLI and Sentinel 2A MSI footprints, respectively.	64
Figure 5.	Intersection of Cluster 13 and Libya 4 (a) Landsat 8 OLI (b) Sentinel 2A MSI. Black pixels represent the cloud-free Cluster 13 pixels of Libya 4.	65
Figure 6.	Spectral band adjustment factor (SBAF) for Sentinel 2A MSI for Libya 4 CNES ROI and Cluster 13 (Uncertainty bars, $k = 2$ ).	66
Figure 7.	Comparison of Landsat OLI and Sentinel 2A MSI TOA reflectance (Uncertainty bars are $k = 2$ ) using Libya 4 CNES ROI coincident scene pairs.	67
Figure 8.	Comparison of Landsat OLI and Sentinel 2A MSI TOA reflectance (Uncertainty bars are $k = 2$ ) using Libya 4 CNES ROI near coincident scene pairs.	67

Figure 9.	Comparison of Landsat OLI and Sentinel 2A MSI TOA reflectance (Uncertainty bars are $k=2$ ) using Cluster 13 coincident scene pairs.	68
Figure 10.	Comparison of Landsat OLI and Sentinel 2A MSI TOA reflectance using Cluster 13 near coincident scene pairs.	68
Figure 11.	Comparison of Landsat OLI and Sentinel 2A MSI TOA cross-calibration gain ratios using Libya 4 CNES ROI coincident scene pairs.	69
Figure 12.	Comparison of Landsat OLI and Sentinel 2A MSI TOA cross-calibration gain ratios using Cluster 13 near coincident scene pairs.	70
Figure 13.	Cross-calibration gain comparison of Landsat 8 OLI and Sentinel 2A MSI using a traditional ROI-based approach and a cluster-based approach from Libya 4 CNES ROI coincident scene pairs (Uncertainty bars, $k=2$ ).	71
Figure 14.	Cross-calibration gain comparison of Landsat 8 OLI and Sentinel 2A MSI using a traditional ROI-based approach and a cluster-based approach using Cluster 13 near coincident scene pairs (Uncertainty bars, $k=2$ ).	71
Figure 15.	Comparison of cluster-based cross-calibration gain ratio with ROI-based cross calibration gain (Uncertainty bars, $k=2$ ).	74

## ABSTRACT

CLASSIFICATION OF NORTH AFRICA FOR USE AS AN EXTENDED PSEUDO  
INVARIANT CALIBRATION SITES (EPICS) FOR RADIOMETRIC CALIBRATION  
AND STABILITY MONITORING OF OPTICAL SATELLITE SENSORS

MAHESH SHRESTHA

2019

An increasing number of Earth-observing satellite sensors are being launched to meet the insatiable demand for timely and accurate data to help the understanding of the Earth's complex systems and to monitor significant changes to them. The quality of data recorded by these sensors is a primary concern, as it critically depends on accurate radiometric calibration for each sensor. Pseudo Invariant Calibration Sites (PICS) have been extensively used for radiometric calibration and temporal stability monitoring of optical satellite sensors. Due to limited knowledge about the radiometric stability of North Africa, only a limited number of sites in the region are used for this purpose. This work presents an automated approach to classify North Africa for its potential use as an extended PICS (EPICS) covering vast portions of the continent. An unsupervised classification algorithm identified 19 "clusters" representing distinct land surface types; three clusters were identified with spatial uncertainties within approximately 5% in the shorter wavelength bands and 3% in the longer wavelength bands. A key advantage of the cluster approach is that large numbers of pixels are aggregated into contiguous homogeneous regions sufficiently distributed across the continent to allow multiple imaging opportunities per day, as opposed to imaging a typical PICS once during the sensor's revisit period.

In addition, this work proposes a technique to generate a representative hyperspectral profile for these clusters, as the hyperspectral profile of these identified clusters are mandatory in order to utilize them for performing cross-calibration of optical satellite sensors. The technique was used to generate the profile for the cluster containing the largest number of aggregated pixels. The resulting profile was found to have temporal uncertainties within 5% across all the spectral regions. Overall, this technique shows great potential for generation of representative hyperspectral profiles for any North African cluster, which could allow the use of the entire North Africa Saharan region as an extended PICS (EPICS) dataset for sensor cross-calibration.

Furthermore, this work investigates the performance of extended pseudo-invariant calibration sites (EPICS) in cross-calibration for one of Shrestha's clusters, Cluster 13, by comparing its results to those obtained from a traditional PICS-based cross-calibration. The use of EPICS clusters can significantly increase the number of cross-calibration opportunities within a much shorter time period. The cross-calibration gain ratio estimated using a cluster-based approach had a similar accuracy to the cross-calibration gain derived from region of interest (ROI)-based approaches. The cluster-based cross-calibration gain ratio is consistent within approximately 2% of the ROI-based cross-calibration gain ratio for all bands except for the coastal and shortwave-infrared (SWIR) 2 bands. These results show that image data from any region within Cluster 13 can be used for sensor cross-calibration. Eventually, North Africa can be used a continental scale PICS.

Article

# Classification of North Africa for Use as an Extended Pseudo Invariant Calibration Sites (EPICS) for Radiometric Calibration and Stability Monitoring of Optical Satellite Sensors

Mahesh Shrestha<sup>1</sup>, Larry Leigh<sup>1</sup>, Dennis Helder<sup>1, \*</sup>

<sup>1</sup> Department of Electrical Engineering and Computer Science, South Dakota State University (SDSU), Brookings, SD 57007, USA; E-Mails: mahesh.shrestha@sdstate.edu (M.S.), larry.leigh@sdstate.edu (L.L.), dennis.helder@sdstate.edu (D.H.)

\* Correspondence: dennis.helder@sdstate.edu; Tel.: +01-605-688-4372

Received: date; Accepted: date; Published: date

**Abstract:** Pseudo Invariant Calibration Sites (PICS) have been extensively used for radiometric calibration and temporal stability monitoring of optical satellite sensors. Due to limited knowledge about the radiometric stability of North Africa, only a limited number of sites in the region are used for this purpose. This work presents an automated approach to classify North Africa for its potential use as an extended PICS (EPICS) covering vast portions of the continent. An unsupervised classification algorithm identified 19 “clusters” representing distinct land surface types; three clusters were identified with spatial uncertainties within approximately 5% in the shorter wavelength bands and 3% in the longer wavelength bands. A key advantage of the cluster approach is that large numbers of pixels are aggregated into contiguous homogeneous regions sufficiently distributed across the continent to allow multiple imaging opportunities per day, as opposed to imaging a typical PICS once during the sensor’s revisit period. This potential increase in temporal resolution could result in increased sensitivity for quicker identification of changes in sensor response.

**Keywords:** Pseudo Invariant Calibration Sites (PICS); Google Earth Engine; Land cover classification; Radiometric calibration; Sensor stability monitoring; Satellite sensors

---

## 1. Introduction

For over 45 years, data from Earth observing satellite sensors have been used to increase understanding of long-term global change. Thus, the quality of data produced by previous and currently operational sensors is a primary concern, as it critically depends on accurate radiometric calibration for each sensor. Accurate radiometric calibration also allows meaningful comparisons of data acquired by different sensors to be combined into a continuous record [1]. Radiometric calibration needs to be performed both before launch (to establish an initial operating state) and at regular intervals after launch (to account for degradations in response due to launch stresses, aging and effects relating to conditions in near-Earth orbit). Sensors often include onboard calibrators (e.g. solar diffuser panels, lamps, thermal blackbody radiators) intended to provide data for radiometric calibration and long-term stability monitoring.

Since an onboard calibrator experiences conditions similar to the sensor, its data will likely show similar degradation in radiometric response. Onboard calibrator systems can increase the design, building, and operating costs of a sensor and are thus not included in all satellites,

especially those designed with shortened operating lifetimes. Alternatively, image data from locations on the Earth's surface exhibiting minimal temporal change and other desirable properties have been identified and are increasingly used as a calibration data source; these sites are known as Pseudo-Invariant Calibration Sites (PICS) [2]. Any changes in a sensor's radiometric response can then be attributed to changes in the sensor itself, rather than to changes at the PICS. Teillet et al. [3, 4] provided a comprehensive list of PICS suitable for post launch radiometric calibration, sensor cross calibration, and long-term stability monitoring. Some of these sites have since been endorsed by the Committee on Earth Observing Sensors (CEOS).

Primarily, PICS are used for three purposes: long term trending to assess sensor radiometric stability, cross calibration of sensors, and absolute radiometric calibration. PICS are most widely used to monitor post launch degradation of sensors [5, 6, 7, 8, 9, 10, 11]. Using data from the CEOS-recommended standard PICS, Chander et al. [5] investigated on-orbit stability of the Terra MODIS and ETM+ sensors, and found that both sensors' measured TOA reflectances changed less than 0.4% per year. Several researchers have used PICS for cross calibration of sensors as well [12, 13, 14, 15, 16]. Li et al. [17] used PICS to cross calibrate the recently launched Sentinel-2A MSI to the OLI and estimated agreement between the corresponding bands to approximately 1% or better. Furthermore, absolute calibration predicts the TOA reflectance, or radiance, observed by the sensor at any given geometry [18, 19, 20, 21, 22]. A recent absolute radiometric calibration model developed by Bouvet can accurately simulate the VNIR band TOA reflectance of Libya 4 to within 1% of observed values [23].

### *1.1 Historical Approach for Identifying Candidate PICS*

Previous work in the search for suitable PICS was limited to a few regions within the Sahara Desert, often based on visual inspection of cloud-free image data to identify candidate spatially homogeneous areas. Using Meteosat-4 data, Cosnefroy et al. [24] selected 20 desert sites of size 100 \* 100 km in North Africa and Saudi Arabia with estimated spatial uncertainties of 3% or less and temporal uncertainties between approximately 1% and 2%. They determined, for some of the selected sites and over short time intervals, that the most spatially stable sites also tended to be the most temporally stable sites. Helder et al. [2] developed an automated technique to locate temporally and spatially optimal stable regions. Using Landsat 5 TM image data, they found six individual sites in the Sahara and Middle East exhibiting spatial and temporal uncertainties on the order of 2% in the VNIR region and 2%-3% in the SWIR region.

### *1.2 Limitations of using traditional PICS*

Imaging of individual PICS such as Libya 4 is limited by a sensor's orbital path, field of view (FOV), and occurrence of cloud cover, which results in an observation frequency far lower than that potentially offered by the sensor's revisit cycle and assuming cloud-free conditions. As a result, more time is required to build a time series dataset with sufficient observations to allow reasonable radiometric analyses with adequate sensitivity. An additional limitation of PICS used for cross-calibration is a lack of surface hyperspectral knowledge at most of the sites.

This limitation imposed by traditional PICS can be addressed by extending PICS to a larger region than it used to be. Ruchira [25] performed an initial study on searching worldwide PICS and she showed that majority region of North Africa are stable to some degree. These stable surfaces are of different intensity level so it is necessary to identify the stable regions having similar spectral profiles in order to expand them for developing extended PICS. These spectrally similar regions of North Africa can be found by developing classification map of North Africa.

### 1.3 Previous Classification of North Africa

Loveland et al. [26] applied an unsupervised classification algorithm to Advanced Very High-Resolution Radiometer (AVHRR) image data to develop a land cover characteristics database for the conterminous US. Using a supervised algorithm, Hansen et al. [27] developed the first global land cover classification using 1 km spatial resolution AVHRR data; their training dataset was previously generated from higher spatial resolution data. Interestingly, both classification methods identified a generic “barren” class, which was defined as land cover having less than 10% vegetation throughout the year; this class included all soils, rocks, and sands. A similar global land cover product was also generated for Terra MODIS using a supervised classification algorithm, with training datasets derived from higher resolution image data and ground-based surface reflectance measurements when available [28]. It also identified a generic “barren” class across North Africa.

To the present time, the “barren” classification is still used to group all soil, sand, and rock land cover types into a single land cover type, as most applications using land cover data do not require such a fine distinction. However, this “barren” land cover also includes spatially and temporally stable ground cover types that are highly desirable with respect to PICS-based radiometric calibration. Consequently, the “barren” land cover type identified in North Africa should be resolved into subclasses, which would allow evaluation of their radiometric intensity and stability for potential use in calibration across wider portions of a sensor’s dynamic range.

### 1.4 Current Approach for Extending PICS

Spectral properties of North Africa have been only studied superficially due to lack of its significance to the scientific community. As its majority of regions are stable, it should be studied more rigorously in order to utilize these regions for radiometric calibration of optical satellite sensors. So, the primary concern of this work is to characterize the temporal variability throughout all of North Africa from Egypt to the Atlantic Ocean (latitude: 36°N to 15°N and longitude: 18°W to 35°E longitude), rather than characterizing limited regions based on manual procedures for identifying specific “optimal” regions. Along with the temporal variability of North Africa, its spectral properties are also studied in order to develop North Africa as continental-scale EPICS. To perform this analysis, a dataset from a well calibrated sensor is necessary so Landsat 8 OLI images acquired over three years, from launch through March 2017, were used. Then, the temporally stable pixels of every image were classified according to the unique spectral response using a classification algorithm. Pixels with spectrally similar responses were then aggregated into continental scale regions. These regions were then considered suitable for future evaluation of their potential for sensor calibration and stability monitoring which will be described in a future paper.

These EPICS can be used for all the radiometric calibration purposes for which traditional PICS have been used such as long term trending, cross-calibration, and developing an absolute calibration model. The key advantage of the EPICS over traditional PICS is its spatial extent which provides a significantly large number of calibration data points than the traditional PICS. The increased number of calibration data points enables the ability to detect the sensor degradation quickly and with more sensitivity than the traditional PICS. It can also help to build the larger cross calibration data set contributing to achieve a cross calibration quality of similar to that of individual PICS in a significantly shorter time interval. Similarly, EPICS based absolute calibration model can significantly increase the temporal resolution of the calibration opportunities to a daily or nearly daily basis.

This paper is organized as follows. Section 1 provides a brief overview of the topic. Section 2 presents the materials and methods used in the analysis. Sections 3 demonstrate the resulting



cluster classification map of North Africa and its validation. Section 4 discusses different thresholds used in the classification of North Africa, cluster properties and potential directions for future research into this topic. Finally, Section 5 provides a brief summary of this work.

## 2. Materials and Methods

### 2.1. Google Earth Engine (GEE)

Google Earth Engine (GEE) is a cloud based platform which provides access to global geospatial datasets and significant processing power [29]. By using the GEE, a user can process petabytes of image data currently contained in the Landsat and other image archives. Images within GEE are stored as tiles in their original projections, spatial resolutions, and bit depth, and arranged into collections for each sensor; this avoids potential issues with degradation of data quality. The image tiles are also placed into a pyramid whose levels consist of the image data down sampled by a factor of 2. Whenever users request any particular portion of an image, only the tile(s) from the appropriate pyramid level are retrieved, which significantly reduces the required computational time.

### 2.2. SDSU Derived Data Product

Landsat 8 OLI data were chosen for this work, as the analyses of Knight et al. [30] and Markham et al. [31] reported an OLI reflectance calibration accuracy of approximately 3%. The key spectral and spatial characteristics of the OLI are presented in Table 1. Through the use of the GEE system, all pixels of North Africa acquired by the OLI over the 3-year period were screened for clouds/cloud shadows and saturated pixels. These data were spatially resampled from the native resolution of 30 x 30 meters to 300 x 300 meters. A temporal mean, standard deviation, and uncertainty (ratio of temporal standard deviation to temporal mean) was calculated for each pixel location, along with a count of the number of measurements that went into the statistics calculations. These summary statistics data were then “stacked” into data cubes and “tiled” into 1° latitude by 1° longitude images. The image and pixel sizes were chosen as a practical trade-off between the amount of data retrievable from GEE and the current processing and storage capabilities of the South Dakota State University (SDSU) Image Processing Laboratory systems. In addition, resampling the tiles to 300 m spatial resolution did not significantly degrade the information obtainable from them as much of North Africa is relatively spatially uniform.

**Table 1.** Salient characteristics of Landsat-8 Operational Land Imager (OLI).

Wavelength range	Band Number	Center wavelength(nm)	Bandwidth(nm)	Spatial resolution(m)
Coastal	1	443	16	30
Blue	2	492	60	30
Green	3	561	57	30
Red	4	654	37	30
NIR	5	865	28	30
Cirrus	9	1373	20	30
SWIR1	6	1609	85	30
SWIR2	7	2201	187	30
Panchromatic	8	590	172	15

Figure 1 shows the concept behind a processed data cube. It consists of 25 layers. Layers 1-8 are the temporal mean statistics image for each VNIR/SWIR multispectral band, ordered by band number starting with the Coastal/Aerosol band and ending with the Cirrus band. Layers 9-16 and 17-24 are the standard deviation and uncertainty images, respectively, again ordered by band number. The final layer consists of the number of resampled image pixels used to calculate the summary statistics.

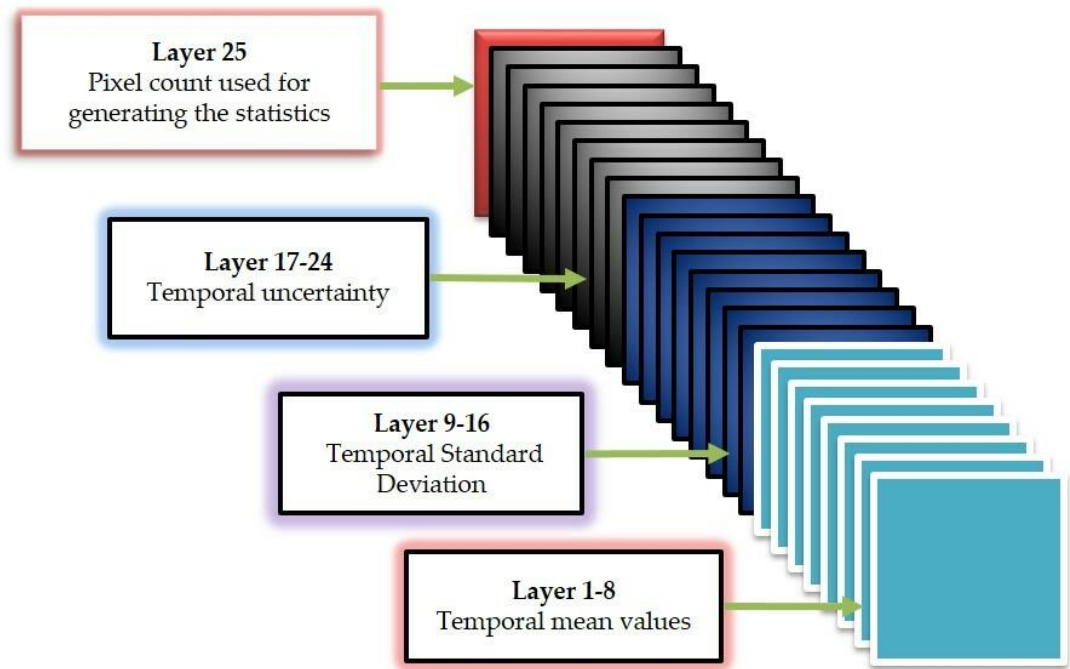


**Figure 1.** SDSU Data Tile Layers Derived from Google Earth Engine (GEE).

### 2.3 Mosaic Image of North Africa

Once the processed data tiles were retrieved from GEE and processed locally into data cubes, the temporal mean images were mosaicked to generate composite images of North Africa. The resulting mosaics covered an area from 36°N to 15°N latitude and 18°W to 35°E longitude. In all, approximately 1003 data cubes were used to generate the North Africa mosaics. As part of the mosaicking process, each pixel in a temporal mean tile was screened for a temporal uncertainty of 5% or less, and sufficient resampled pixel count (25 or greater, as it represented approximately one third of the potential cloud-free acquisitions). Helder et al. [2] used a threshold of 3% temporal stability to identify the individual PICS. Since this work focuses on finding continental scale PICS, the temporal variability criteria was relaxed to 5% in order to account for extra variability likely arising due to the large spatial extent of the PICS.

### 2.4 Classification of North African Land Cover

Landcover maps identifying spectrally similar pixels can be generated through supervised or unsupervised classification algorithms. In supervised classifications (e.g. decision trees, maximum likelihood, and minimum distance [32, 33]), reference “training” datasets are used to perform the classification. In unsupervised classifications (e.g. isodata and k-means [34]), standard image

processing techniques are directly applied to the image data to perform the classification. There is no consensus regarding the superiority of supervised or unsupervised methods used by themselves; the suitability of the classification method depends on the available reference data. Other research [35, 36] suggests that combination of supervised and unsupervised methods can provide more accurate land cover classification results.

This work performs, for the first time, a higher-resolution classification of land cover across all of North Africa. K-means unsupervised classification was chosen as the classification method due to i) its computational simplicity, which is critical when performing analyses at a continental scale [37, 38]; and ii) the lack of prior knowledge of spectral information for that region. The K-means algorithm is presented below:

- Step 1: Estimate initial mean values for  $K = 2$  clusters:

$$\sum_{j=1}^{\text{NoOfClusters}} \sum_{i=1}^{\text{NoOfBands}} \mu_{ij}, \quad (1.1)$$

- Step 2: Calculate the Euclidean distances between each mosaicked image pixel and initial cluster means:

$$\sum_{m=1, n=1}^{\text{Row, Column}} \sum_{j=1}^{\text{NoOfClusters}} D_{jmn} = \sum_{m=1, n=1}^{\text{Row, Column}} \left[ \sum_{j=1}^{\text{NoOfClusters}} \sum_{i=1}^{\text{NoOfBands}} (x_{imn} - \mu_{ij})^2 \right]^{1/2}, \quad (1.2)$$

- Step 3: Classify pixels based on the minimum distance to a cluster:

$$\sum_{j=1}^{\text{NoOfClusters}} \sum_{i=1}^{\text{NoOfBands}} \text{ClassifiedPixels}_{ij} = \min \left( \sum_{m=1, n=1}^{\text{Row, Column}} \sum_{j=1}^{\text{NoOfClusters}} D_{jmn} \right), \quad (1.3)$$

- Step 4: Calculate the new cluster mean:

$$\mu_{ij\text{new}} = \frac{\sum_{j=1}^{\text{NoOfClusters}} \sum_{i=1}^{\text{NoOfBands}} \text{sum}(\text{ClassifiedPixels}_{ij})}{\text{Count}(\text{ClassifiedPixels}_{ij})}, \quad (1.4)$$

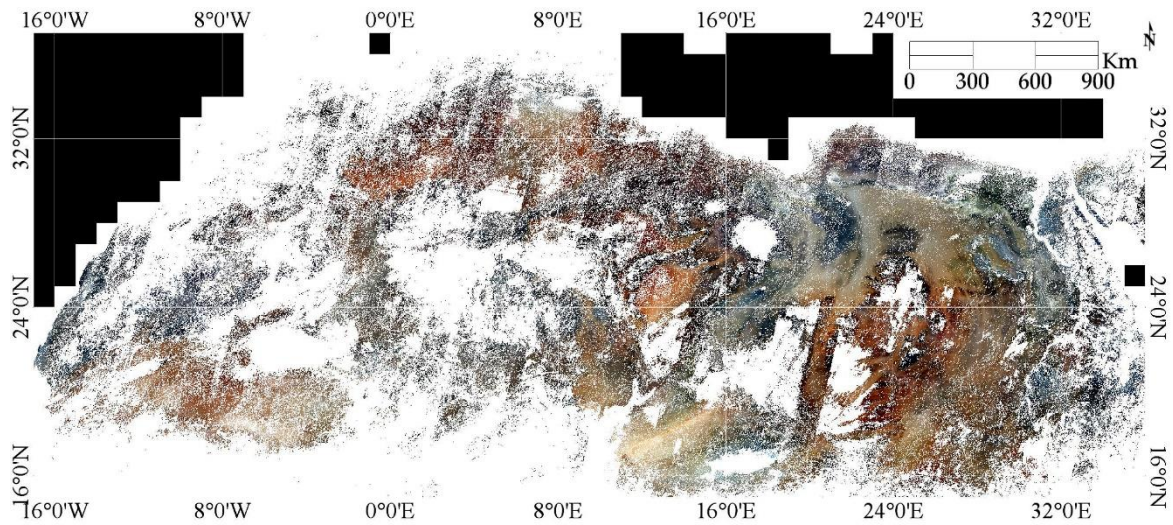
- Step 5: If  $\max(|\mu_{ij} - \mu_{ij\text{new}}|) > 0.0001$  replace the old cluster mean with the new cluster mean calculated in Step 4, then return to Step 2. Otherwise, proceed to Step 6.
- Step 6: Calculate the spatial uncertainty of all pixels within each cluster.
- Step 7: If the maximum spatial uncertainty of any cluster is greater than 5%, increase the number of clusters by one and return to Step 1. Otherwise, terminate the algorithm.

K-means algorithm was initially “seeded” with cluster means represented by the temporal means of two randomly chosen pixels from the mosaicked images. The Euclidean distance between cluster means (two randomly chosen pixels) and each and every pixels of the mosaicked image pixels is calculated in step 2. Third step classifies all the pixels of North Africa based on their minimum distance to the cluster’s mean. The average of the new classified pixels is calculated and considered as the new cluster mean in step 4. The difference between the current cluster mean and the new cluster mean is computed and if the difference is more than the threshold 0.0001 then current cluster mean is replaced by newly computed cluster mean and again start from step 2. A mean difference threshold of 0.0001 was used to determine whether new clusters should be created; this threshold value was chosen to ensure that final convergence of the classification remained independent of the chosen starting pixels. For cluster mean differences of less than the difference threshold, the spatial uncertainties of the current set of clusters was calculated. If any cluster’s spatial uncertainty exceeded 5% in any band, the current cluster count was incremented by 1, and the classification process was repeated; otherwise, the classification process terminated at the current cluster count. A 5% spatial uncertainty threshold was selected in order to balance aggregation within cluster regions (i.e. minimizing the creation of smaller cluster regions that are more widely spread) while ensuring lower spatial uncertainty. For this work, the classification process identified 19 distinct clusters.

### 3. Results and Validation

#### 3.1 Classification of North Africa

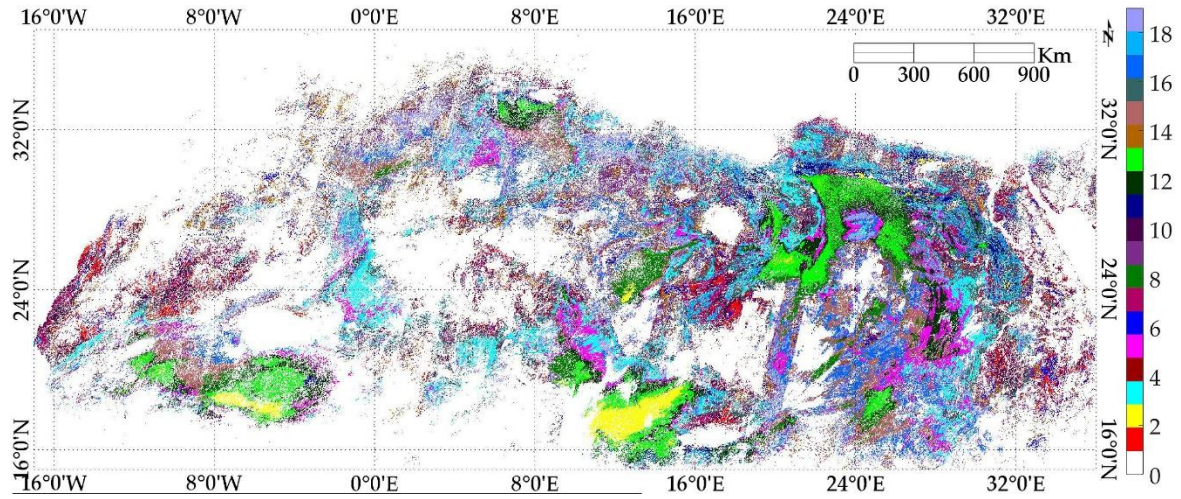
Figure 2 shows the resulting red/green/blue composite mosaicked image of North Africa after filtering for temporally unstable pixels and pixel count threshold. The white areas represent pixels excluded due to temporal instability and pixels identified as having clouds/cloud shadows and/or small water bodies. The black pixels represent “fill” over regions beyond the African continent.



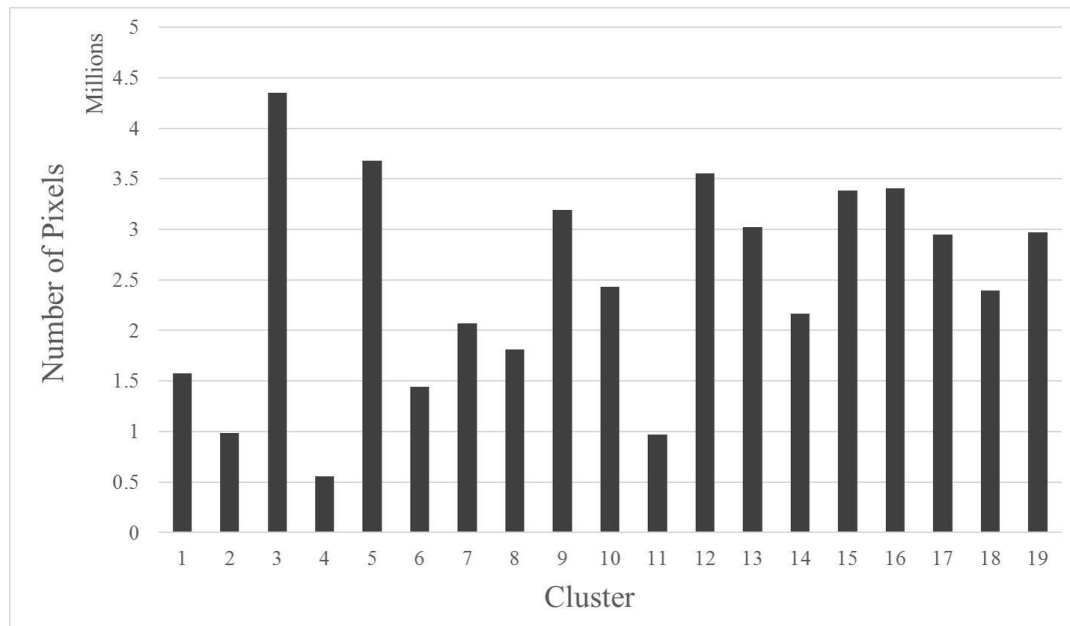
**Figure 2.** North Africa Mosaic After Filtering Temporally Unstable Pixels.

Figure 3 shows the 19 distinct clusters identified in the classification. All of the identified clusters have contiguous regions widely distributed across the continent, potentially allowing a much higher imaging frequency rather than an imaging frequency of several days for most moderate resolution sensors over a single PICS.

Figure 4 shows a bar graph of the resulting pixel counts for each cluster. Among the clusters, Cluster 3 has the largest number of pixels (approximately 4.3 million). Cluster 13 (the light green graph in Figure 3) has approximately 3 million pixels. Although Cluster 3 has the largest pixel count, its pixels are more widely distributed in non-contiguous regions. The Cluster 13 pixels, on the other hand, are grouped into large contiguous regions widely distributed across North Africa, making this cluster a potential candidate for EPICS-based calibration.



**Figure 3.** K-Means Classification of North Africa to 5% Spatial Uncertainty.



**Figure 4.** Number of pixels in each North African cluster.

### 3.2. Spatial Uncertainty of Clusters

Table 2 shows the final spatial uncertainties (ratio of spatial standard deviation to spatial mean) estimated for each cluster when the classification process was terminated. Due to more pronounced atmospheric scatter in shorter wavelengths, the spatial uncertainties are generally higher in the shorter wavelength bands (the exception being Cluster 4, which exhibited greater uncertainty in the SWIR 1 band). Despite its widespread extent, the Cluster 13 spatial uncertainties are within 5% in the Coastal/Aerosol and Blue bands, and within 3% in the longer wavelength bands. As a result, it should be quite useful for radiometric calibration and radiometric stability assessment.

**Table 2.** Cluster Spatial Uncertainties, by Band.



Spatial uncertainty of each cluster of North Africa							
Cluster	Coastal	Blue	Green	Red	NIR	SWIR1	SWIR2
1	5.73	6.31	5.37	3.88	3.87	4.14	4.86
2	7.19	7.27	4.83	3.24	2.60	2.06	3.54
3	4.95	5.31	3.94	2.89	2.78	2.36	3.27
4	8.31	9.66	9.82	8.77	8.10	9.67	9.16
5	4.57	4.75	3.44	2.69	2.47	2.23	2.57
6	7.75	8.94	8.03	5.51	5.27	5.89	5.19
7	5.49	5.85	4.68	3.50	3.35	4.05	5.13
8	5.35	5.89	5.03	2.84	2.93	2.54	2.38
9	5.93	6.71	5.67	3.61	3.73	3.19	4.30
10	5.91	6.46	5.21	3.87	3.38	3.37	4.61
11	5.36	5.77	5.07	4.05	3.33	3.45	6.13
12	4.79	5.05	3.34	2.62	2.23	2.03	2.66
13	4.59	4.80	3.08	2.71	2.11	1.78	2.62
14	5.95	6.88	6.38	4.38	4.49	3.87	4.48
15	5.20	5.91	5.16	2.48	2.46	2.15	1.96
16	4.71	5.03	4.02	3.28	2.99	2.95	3.99
17	5.58	6.25	5.28	3.23	3.15	2.53	2.61
18	4.71	4.94	4.14	3.15	2.70	3.15	4.56
19	5.43	6.15	5.39	3.31	3.79	2.88	3.59

### 3.3. Cluster Spectral Signatures

Figure 5 shows the multispectral signature of each cluster represented by the mean TOA reflectance and  $\pm 1\sigma$  standard deviation.

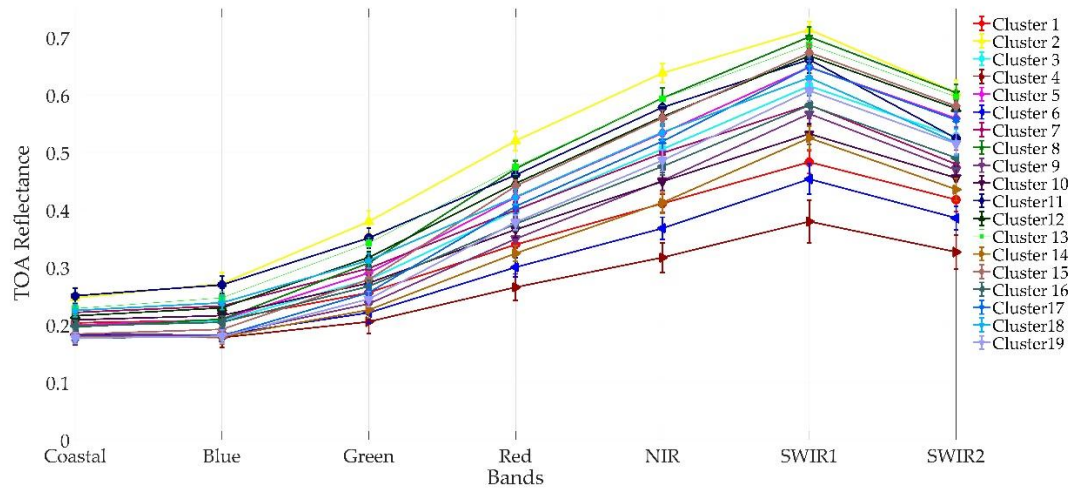


**Figure 5.** Spectral Signature of Clusters, by Band.

At shorter wavelengths, the surface cover is less reflective; the range of TOA reflectance is narrower, and the standard deviations of different clusters exhibit greater overlap. Conversely, the surface cover is more reflective at longer wavelengths; the range of TOA reflectance is wider, and the standard deviations of different clusters exhibit much less overlap, suggesting that the clusters represent distinct surface cover types.

Cluster 4 (represented by the bottom reddish brown plot) has the lowest overall reflectance levels, while cluster 2 (represented by the top yellow plot) has the highest reflectance levels. This distribution allows sensor calibration across wider portions of the dynamic range, especially at longer wavelengths.

### 3.4. Comparison of Traditional PICS and Cluster 13 behaviour

As Cluster 13 spread across the continent, it also includes one of the most widely used traditional PICS i.e. Libya 4, so the temporal behavior of Cluster 13, using selected 16 paths and rows, is compared with Libya 4 temporal behavior as shown in Figure 6. For comparison, Libya 4 CNES (French: *Centre national d'études spatiales*) region of interest (ROI) is chosen as it is regarded as one of the best regions by CNES based on the long term trending of North African and Arabian desert [2, 39]. In Figure 6, the left and right figure present the temporal trend of Libya 4 and Cluster 13, since launch to mid-August 2018, using Landsat 8 OLI. The behavior of Cluster 13 is the same as the behavior of traditional PICS, Libya 4, but it provides a significantly large number of acquisitions than Libya 4 within the same interval of time, i.e. Libya 4 provides 110 cloud-free observations since launch to mid-August 2018 whereas Cluster 13 provides nearly daily observation and offers 1434 cloud-free observations within the same interval of time. The temporal mean ( $\pm 2$  sigma) of Cluster 13 and Libya 4 are also compared in Figure 7. As Libya 4 temporal mean lies within the uncertainty bar of Cluster 13 temporal mean, the temporal mean of both Libya 4 and Cluster 13 are same. This implies that despite its continental scale spatial extent, Cluster 13 has the same response like the Libya 4 CNES ROI.

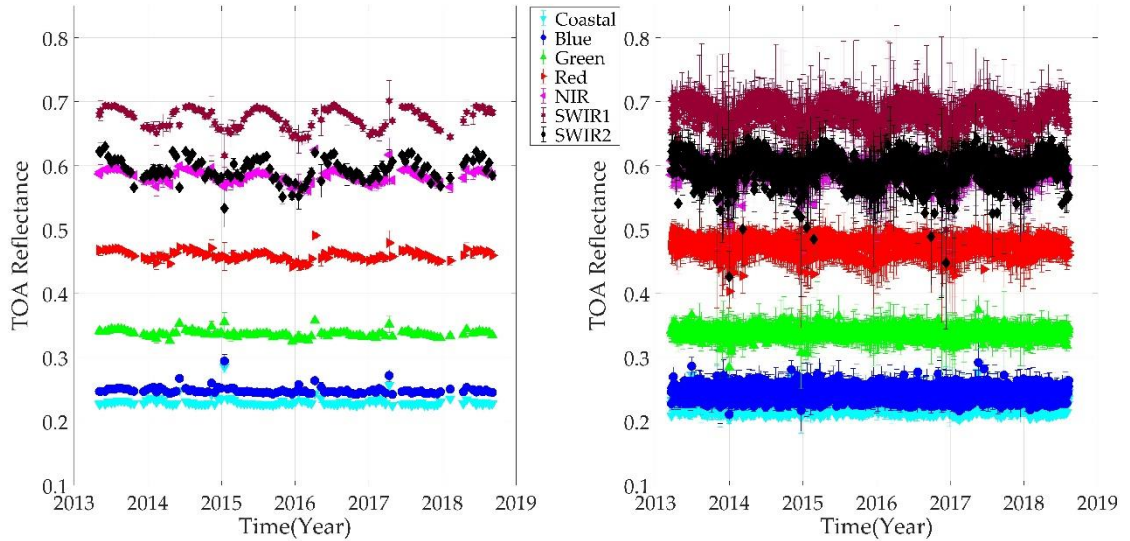


**Figure 6.** Comparison between traditional PICS (Libya 4) and Cluster 13 behavior. The figure on the left and right show the trending of Libya 4 and Cluster 13, since launch to August 2018, using Landsat 8 OLI respectively.

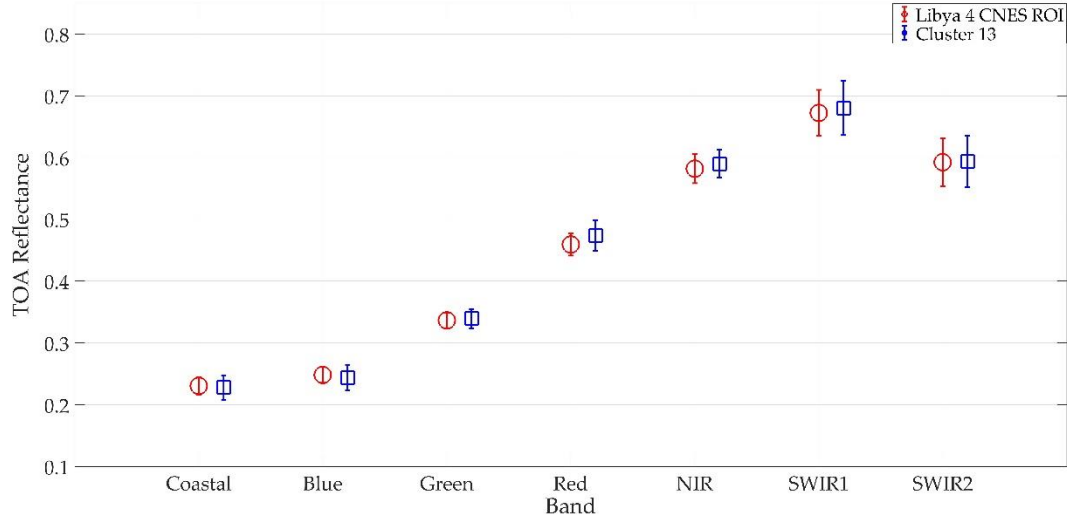


**Figure 7.** Comparison between the temporal mean and its standard deviation between traditional PICS (Libya 4 CNES ROI) and Cluster 13. Red and Blue symbol represent the temporal mean of Libya 4 CNES ROI and Cluster 13 respectively.

### 3.5. Validation of North African Classification

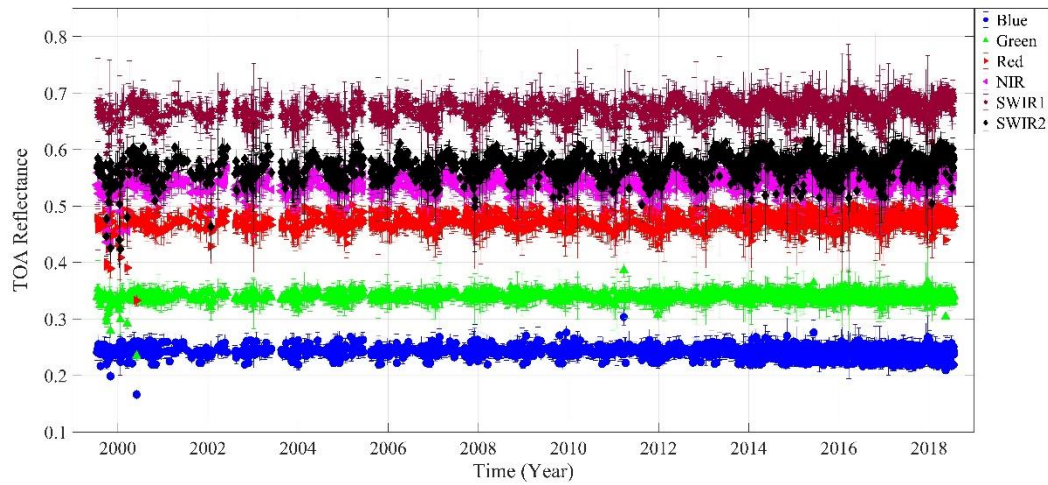
To validate the North Africa classification results, cloud-free, full-resolution Landsat-7 ETM+ scenes imaging Cluster 13 were obtained. To reduce the amount of data to process, images were limited to 9 distinct WRS-2 path/row combinations from different acquisition dates; these path/row combinations maximized the intersection between the ETM+ images and Cluster 13 region boundaries and provided near-daily imaging frequency during the ETM+'s 16-day revisit period. Binary masks were generated for each path/row image and were used to exclude i) pixels identified in other clusters; and Cluster 13 pixels with 5% or greater temporal uncertainty. For the purposes of this work, the masks were created at 30m spatial resolution in order to match the ETM+'s spatial resolution; the mask generation procedure is sufficiently general in nature and can generate masks at any required spatial resolution for any sensor.

Figure 8 shows the resulting temporal TOA reflectance trend of Cluster 13 using selected WRS- 2 paths and rows. All the Landsat 7 images used in this analysis were screened for 5% cloud cover due to which the density of Landsat 7 data sample increases after 2014. The error bar of each data points represents its spatial uncertainty. The cluster means, spatial uncertainty, temporal uncertainty and the corresponding statistics from the temporal trend are listed in Table 3. The overall cluster means and temporal trend from different WRS2 paths and rows are essentially the same for most of the band except NIR band where there is an offset of 0.01 reflectance unit. The lifetime time series of Cluster 13 TOA reflectance using Landsat 7 shows a trend in some bands and also exhibits apparent seasonal effects in the longer wavelength bands, indicating the necessity for additional drift and BRDF correction. It is possible that the observed reflectance differences are due to i) no application of BRDF correction to the data; iii) no application of drift correction to the data and ii) potential outliers in the data. As mentioned earlier, all pixels used as input to the K-means algorithm exhibited temporal uncertainties of 5% or less. Not surprisingly, the Cluster 13 trend data also exhibits approximately 5% or less temporal uncertainty.

In general, the image-estimated spatial uncertainties are larger than the corresponding classification-estimated spatial uncertainties; however, they are within 5% in all bands. The large image-estimated spatial uncertainty is due to the reason that the selected path/row images intersect



sub-regions within Cluster 13 exhibiting more heterogeneous reflectance values, resulting in a larger standard deviation and corresponding spatial uncertainty.



**Figure 8.** Lifetime OLI TOA Reflectance of Cluster 13 using Landsat 7, No BRDF Correction.

**Table 3.** Comparison of K-Means Cluster 13 Statistics and Scene-Based Cluster 13 Statistics.

Cluster 13		K means algorithm		Selected Landsat 7 Scenes		
Band	Mean	Spatial Uncertainty (%)	Temporal Uncertainty (%)	Mean	Spatial Uncertainty (%)	Temporal Uncertainty (%)
Coastal	0.23	4.59	5.00	N/A	N/A	N/A
Blue	0.25	4.80	5.00	0.25	4.82	3.96
Green	0.34	3.08	5.00	0.34	4.30	2.22
Red	0.47	2.71	5.00	0.47	4.13	2.86
NIR	0.59	2.11	5.00	0.60	4.07	2.88
SWIR1	0.69	1.78	5.00	0.69	4.09	2.85
SWIR2	0.60	2.62	5.00	0.60	4.41	3.65

#### 4. Discussion

This work has developed a novel procedure for classification of Landsat-8 OLI image data of North Africa, demonstrating the region's potential for use as an extended PICS. The classification, based on a standard k-means unsupervised classification, is computationally simple and does not require prior knowledge of the region's spectral characteristics. The proposed procedure allows efficient storage and processing of large amounts of OLI image data by resampling them to 300 m spatial resolution; due to the relative uniformity of the region, resampling does not lead to significant loss of spectral information that would adversely impact the resulting classification. The procedure relies on a maximum 5% temporal uncertainty threshold to account for additional variability resulting from use of a much larger region size. Overall, the proposed procedure represents a significant advance over previous efforts that relied heavily upon visual inspection to identify much smaller candidate PICS regions [2, 24], and can be applied "as is" to any sensor. The

proposed procedure identified 19 distinct “clusters” of pixels exhibiting temporal uncertainty of 5% or less. Processing in the procedure terminated when the spatial uncertainty within any given cluster was 5% or less across all bands. The 5% spatial uncertainty threshold represents a practical compromise to avoid the extremes of i) lower spatial uncertainty within a larger number of clusters; or ii) higher spatial uncertainty within a smaller number of clusters, either of which would yield a less accurate calibration.

Previous landcover classifications had identified North Africa as “barren”, containing less than 10% vegetation and composed primarily of some combination of sand, bare soil, and rock [27, 28, 40]. The “barren” classification has largely remained to the present time, as the scientific community did not demand a finer classification. However, this landcover classification applies to many current PICS extensively used for sensor radiometric calibration and performance analysis, such as Libya 4, Mauritania 1, and Algeria 1 [5, 8, 21, 22]. Choi et al. [41] studied the spectral stability of the Libya 4, Libya 1 and Mauritania 2 PICS using average deviation (AD) and spectral angle mapper (SAM) where average deviation is the absolute reflectance difference and SAM is the spectral angle between the test and reference spectrum [42, 43]. This is the earliest attempt to study the spectral similarity of PICS and in this study, they found that ROIs chosen parallel to the along-track direction were spectrally stable for spectral angle mapper values up to  $\pm 2$  degrees, with an average deviation of  $\pm 1.7\%$  in reflectance scale. In contrast to previous work, this work presents the classification of North Africa by studying each and every pixel and group together the pixels with similar characteristics in order to develop extended pseudo invariant calibration sites.

Clusters found by the unsupervised classification algorithm possess different spectral characteristics. Even if the spectral signature of clusters appears to be similar in multiple bands, they are distinct if they are observed across all the bands. The spectral separation between different clusters is wavelength dependent, as shown in Figure 5. Longer wavelengths have very distinct spectral separation; the SWIR1 band has the most distinct spectral separation of 0.33 reflectance units whereas the coastal band has poor spectral separation, just separated by 0.07 reflectance units. So, on the basis of different intensity levels, North Africa offers a better dynamic range for sensor calibration at longer wavelengths than at shorter wavelengths as shown in Figure 5.

Factors to consider when performing a cluster-based analysis include the cluster size (represented by the number of pixels in the cluster) and its distribution across a region, as well as the degree of contiguity of the cluster pixels. The “optimal” cluster for calibration and performance monitoring balances a lower spatial uncertainty, a larger size and distribution (in order to cover a larger geographic area), and a greater degree of pixel contiguity (in order to minimize effects due to geometric misregistration between images); this becomes particularly important for sensors with higher (< 30 m) spatial resolution.

Two of the clusters identified by the proposed procedure (Clusters 2 and 3) exhibit similar levels of spatial uncertainty at longer wavelengths. With respect to cluster size and distribution across the region, Cluster 3 would be considered optimal; however, with respect to cluster contiguity, Cluster 2 would be considered optimal. For sensors with lower geometric accuracy, Cluster 2 would be preferred for radiometric calibration and sensor performance analysis.

Cluster 3 has the largest number of pixels (approximately 4.3 million) as shown in Figure 4, however, as mentioned above, its pixels are relatively non-contiguous. In contrast, Cluster 13 possesses a similar intensity level to Cluster 3, and contains a slightly smaller number of pixels that are almost as widely distributed across northern Africa. However, its spatial uncertainty is smaller than Cluster 3’s across most bands, and its pixels’ form much more contiguous subregions. While other clusters might be preferable to Cluster 13 with respect to spatial uncertainty and cluster characteristics in specific bands (e.g. Clusters 5 and 15 in the Red and SWIR2 bands), Cluster 13

exhibits favorable characteristics across the majority of bands, making it an ideal bright target cluster for calibration purposes.

Similarly, Clusters 4 and 6 provide a lower intensity level that would help widen the dynamic range for PICS based calibration. Between them, Cluster 4 is slightly darker, but it has a spatial uncertainty of approximately 8% to 9% across all bands; in addition, it contains the smaller number of pixels forming less contiguous subregions. Cluster 6 would be preferred due to its larger number of pixels, more contiguous sub-regions and lower spatial uncertainty.

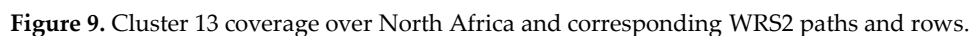
Some of the key advantages that this classification of North Africa offered to the radiometric calibration community are highlighted as follows:

- Historically, PICS-based calibration work used bright desert targets due to there being no universally recognized set of darker PICS exhibiting sufficient temporal and spatial stability. As the proposed procedure identifies clusters with 5% or better temporal stability, it offers the potential for improving calibration accuracy by extending the dynamic range over which calibration can be performed.
- Previously, PICS such as Libya 4 has only one image acquisition corresponding to the satellite revisit cycle but Cluster 13 found by the classification of North Africa is observed in nearly a daily fashion. As Libya 4 lies within Cluster 13, it is similar to observing Libya 4 in a daily manner in contrast to 16 days' period which helps to quickly detect the drift of any satellite sensors.
- One of the major application of PICS is the cross-calibration of optical satellite sensors [14, 16, 44]. Previously, limited cross calibration opportunities were available as PICS are observed once in 16 days. But Cluster 13 provides more cross-calibration opportunities as it spreads across the continent which helps to decrease the cross-calibration gain and bias uncertainties between any optical satellite sensor pairs. In addition, it helps to achieve a cross calibration quality similar to that of individual PICS in a significantly shorter time interval
- Several researchers have developed data driven absolute calibration model in order to simulate the TOA reflectance of an individual PICS, such as Libya 4 [19, 20, 21, 22, 23]. The number of Libya 4 observations is limited due to orbital pattern and cloud cover. As Cluster 13 has a significantly large number of observations than an individual PICS, it enhances the model's ability to predict the TOA reflectance more accurately as more training datasets are available for developing the EPICS based absolute calibration model. Furthermore, EPICS based absolute calibration model can increase the temporal resolution of calibration opportunities to a daily or nearly daily basis for any optical satellite sensor.

This paper only presents initial cluster classification results. Since Cluster 13 has more than 3 million pixels, offers lower spatial uncertainty across most bands, and forms more contiguous subregions widely distributed across North Africa, it stands out as a viable first candidate for EPICS based calibration. Future directions for this work would investigate the use of cluster regions, beginning with Cluster 13, to perform long-term stability assessment and sensor cross calibration. The following sections discuss these potential cluster-based applications in greater detail.

#### *4.1 Long Term Monitoring of Sensor Radiometric Stability*

Cluster-based analyses of long-term sensor stability can potentially benefit from a significant increase in temporal resolution over that provided by individual PICS, since a cluster is considered as a group of spectrally similar pixels, with each cluster containing contiguous regions distributed across the continent. Preliminary investigation into this topic has begun with Cluster 13, as its



A cluster-based cross calibration approach would need to have accurate knowledge of the cluster's expected hyperspectral response, in order to derive appropriate scaling factors to compensate for spectral response differences between a well calibrated "reference" sensor and the sensor to be calibrated. In the absence of ground truth measurements, this knowledge can be derived from available hyperspectral image data. Figure 10 shows a simplified diagram of the five largest contiguous regions of Cluster 13 across North Africa (represented by the blue color) and a map of the available Hyperion coverage over the same regions (represented by the red color). Hyperion is a hyperspectral pushbroom sensor imaging the Earth's surface in the 400 nm – 2500 nm portion of the solar spectrum, in 242 overlapping bands with a spectral resolution of approximately 10 nm; 196 of these bands are well calibrated. It images a 7 km by 100 km swath at a spatial resolution of 30 m [45, 46, 47, 48]. Preliminary investigation has identified a set of 731 Hyperion scenes imaging these regions. After filtering the set for 10% or less cloud cover and sensor view angles within  $\pm 5^\circ$  of nadir, 101 scenes were identified that could be used to determine the hyperspectral profile. As Cluster 13 regions are spectrally similar (as determined by the classification process), it could be expected that the hyperspectral profile of a region may be used as a "representative" profile for the entire cluster.

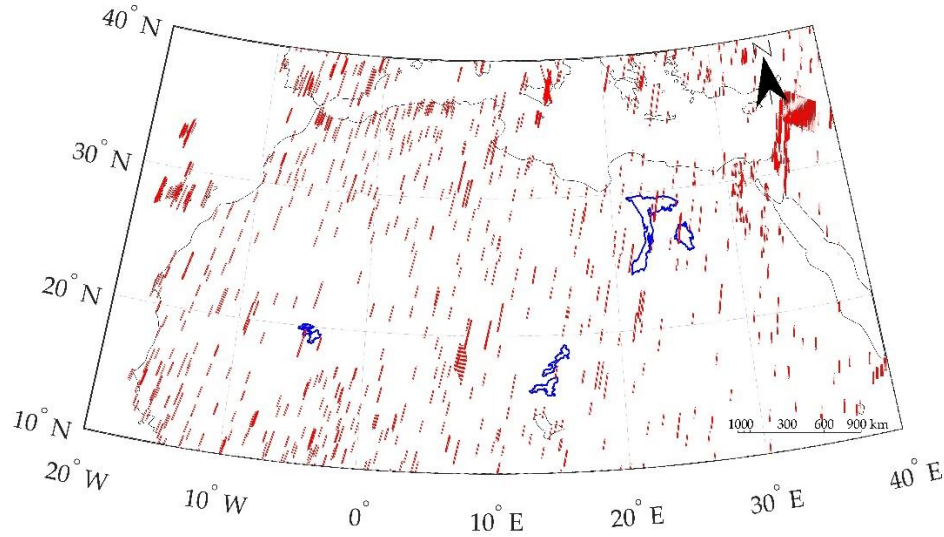


**Figure 10.** Cluster 13 Extent Across North Africa with Corresponding Hyperion Coverage.

## 5. Conclusions

This work demonstrated the potential of using the whole of North Africa as a continental PICS. Traditionally, only a few locations in North Africa have been used due to the lack of knowledge about the temporal stability of most of North Africa. This work analyzed each and every pixel of North Africa and found that the majority of North Africa is temporally stable and could potentially be used for radiometric calibration of satellite sensors.

Conventionally, all these pixels were broadly categorized as a “barren” surface type which includes soil, sand, and rock. This work developed a first-ever high-resolution classification of this “barren” surface type of North Africa using Landsat 8 OLI image data and sub classified it into finer classes using an unsupervised classification algorithm. The algorithm identified 19 clusters each representing a distinct surface type having different spectral characteristics. The range of TOA reflectance at shorter wavelengths is narrow, but wider at longer wavelengths which offers a wide dynamic range to calibrate optical satellite sensors.

All of the identified clusters contained a large number of pixels grouped in contiguous regions potentially useable for sensor calibration and stability assessment. Among all the clusters, Cluster 13 possessed the largest contiguous region, lowest overall spatial uncertainty and was also more widely distributed across North Africa. Due to their spatial extent, most of the clusters allowed multiple imaging opportunities per day in contrast to a typical once during the sensor’s revisit time. Multiple imaging opportunities obtained through a cluster, or EPICS, approach increases the temporal resolution of a calibration time series which leads to increased sensitivity for quicker identification of changes in sensor response.

While some obvious next steps need to take place, as indicated in the discussion sections, the results presented in this paper are very promising. They represent an advance towards the development of an extended PICS (EPICS) with large areal extent, and the ability to evaluate any sensor system on a daily basis using a potentially continent-wide site that behaves as a point site. The cluster-based approach could lead to a new way to calibrate and monitor sensor radiometric performance on orbit. More importantly, this approach could address a very new and serious problem of calibration monitoring for shorter-lived sensor missions, such as low-cost small

satellite-based systems, where more pronounced degradation in radiometric performance is possible.

**Author Contributions:** M.S conceived the research, developed the algorithm with the help of L.L and D.H. M.S, L.L, T.L and D.H analyzed the data. M.S wrote the paper; and L.L and D.H edited the paper.

**Funding:** This research was funded by NASA (grant number NNX15AP36A) and USGS EROS (grant number G14AC00370).

**Acknowledgments:** The authors would like to thank Dr. Thomas Loveland for his guidance and supervision, Google Earth Engine team for providing cloud computing resources, Tim Ruggles for editing the manuscript and Md. Nahid Hasan for providing figure 1, 3, 7 and validation dataset.

**Conflicts of Interest:** The authors declare no conflict of interest.

## References

1. Six, D.; Fily, M.; Alvain, S.; Henry, P.; Benoist, J.-P. Surface characterisation of the Dome Concordia area (Antarctica) as a potential satellite calibration site, using Spot 4/Vegetation instrument. *Remote Sensing of Environment* **2004**, *89*, 83-94.
2. Helder, D.L.; Basnet, B.; Morstad, D.L. Optimized identification of worldwide radiometric pseudo-invariant calibration sites. *Canadian Journal of Remote Sensing* **2010**, *36*, 527-539.
3. Teillet, P.; Chander, G. Terrestrial reference standard sites for postlaunch sensor calibration. *Canadian Journal of Remote Sensing* **2010**, *36*, 437-450.
4. Teillet, P.; Barsi, J.; Chander, G.; Thome, K. In *Prime candidate earth targets for the post-launch radiometric calibration of space-based optical imaging instruments*, Earth Observing Systems XII, 2007; International Society for Optics and Photonics: 2007; p. 66770S.
5. Chander, G.; Xiong, X.J.; Choi, T.J.; Angal, A. Monitoring on-orbit calibration stability of the Terra MODIS and Landsat 7 ETM+ sensors using pseudo-invariant test sites. *Remote Sensing of Environment* **2010**, *114*, 925-939.
6. Kim, W.; He, T.; Wang, D.; Cao, C.; Liang, S. Assessment of long-term sensor radiometric degradation using time series analysis. *IEEE Transactions on Geoscience and Remote Sensing* **2014**, *52*, 2960-2976.
7. Angal, A.; Chander, G.; Xiong, X.; Choi, T.J.; Wu, A. Characterization of the Sonoran desert as a radiometric calibration target for Earth observing sensors. *Journal of Applied Remote Sensing* **2011**, *5*, 059502.
8. Angal, A.; Xiong, X.; Choi, T.; Chander, G.; Wu, A.J.J.o.A.R.S. Using the Sonoran and Libyan Desert test sites to monitor the temporal stability of reflective solar bands for Landsat 7 enhanced thematic mapper plus and Terra moderate resolution imaging spectroradiometer sensors. *Journal of Applied Remote Sensing* **2010**, *4*, 043525.
9. Smith, D.L.; Mutlow, C.T.; Rao, C.N.J.A.o. Calibration monitoring of the visible and near-infrared channels of the Along-Track Scanning Radiometer-2 by use of stable terrestrial sites. *Applied optics* **2002**, *41*, 515-523.
10. Li, C.; Xue, Y.; Liu, Q.; Guang, J.; He, X.; Zhang, J.; Wang, T.; Liu, X. Post calibration of channels 1 and 2 of long-term AVHRR data record based on SeaWiFS data and pseudo-invariant targets. *Remote sensing of environment* **2014**, *150*, 104-119.
11. Doelling, D.R.; Wu, A.; Xiong, X.; Scarino, B.R.; Bhatt, R.; Haney, C.O.; Morstad, D.; Gopalan, A. The radiometric stability and scaling of collection 6 Terra-and Aqua-MODIS VIS, NIR, and SWIR spectral bands. *IEEE Transactions on Geoscience and Remote Sensing* **2015**, *53*, 4520-4535.
12. Chander, G.; Meyer, D.J.; Helder, D.L. Cross calibration of the Landsat-7 ETM+ and EO-1 ALI sensor. *IEEE Transactions on Geoscience and Remote Sensing* **2004**, *42*, 2821-2831.
13. Chander, G.; Angal, A.; Choi, T.J.; Meyer, D.J.; Xiong, X.J.; Teillet, P.M. In *Cross-calibration of the Terra MODIS, Landsat 7 ETM+ and EO-1 ALI sensors using near-simultaneous surface observation over the Railroad*



- Valley Playa, Nevada, test site, Earth Observing Systems XII, 2007; International Society for Optics and Photonics: 2007; p. 66770Y.
14. Chander, G.; Angal, A.; Choi, T.; Xiong, X. Radiometric cross-calibration of EO-1 ALI with L7 ETM+ and Terra MODIS sensors using near-simultaneous desert observations. *IEEE Journal of Selected Topics in Applied Earth Observations and Remote Sensing* **2013**, *6*, 386-399.
  15. Pinto, C.; Ponzone, F.; Castro, R.; Leigh, L.; Mishra, N.; Aaron, D.; Helder, D. First in-flight radiometric calibration of MUX and WFI on-board CBERS-4. *Remote Sensing* **2016**, *8*, 405.
  16. Mishra, N.; Haque, M.O.; Leigh, L.; Aaron, D.; Helder, D.; Markham, B. Radiometric cross calibration of Landsat 8 operational land imager (OLI) and Landsat 7 enhanced thematic mapper plus (ETM+). *Remote Sensing* **2014**, *6*, 12619-12638.
  17. Li, S.; Ganguly, S.; Dungan, J.L.; Wang, W.; Nemani, R.R. Sentinel-2 MSI radiometric characterization and cross-calibration with Landsat-8 OLI. *Adv. Remote Sens* **2017**, *6*, 147.
  18. Govaerts, Y.M.; Clerici, M. Evaluation of radiative transfer simulations over bright desert calibration sites. *IEEE Transactions on Geoscience and Remote Sensing* **2004**, *42*, 176-187.
  19. Govaerts, Y.; Sterckx, S.; Adriaensen, S. In *Optical sensor calibration using simulated radiances over desert sites*, Geoscience and Remote Sensing Symposium (IGARSS), 2012 IEEE International, 2012; IEEE: 2012; pp. 6932-6935.
  20. Govaerts, Y.; Sterckx, S.; Adriaensen, S. Use of simulated reflectances over bright desert target as an absolute calibration reference. *Remote sensing letters* **2013**, *4*, 523-531.
  21. Mishra, N.; Helder, D.; Angal, A.; Choi, J.; Xiong, X. Absolute calibration of optical satellite sensors using Libya 4 pseudo invariant calibration site. *Remote Sensing* **2014**, *6*, 1327-1346.
  22. Helder, D.; Thome, K.J.; Mishra, N.; Chander, G.; Xiong, X.; Angal, A.; Choi, T. Absolute radiometric calibration of Landsat using a pseudo invariant calibration site. *IEEE Transactions on Geoscience and Remote Sensing* **2013**, *51*, 1360-1369.
  23. Bouvet, M. Radiometric comparison of multispectral imagers over a pseudo-invariant calibration site using a reference radiometric model. *Remote sensing of environment* **2014**, *140*, 141-154.
  24. Cosnefroy, H.; Leroy, M.; Briottet, X. Selection and characterization of Saharan and Arabian desert sites for the calibration of optical satellite sensors. *Remote Sensing of Environment* **1996**, *58*, 101-114.
  25. Tabassum, R. WORLDWIDE OPTIMAL PICS SEARCH. South Dakota State University: Country, 2017.
  26. LOVELAND, T.; MERCHANT, J.; BROWN, J.; OHLEN, D. Development of a land-cover characteristics database for the conterminous U. S. *Photogrammetric engineering and remote sensing* **1991**, *57*, 1453-1463.
  27. Hansen, M.C.; DeFries, R.S.; Townshend, J.R.; Sohlberg, R. Global land cover classification at 1 km spatial resolution using a classification tree approach. *International journal of remote sensing* **2000**, *21*, 1331-1364.
  28. Friedl, M.A.; McIver, D.K.; Hodges, J.C.; Zhang, X.; Muchoney, D.; Strahler, A.H.; Woodcock, C.E.; Gopal, S.; Schneider, A.; Cooper, A. Global land cover mapping from MODIS: algorithms and early results. *Remote Sensing of Environment* **2002**, *83*, 287-302.
  29. Gorelick, N.; Hancher, M.; Dixon, M.; Ilyushchenko, S.; Thau, D.; Moore, R. Google Earth Engine: Planetary-scale geospatial analysis for everyone. *Remote Sensing of Environment* **2017**.
  30. Knight, E.J.; Kvaran, G. Landsat-8 operational land imager design, characterization and performance. *Remote Sensing* **2014**, *6*, 10286-10305.
  31. Markham, B.; Barsi, J.; Kvaran, G.; Ong, L.; Kaita, E.; Biggar, S.; Czapla-Myers, J.; Mishra, N.; Helder, D. Landsat-8 operational land imager radiometric calibration and stability. *Remote Sensing* **2014**, *6*, 12275-12308.
  32. Lu, D.; Weng, Q. A survey of image classification methods and techniques for improving classification performance. *International journal of Remote sensing* **2007**, *28*, 823-870.
  33. Hurd, J.D.; Civco, D.L. In *Creating an image dataset to meet your classification needs: a proof-of-concept study*, ASPRS Annual Conf, 2009; 2009.
  34. Kanniah, K.D.; Wai, N.S.; Shin, A.; Rasib, A.W. Per-pixel and sub-pixel classifications of high-resolution satellite data for mangrove species mapping. *Applied GIS* **2007**, *3*, 1-22.

35. Castellana, L.; D'Addabbo, A.; Pasquariello, G. A composed supervised/unsupervised approach to improve change detection from remote sensing. *Pattern Recognition Letters* **2007**, *28*, 405-413.
36. Rozenstein, O.; Karnieli, A. Comparison of methods for land-use classification incorporating remote sensing and GIS inputs. *Applied Geography* **2011**, *31*, 533-544.
37. Pelleg, D.; Moore, A.W. In *X-means: Extending k-means with efficient estimation of the number of clusters*, Icml, 2000; 2000; pp. 727-734.
38. Kanungo, T.; Mount, D.M.; Netanyahu, N.S.; Piatko, C.D.; Silverman, R.; Wu, A.Y.J.C.G. A local search approximation algorithm for k-means clustering. **2004**, *28*, 89-112.
39. Chander, G.; Mishra, N.; Helder, D.L.; Aaron, D.B.; Angal, A.; Choi, T.; Xiong, X.; Doelling, D.R. Applications of spectral band adjustment factors (SBAF) for cross-calibration. *IEEE Transactions on Geoscience and Remote Sensing* **2013**, *51*, 1267-1281.
40. Loveland, T.R.; Reed, B.C.; Brown, J.F.; Ohlen, D.O.; Zhu, Z.; Yang, L.; Merchant, J.W. Development of a global land cover characteristics database and IGBP DISCover from 1 km AVHRR data. *International Journal of Remote Sensing* **2000**, *21*, 1303-1330.
41. Choi, T.J.; Xiong, X.; Angal, A.; Chander, G.; Qu, J.J. Assessment of the spectral stability of Libya 4, Libya 1, and Mauritania 2 sites using Earth Observing One Hyperion. *Journal of Applied Remote Sensing* **2014**, *8*, 083618.
42. Kruse, F.A.; Lefkoff, A.; Boardman, J.; Heidebrecht, K.; Shapiro, A.; Barloon, P.; Goetz, A.J.R.s.o.e. The spectral image processing system (SIPS)—interactive visualization and analysis of imaging spectrometer data. *Remote sensing of environment* **1993**, *44*, 145-163.
43. Yuhua, R.H.; Goetz, A.F.; Boardman, J.W. Discrimination among semi-arid landscape endmembers using the spectral angle mapper (SAM) algorithm. **1992**.
44. Angal, A.; Xiong, X.; Wu, A.; Chander, G.; Choi, T. Multitemporal cross-calibration of the Terra MODIS and Landsat 7 ETM+ reflective solar bands. *IEEE Transactions on Geoscience and Remote Sensing* **2013**, *51*, 1870-1882.
45. Folkman, M.A.; Pearlman, J.; Liao, L.B.; Jarecke, P.J. In *EO-1/Hyperion hyperspectral imager design, development, characterization, and calibration*, Hyperspectral Remote Sensing of the Land and Atmosphere, 2001; International Society for Optics and Photonics: 2001; pp. 40-52.
46. Pearlman, J.; Segal, C.; Liao, L.B.; Carman, S.L.; Folkman, M.A.; Browne, W.; Ong, L.; Ungar, S.G. In *Development and operations of the EO-1 Hyperion imaging spectrometer*, Earth Observing Systems V, 2000; International Society for Optics and Photonics: 2000; pp. 243-254.
47. Ungar, S.G.; Pearlman, J.S.; Mendenhall, J.A.; Reuter, D. Overview of the earth observing one (EO-1) mission. *IEEE Transactions on Geoscience and Remote Sensing* **2003**, *41*, 1149-1159.
48. Pearlman, J.S.; Barry, P.S.; Segal, C.C.; Shepanski, J.; Beiso, D.; Carman, S.L. Hyperion, a space-based imaging spectrometer. *IEEE Transactions on Geoscience and Remote Sensing* **2003**, *41*, 1160-1173.



© 2019 by the authors. Submitted for possible open access publication under the terms and conditions of the Creative Commons Attribution (CC BY) license (<http://creativecommons.org/licenses/by/4.0/>).



Article

# Derivation of Hyperspectral Profile of North Africa Land Cover Types for Use in Sensor Calibration

Mahesh Shrestha<sup>1</sup>, Md Nahid Hasan<sup>1</sup>, Larry Leigh<sup>1</sup>, Dennis Helder<sup>1, \*</sup>

<sup>1</sup> Department of Electrical Engineering and Computer Science, South Dakota State University (SDSU), Brookings, SD 57007, USA; E-Mails: mahesh.shrestha@sdstate.edu (M.S.), mdnahid.hasan@sdstate.edu (NH), larry.leigh@sdstate.edu (L.L.), dennis.helder@sdstate.edu (D.H.)

\* Correspondence: dennis.helder@sdstate.edu; Tel.: +01-605-688-4372

Received: date; Accepted: date; Published: date

**Abstract:** Reference of Earth-observing satellite sensor data to a common, consistent radiometric scale is an increasingly critical issue as more of these sensors are launched; such consistency can be achieved through radiometric cross-calibration of the sensors. A common cross-calibration approach uses a small set of region of interest (ROIs) in established Pseudo-Invariant Calibration Sites (PICS) mainly located throughout North Africa. The number of available cloud-free coincident scene pairs available for these regions limits the usefulness of this approach; furthermore, the temporal stability of most regions throughout North Africa is not known, and limited hyperspectral information exists for these regions. As a result, it takes more time to construct an appropriate cross-calibration dataset.

In a previous work, Shrestha et al. [1] presented an analysis identifying 19 distinct “clusters” of spectrally similar surface cover that are widely distributed across North Africa, with the potential to provide near-daily cloud-free imaging for most sensors. This paper proposes a technique to generate a representative hyperspectral profile for these clusters. The technique was used to generate the profile for the cluster containing the largest number of aggregated pixels. The resulting profile was found to have temporal uncertainties within 5% across all the spectral regions. Overall, this technique shows great potential for generation of representative hyperspectral profiles for any North African cluster, which could allow the use of the entire North Africa Saharan region as an extended PICS (EPICS) dataset for sensor cross-calibration. This should result in the increased temporal resolution of cross-calibration datasets and should help to achieve a cross-calibration quality similar to that of individual PICS in a significantly shorter time interval. It also facilitates the development of an EPICS based absolute calibration model, which can improve the accuracy and consistency in simulating any sensor’s top of atmosphere (TOA) reflectance.

**Keywords:** Extended Pseudo-Invariant Calibration Site (EPICS); Hyperspectral profile; Sensor calibration; Absolute calibration model

---

## 1. Introduction

Satellite image data have been successfully used to characterize and monitor natural and man-made changes to the Earth’s surface over time. As the use of these sensors increases, a primary concern for researchers is ensuring the data are referenced to a common and consistent radiometric scale [2]. This can be achieved through accurate radiometric calibration of each sensor prior to its launch and at regular intervals after launch throughout its operating lifetime.

Many sensor designs include an onboard calibration data source such as lamps or a solar diffuser panel. For sensors without an onboard source, it may be possible to image the moon and generate a calibration dataset from these images. Alternatively, various calibration target regions on the Earth's surface have "ground truth" radiance and/or reflectance measurements available during periods around a sensor overpass, allowing a more direct vicarious calibration approach. An indirect vicarious calibration approach involves cross-calibration between multiple sensors based on analysis of cloud-free coincident or near-coincident image pairs.

Cross-calibration is a post-launch calibration technique that uses a well-calibrated sensor as a transfer radiometer to achieve the radiometric calibration of an uncalibrated sensor using coincident and near coincident scenes of the Earth's surface acquired by both sensors [2] and along with that it is also used to validate the in-orbit calibrated radiance. Accurate cross-calibration places data from multiple sensors on a common, consistent radiometric scale [2, 3]. It provides an alternative, cost-effective calibration method when i) a sensor does not possess an onboard calibration system; and/or ii) opportunities for vicarious calibration using surface radiance or reflectance measurements are limited or non-existent. Cross-calibration includes direct cross-calibration and indirect cross-calibration. The direct cross-calibration is the direction inter-calibration between two instruments, including the SNO and ray-matching methods. While indirect cross-calibration needs a transfer (e.g. stable target, RTM, or third instrument) to inter-calibrate the two sensors. This paper is focused on the method for the in-direct cross-calibration using the deserts as the transfer.

### *1.1 Limitation of Region of Interest (ROI) Based Cross-Calibration Approach*

Sensor cross-calibration is typically performed at a few Pseudo-Invariant Calibration Sites (PICS), located throughout the Sahara Desert in North Africa, where there is sufficient information available about the regional surface stability and a representative hyperspectral profile has been obtained. Depending on cloud cover at the site during each overpass and the revisit period of the sensor (e.g. 16 days for the Landsat sensors), several years are needed to construct a useful dataset for performing cross-calibration of optical satellite sensors and developing absolute calibration model. An absolute calibration model is a simple data-driven model which can simulate the TOA reflectance of virtually any optical sensor and is used for absolute calibration [4].

### *1.2 Proposed Solution to the ROI Based Cross-Calibration Approach*

A representative hyperspectral profile of the site is crucial for developing spectral band adjustment factors (SBAFs) to account for differences in relative spectral response between sensors. [4]. In a previous work, Shrestha et al. [1] identified an "extended" PICS (EPICS), widely spread across North Africa, that could be imaged on a near daily basis by any sensor as shown in Figure 1. These EPICS or clusters are the contiguous homogeneous regions which are spectrally similarly each other. Despite of its large spatial extent across North Africa, it behaves as a point site. Shrestha's work indicated sufficient temporal and spatial stability to be considered as a candidate cross-calibration data source. However, it did not address determination of a representative hyperspectral profile from which the appropriate sensor SBAFs could be derived, thus limiting its suitability for cross-calibration work.

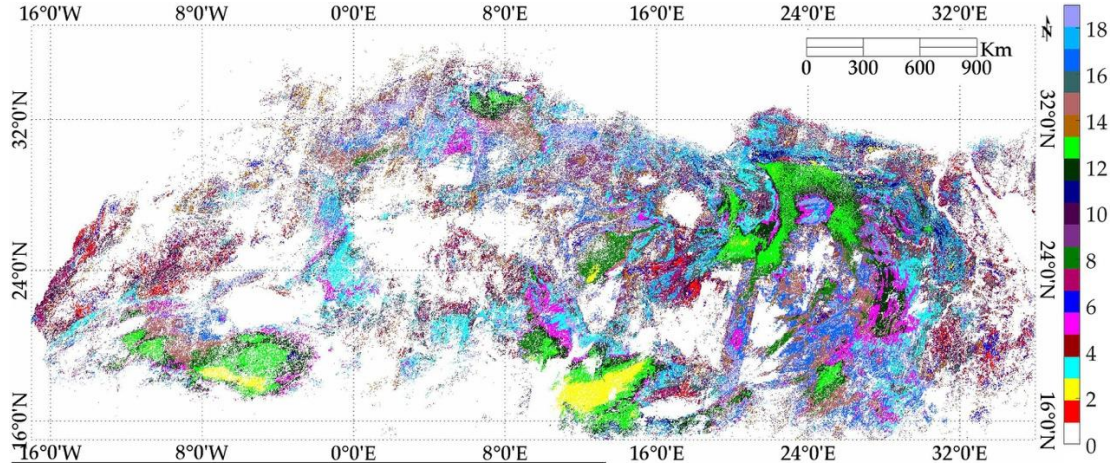


**Figure 1.** K-Means Classification of North Africa to 5% Spatial Uncertainty.

This paper proposes an approach for generating a representative hyperspectral profile applicable to the set of surface characteristic “clusters” previously identified by Shrestha. The Earth Observer 1 (EO-1) Hyperion provides the image data used to generate the profiles; a brief overview of this sensor is provided in the section 1.4. In principle, once a cluster’s representative hyperspectral profile has been generated, any region within the cluster can be used to cross-calibrate a sensor pair. Similarly, with the availability of a representative hyperspectral profile of an EPICS, they can also be used for the development of an absolute calibration model which will be briefly mentioned in section 1.3. In a future paper, a cluster-based cross-calibration method is proposed that will significantly increase the temporal resolution of calibration time series datasets, which will help to achieve similar cross-calibration quality in a much shorter period of time compared to an individual PICS. Similarly, EPICS based absolute calibration model will also be developed which can provide a daily calibration point for any sensor.

### 1.3 EPICS based Absolute Calibration Model

Helder et al. [4] developed a simple empirical absolute calibration model using Libya 4 observations by Terra MODIS and EO-1 Hyperion. In this model, Terra MODIS was used as the calibrated radiometer, whereas EO-1 Hyperion provided the target hyperspectral profile. Hyperspectral profile of the target is scaled to “match” the calibration of the sensor. When this scaled hyperspectral profile is integrated over the sensor relative spectral response (RSR), it will produce the comparable TOA reflectance of the specific sensor. The model was validated using corresponding Landsat 7 Enhanced Thematic Mapper (ETM+) observations and finding agreement of approximately 6% root mean square error (RMSE) between the sensor measured and modeled TOA reflectances, with approximately 2% random uncertainty. This TOA reflectance is compared to the observed TOA reflectance, resulting in sensor calibration. Mishra et al. [5] further improved the model by including BRDF effects due to view zenith angle and also incorporating an atmospheric model. They showed that the PICS-based empirical absolute calibration model has accuracy on the order of 3% with an uncertainty of approximately 2% for the sensors they studied. As this work derives representative hyperspectral profiles for all North Africa clusters, development of absolute calibration models for these EPICS becomes possible. These models help to i) significantly increase the temporal resolution of calibration time series to a daily or nearly a daily basis, and ii) as the model is data-driven in nature, and the cluster approach provides a significantly larger number of observations, the resulting calibration should be more accurate.

### 1.4 Hyperion Sensor Description and Previous Radiometric Calibration Performance

The EO-1 satellite, launched on November 21, 2000, carried Hyperion among its payload of three sensors. Hyperion is a hyperspectral pushbroom sensor imaging the Earth's surface in the 400 nm – 2500 nm portion of the solar spectrum, in 242 overlapping bands with a spectral resolution of approximately 10 nm; 196 of these bands are well calibrated [6, 7]. It images a 7 km by 100 km swath at a spatial resolution of 30 m. Between 2001 and 2007, Hyperion flew one minute behind the Landsat 7 ETM+, in the same orbital path; after 2007, its orbit was lowered by approximately 5 km. Beginning in 2011, its orbit steadily degraded as it used up its maneuvering fuel supply [8], resulting in its ultimate decommissioning from active service in March 2017.

Biggar and other researchers have investigated the stability of Hyperion's prelaunch calibration coefficients by performing vicarious calibrations at the Railroad Valley, Ivanpah Playa, Barreal Blanco and White Sands Missile Range calibration sites [9]. Using the prelaunch coefficients, they observed a radiometric performance (defined as the ratio of the observed Hyperion image radiance and predicted vicarious radiance) of approximately 9% in the VNIR bands and 20% in the SWIR bands, due to calibration gain changes of approximately 8% and 18%, respectively. Using an updated set of calibration coefficients derived from a series of vicarious, solar, and lunar calibrations, the radiometric performance improved to 5% or better [9, 10, 11, 12]. McCorkel et al. reported the results of reflectance-based vicarious calibrations performed at Railroad Valley in 2001-2005 establishing a variability of approximately 2% and accuracy of approximately 3% to 5% in the non-absorption bands [13]. Campbell et al. [14] analyzed over 12 years of time series data from the Frenchman Flat, Ivanpah Playa and Railroad Valley Playa PICS and could not detect statistically significant trends in the data; she concluded that Hyperion exhibited radiometric stability to within approximately 2% to 2.5% in most bands. Czapla-Myers et al. [15] evaluated Hyperion's radiometric calibration using automated Radiometric Calibration Test Site data from Railroad Valley [RadCaTS/Railroad Valley (RRV)] and found that Hyperion agrees with the RadCaTS prediction to within approximately 5% in the VNIR region and approximately 10% in the SWIR region. This suggests that the relative stability between different channels of Hyperion is at least 5% for the VNIR region and 10% for the SWIR region. Recently, Jing *et al.* [16] derived a set of calibration gain and bias coefficients from reflectance-based vicarious calibration at the South Dakota State University vegetative site and available in-situ Radiometric Calibration Network (RadCalNet) data from the Railroad Valley site.

This paper is organized as follows. Section 1 provides a brief overview of the topic. Section 2 discusses the methodology used in the analysis. Sections 3 presents the results of the hyperspectral profile estimation for three of the clusters i.e. Cluster 13, 1, and 4 and its validation, Cluster 13. Section 4 discusses the results and considers potential directions for future research into this topic. Finally, Section 5 presents the conclusion of this work.

## 2. Methodology

### 2.1 Hyperion Acquisitions Over North Africa

Shrestha et al. [1] identified 19 distinct clusters using an unsupervised K-means based classification algorithm over temporally stable pixels of North Africa. All of these clusters are widely spread across North Africa and can be used for EPICS based cross-calibration at varying levels of uncertainty. These clusters cannot be used for cross-calibration of optical satellite sensors until they are sufficiently characterized in the hyperspectral domain. A representative hyperspectral profile is used to compensate the energy difference between two satellite sensors having a different relative spectral response. Figure 1 shows the locations over North Africa

imaged by Hyperion throughout its mission lifetime. Altogether, 3715 images of North Africa are available in the Hyperion archive which will be used to derive a representative hyperspectral profile for each cluster.

To reduce the uncertainties associated with the estimated hyperspectral data due to variability in look angle and cloud cover, Hyperion images with look angles less than  $5^\circ$  and total cloud cover less than 10% were selected for the analysis. The look angle threshold was used to minimize BRDF effects. The cloud cover threshold was used to maximize the likelihood of including only cloud-free pixels. Figure 2 shows the number of filtered hyperspectral images for corresponding clusters. Cluster 5 has the largest number of hyperspectral spectra (294), whereas Cluster 4 has the smallest number (74). Nearly all of the clusters have enough image data to derive a representative hyperspectral profile. Among all the clusters, Cluster 13 stands out as an early viable candidate for EPICS based calibration, as it offers lower spatial uncertainty across all the bands and has more contiguous sub regions widely distributed across North Africa. In this paper, the estimation and validation of a representative hyperspectral profile of Cluster 13 are described in detail and Cluster 1 and 4 are briefly presented; the same methodology was used to estimate representative hyperspectral profiles for the remaining clusters.

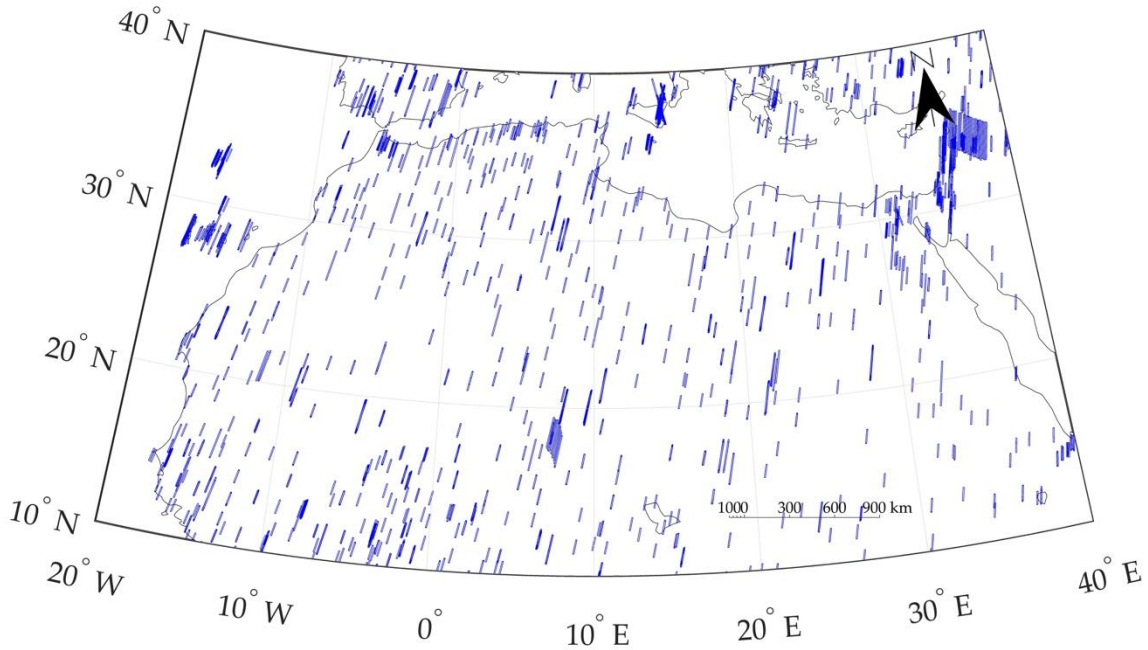


**Figure 2.** Hyperion coverage over North Africa.

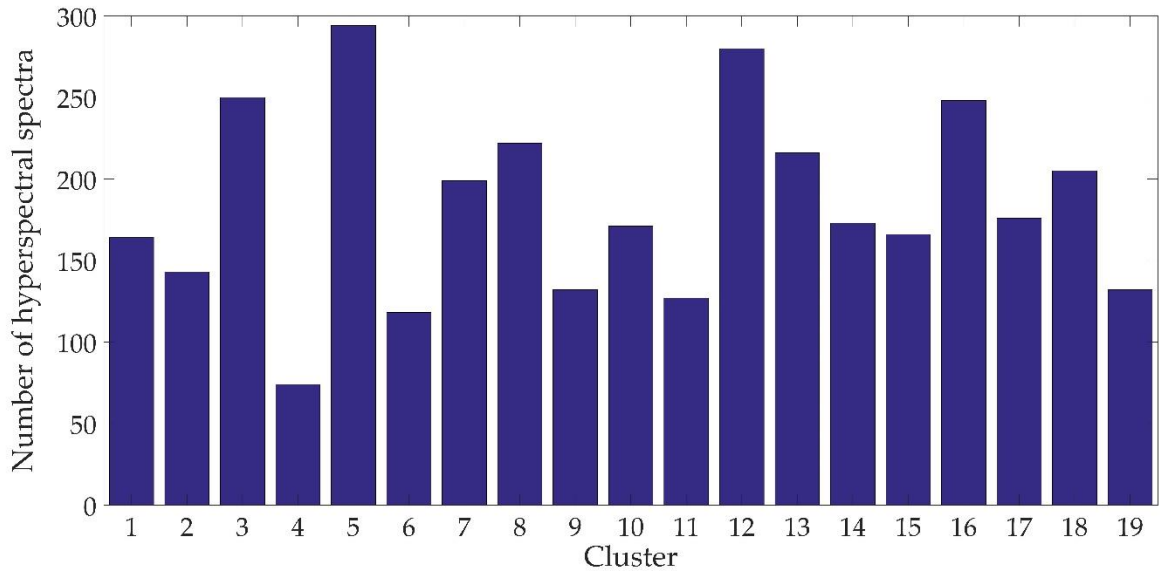


**Figure 3.** Number of hyperspectral spectra over different North African clusters.

## 2.2 Collection of Hyperspectral Data for Cluster 13

Figure 4 shows Cluster 13 spatial extent across North Africa and within this region, Hyperion has imaged 21 different locations. Figure 5 shows the number of hyperspectral spectra corresponding to each WRS-2 path and row. Among all locations, WRS2 path/rows 177/45, 179/41, and 181/40 were extensively imaged by Hyperion, as they correspond to the well-known Sudan 1, Egypt 1 and Libya 4 PICS, respectively, that have been extensively used for radiometric calibration and stability monitoring of optical satellite sensors. The majority of Cluster 13 locations over North Africa have relatively few images, as Hyperion imaged specified locations upon request. 188 hyperspectral spectra from 16 WRS-2 paths and rows, including all these heavily imaged locations over North Africa and other locations, are used to estimate a representative hyperspectral profile of Cluster 13. 28 spectra from six different locations in North Africa, WRS-2 paths/rows 182/42, 198/47, 192/38, 178/43, 185/48, and 200/47, were used to validate the estimated hyperspectral profile of Cluster 13. Validation spectra were chosen from different paths and rows in such a way that they represent the spatial extent of Cluster 13 as shown in solid black rectangle in Figure 4.

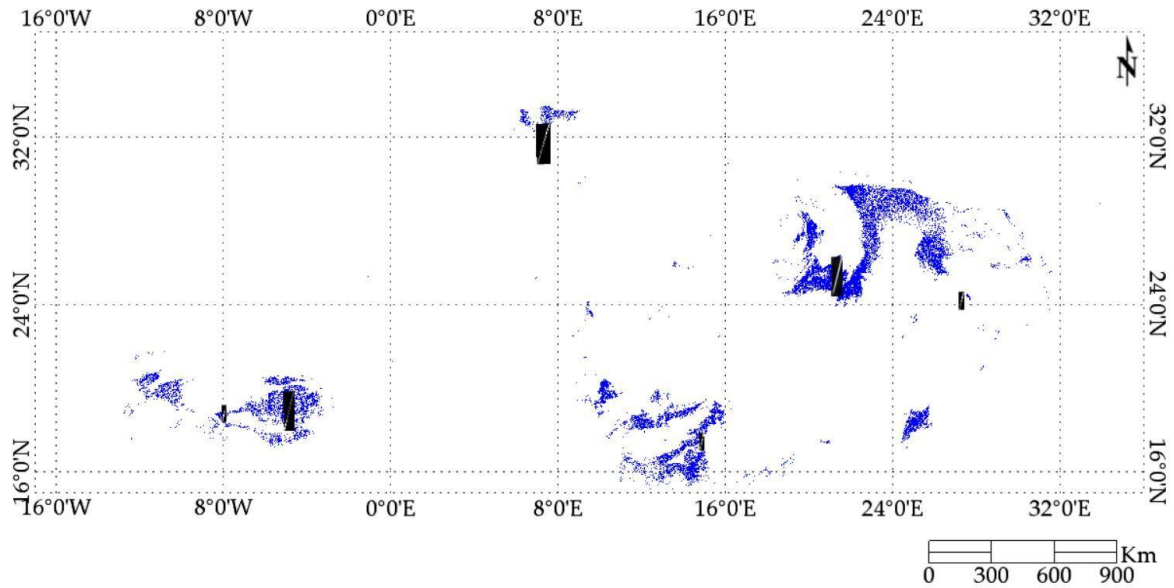


**Figure 4.** Extent of cluster 13 over North Africa. Blue color represents cluster 13 pixels. Black rectangle boxed represent the regions used for validation.

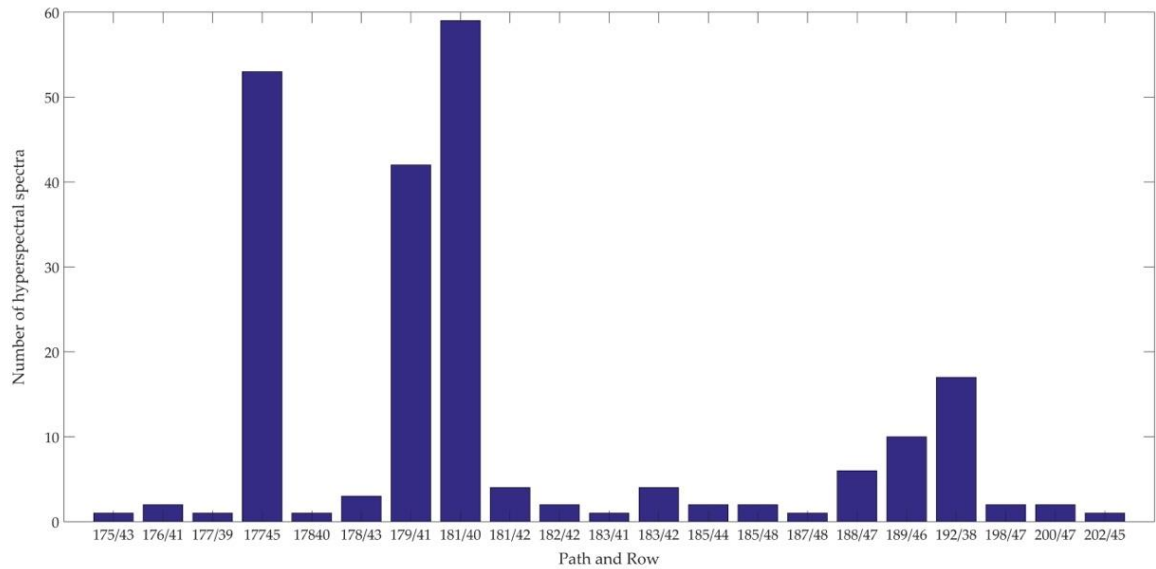


**Figure 5.** Number of hyperspectral spectra corresponding to each WRS-2 Paths and Row of Cluster 13.

### 2.3 Hyperspectral Data for Cluster 13

Two issues were found to have a significant effect on the analysis. The first issue relates to the number of available Hyperion scenes imaging Cluster 13 pixels. 188 Cluster 13 hyperspectral profiles help to derive its reliable representative hyperspectral profile. The second issue relates to the total number of Cluster 13 pixels imaged in a given Hyperion scene; a more representative hyperspectral profile can be generated from a large number of imaged cluster pixels from any WRS-2 path/row. To address the second issue, binary masks identifying cluster 13 pixels within



the Hyperion images were generated. Figure 6 shows the Hyperion binary masks for WRS-2 path/rows 181/40, 179/41, 182/42 and 198/47. WRS-2 path/rows 181/40 and 179/41 are among the 15 locations used to derive the hyperspectral profile of Cluster 13 whereas 182/42 and 198/47 are among six locations used for validation of its derived hyperspectral profile. Fortunately, a significant number of Cluster 13 pixels were found in most Hyperion images. Fewer Cluster 13 pixels were found in the image data from WRS-2 path/row 182/42; however, the pixel counts (approximately 15.85% of the total number of image pixels) allowed generation of reliable hyperspectral profiles from those paths and rows, as shown in Figure 6c.

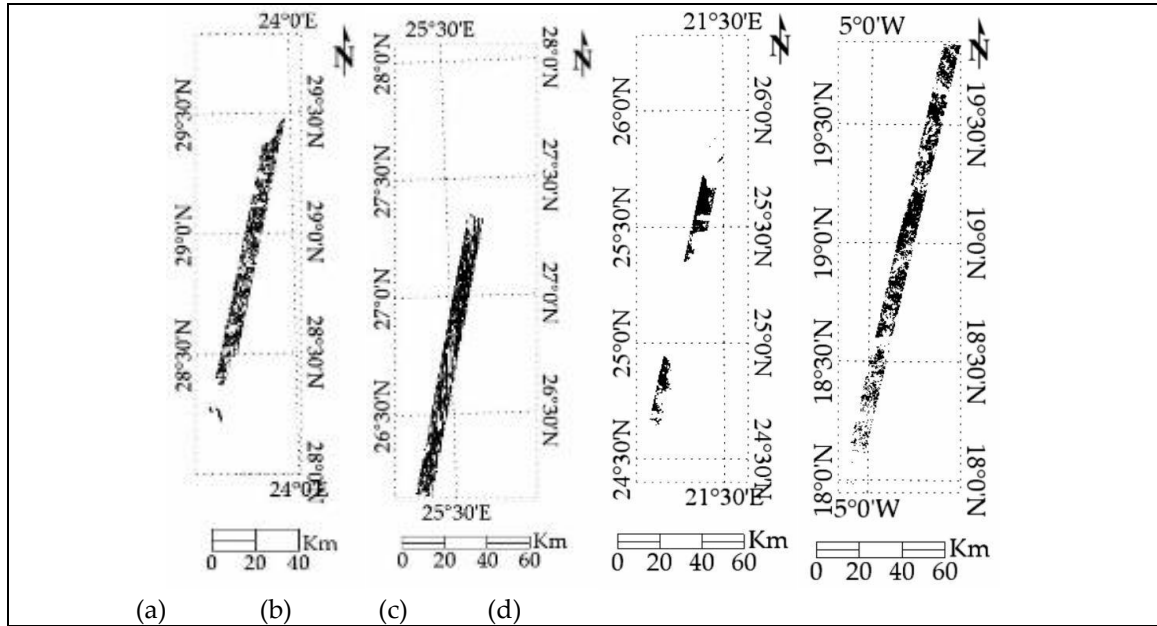


**Figure 6.** Cluster 13 Binary Masks: a) Path/ Row 181/40 (Libya 4), b) Path/ Row 179/41 (Egypt 1) c) Path/ Row 182/42 d) Path/Row 198/47. Black pixels represent Cluster 13 pixels from the Hyperion images.

### 2.3.1. Data Filtering

Of the 731 hyperspectral images from all the locations of Cluster 13, only 216 images met the required look angle and cloud cover constraints. The Hyperion data were also affected by orbital precession. Beginning in 2011, inclination burns to maintain EO-1's initial orbital position were stopped due to lack of onboard fuel [8]. As a result, orbital precession effects led to successively earlier local overpass times and increased solar zenith (decreased solar elevation) angles. The larger solar zenith angles resulted in a decreased signal-to-noise ratio due to a longer atmospheric path between the sensor and ground. These effects ultimately led to both absolute and relative changes in the hyperspectral profiles extracted from the image data. Among these two changes, the relative changes are of greater concern, as the SBAF is more affected by any relative change. To determine the absolute and relative changes on the extracted hyperspectral data of Cluster 13, all corrections such as drift correction, application of calibration gains and biases, and BRDF correction were performed first in order to reduce the uncertainty of estimated representative hyperspectral profile of each cluster.

### 2.3.2. Corrections to Hyperspectral Data



The individual normalized hyperspectral profiles meeting the stability criterion described in the previous section were then corrected to account for potential drift in the sensor response, calibration gain and bias changes, and seasonal variability due to BRDF effects. Each set of corrections is described in further detail below.

### 2.3.2.1. Drift correction and Calibration Gain/Bias Application

Generally, satellite sensors exhibit some degree of change in their radiometric response due to mechanical stresses during launch, operation in a harsh space environment, and aging of the sensor itself. Angal *et al.* [17] and Chander *et al.* [18] assessed Landsat-7 ETM+ and Terra MODIS radiometric stability using PICS image data. Angal's analysis found a statistically significant drift in the ETM+ and MODIS Blue band responses. Chander's analysis confirmed the drifts in the Blue band responses, and also found a statistically significant drift in the ETM+ Red band response.

For this work, it was assumed there is potential drift in the radiometric responses that affect all Hyperion bands. The percentage change in drift was modeled as a linear function of days in a calendar year:

$$\%drift_{\lambda}/year = \frac{slope_{\lambda} * 365 * 100}{intercept_{\lambda}} \quad (1a)$$

where  $\%drift_{\lambda}/year$  (reflectance per year) is the percent degradation per year in a band  $\lambda$ , and  $slope_{\lambda}$  (reflectance per day) and  $intercept_{\lambda}$  (reflectance) are the slope and intercept coefficients obtained from a least-squares linear regression of TOA reflectances in band  $\lambda$ . The correction in potential drift for a given band's hyperspectral profile was then determined as follows:

$$Q_{\lambda, drift\_cor} = Q_{\lambda} - \frac{\frac{\%d_{\lambda}}{yr} \times Yr}{100\%} \quad (1b)$$

Where  $Q_{\lambda}$  is the TOA reflectance of different bands ( $\lambda$ ) of Hyperion, Yr is the decimal year representing the acquisition date and overpass time,  $Q_{\lambda, drift\_cor}$  is the Hyperion TOA profile after yearly drift correction, and  $\frac{\%d_{\lambda}}{yr}$  is the percent yearly drift of band  $\lambda$  estimated from (1a).

For gain and bias correction, the latest set of calibration coefficients reported by Jing *et al.* [16] should be applied after performing the drift correction:

$$Q_{\lambda}^{Corrected} = gain_{\lambda} * Q_{\lambda, drift\_corrected} + bias_{\lambda} \quad (1c)$$

where  $gain_{\lambda}$  and  $bias_{\lambda}$  are the calibration gain and bias coefficients for band  $\lambda$ , and  $Q_{\lambda, drift\_corrected}$  is the drift-corrected TOA reflectance.

### 2.3.2.2. Four Angle Bidirectional Reflectance Distribution Function (BRDF) Correction

The Bidirectional Reflectance Distribution function defines the interaction of light with a given point on the Earth's surface by relating incoming and outgoing radiance at that point. BRDF is an inevitable phenomenon for all optical satellite sensors irrespective of their fields of view [19]. Although nominally operated as a nadir-viewing instrument, Hyperion can be pointed to image from different viewing angles. Consequently, BRDF can affect the resulting estimated TOA reflectance, requiring correction [3, 20] in order to reduce the uncertainty in the final cross-calibration. Most BRDF models used in cross-calibration research are based on empirical or semi-empirical considerations, as these models tend to be simpler to derive and apply than models based on physical considerations. Angal *et al.* [17], Liu *et al.* [21] and Lacherade *et al.* [3] used Roujean's BRDF model [22] to remove the angular effect of solar and viewing geometry while performing the cross-calibration of MODIS and MVIRS. Lacherade *et al.* [3] also used Snyder's BRDF model to

perform cross calibration between different sensor pairs. Wu *et al.* [23] used the Ross-Li BRDF model to remove the angular effect while determining the calibration stability of MODIS using Libya Desert and Antarctic surface.

Helder *et al.* [4] and Mishra *et al.* [5] derived empirical BRDF models based on linear and quadratic functions of solar zenith angle as part of deriving the absolute calibration model for the Libya 4 PICS, as the solar zenith angle is considered to be the major contributor to BRDF effects. However, the level of correction could be increased if the solar azimuth, view zenith, and view azimuth angles are also considered in the BRDF model. For this work, development of a full four angle model begins with the conversion of the view and solar angles from a spherical coordinate basis to a linear Cartesian basis, in order to obtain the TOA reflectance as a continuous function of independent variables [24]:

$$x_1 = \sin(\text{SZA}) * \cos(\text{SAA}) \quad (2a)$$

$$y_1 = \sin(\text{SZA}) * \sin(\text{SAA}) \quad (2b)$$

$$x_2 = \sin(\text{VZA}) * \cos(\text{VAA}) \quad (2c)$$

$$y_2 = \sin(\text{VZA}) * \sin(\text{VAA}) \quad (2d)$$

where SZA and SAA are the solar zenith and azimuth angles in radians, respectively, and VZA and VAA are the sensor viewing zenith and azimuth angles, respectively (also in radians). Multiple linear least-squares regression is used to derive the following linear model:

$$\rho_{\text{model}} = \beta_0 + \beta_1 x_1 + \beta_2 y_1 + \beta_3 x_2 + \beta_4 y_2 \quad (3a)$$

Once the model coefficients have been generated, the mean of the solar and sensor view zenith and azimuth angles is chosen as a reference in order to scale the TOA reflectance to a common level. The resulting reference angles are converted to a Cartesian basis, as in (2a) - (2d), and then used to generate a reference TOA reflectance:

$$Q_{\text{Ref}} = \beta_0 + \beta_1 x_{1\_Ref} + \beta_2 y_{1\_Ref} + \beta_3 x_{2\_Ref} + \beta_4 y_{2\_Ref} \quad (3b)$$

The reference TOA reflectance is then scaled by the ratio of the observed and model predicted TOA reflectances to obtain the final BRDF-corrected TOA reflectance:

$$Q_{\text{site}} = \frac{Q_{\text{obs}}}{Q_{\text{model}}} * Q_{\text{Ref}} \quad (3c)$$

### 2.3.2.3 Estimation of a Representative Cluster 13 Hyperspectral Profile

After significant yearly drift, calibration gain and bias, and BRDF correction, these hyperspectral data are further analyzed to identify relative changes in the Cluster 13 hyperspectral profiles. 188 individual profiles were optimally normalized with respect to the overall Cluster 13 mean hyperspectral profile.

The optimal normalization constant was found by minimizing the sum of squared residual errors between the mean cluster 13 profile and the individual profiles over a reduced set of wavelengths: A reduced wavelength set consists of the 81 wavelengths from transmission windows in the electromagnetic spectrum which have high transmissivity and have been very widely used for remote sensing purposes, are used to derive optimal constants for all hyperspectral profile.

$$\text{Optimal Constant}_i = \frac{\sum \bar{q}_{\text{ref}}(\lambda) q_i(\lambda)}{\sum q_i(\lambda)^2} \quad (4)$$

where  $\bar{q}_{\text{ref}}(\lambda)$  is the mean filtered hyperspectral profile of Cluster 13 and  $q_i(\lambda)$  is a filtered individual hyperspectral profile.

Once the individual profiles were optimally normalized, absolute differences between the normalized profiles and the mean cluster 13 profile were calculated. Any normalized profile that significantly deviated from the mean profile in any wavelength range was excluded from further analysis because such deviation represents the relative change on the hyperspectral profile which adversely effects the SBAF calculation. With this additional screening step, filtered individual profiles were determined to be suitable for use in generating the representative profile for the cluster.

### 3. Results

#### 3.1 Pre-processing of Hyperspectral Profiles of Cluster 13

Cluster 13 regions are spread throughout North Africa; as a result, Hyperion had images of Cluster 13 at 21 different location of North Africa. Among these locations, hyperspectral data from 15 locations were used to estimate the hyperspectral profile. These locations were selected for hyperspectral profile estimation for two reasons that increased the reliability of the estimation: i) the Hyperion images contain a significant number of Cluster 13 pixels, and ii) Hyperion frequently imaged some of these paths and rows. The hyperspectral data from these 15 locations are subjected to drift correction, application of calibration gain and bias and BRDF correction before using them to estimate the Cluster 13 representative hyperspectral profile.

Drift correction using equations (1a) and (1b) was applied to 14 Hyperion channels exhibiting statistically significant drift in their response. The resulting hyperspectral profiles are shown in Figure 7, with the red profile representing the original spectrum and the green profile representing the drift-corrected spectrum. The observed drifts were generally small in magnitude (as low as 0.1 % per year); the drift-corrected spectrum is virtually indistinguishable from the original spectrum. After application of the drift correction, calibration gains and biases were applied to those channels with significant gain and bias. 25 Hyperion channels have a significant gain (different from unity) and 44 channels have a significant bias (different from 0). Higher wavelength channels have significant gain and bias, so the effect of gain and bias is clearly visible as represented by the blue spectrum in Figure 7. After calibration gain and bias application, the four angle BRDF correction was performed to these spectra. BRDF correction had a greater effect at the wavelength extremes. A minimal correction was observed in effect the 500-600 nm region, as this spectral region transitions between predominant atmospheric scattering and more direct transmission to the surface. BRDF correction was more pronounced at longer wavelengths due to the greater correction of seasonality effects, represented by the cyan spectrum in Figure 7.

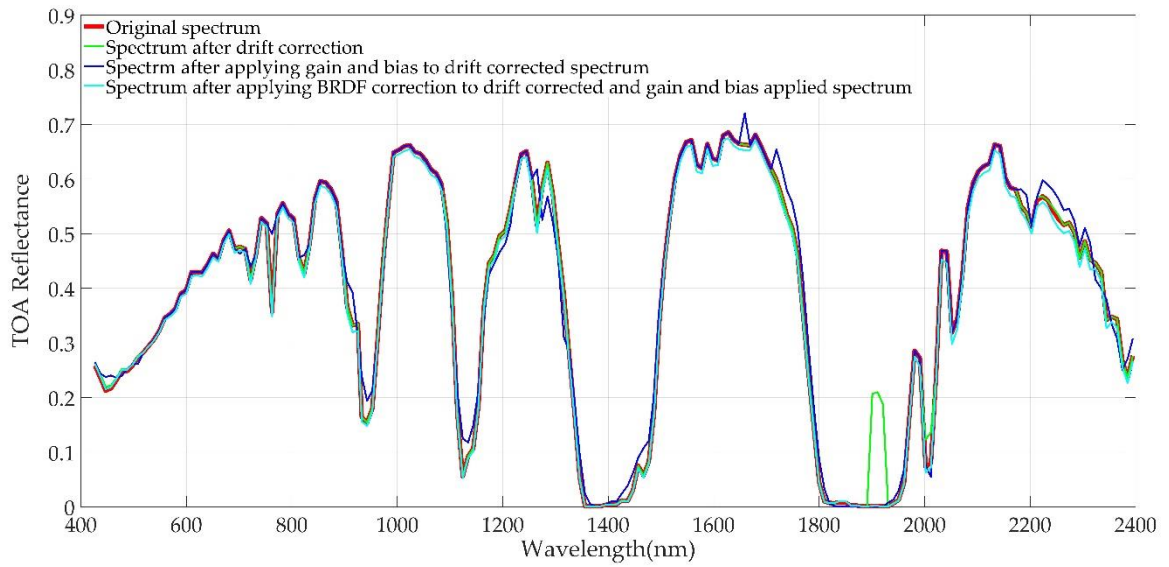


**Figure 7.** Corrections applied to the hyperspectral profile. Red curve represents the original spectrum and blue represents the corrected hyperspectral data.

### 3.2 Collection of Hyperspectral Profiles of Cluster 13

Figure 8 shows the corrected hyperspectral profiles extracted from different locations of Hyperion image data that are used to estimate a representative Cluster 13 hyperspectral profile. The Hyperion image data are divided into three temporal ranges: i) from EO-1's launch to 2007; ii) 2008 through 2015, and iii) 2016 to its decommissioning in March 2017. During the first time period, EO-1 flew in the same orbit as Landsat-7 but 1 minute later (green spectra). During the second time period, EO-1 flew in an orbital path approximately 5km below Landsat-7's path (blue spectra) and began a steady drop in altitude in 2011 that worsened through 2016 to decommissioning (red spectra). The spectrum of the surface is similar from EO-1's launch to 2015, so the green spectra are overlaid by the blue spectra and aren't clearly visible in Figure 8.

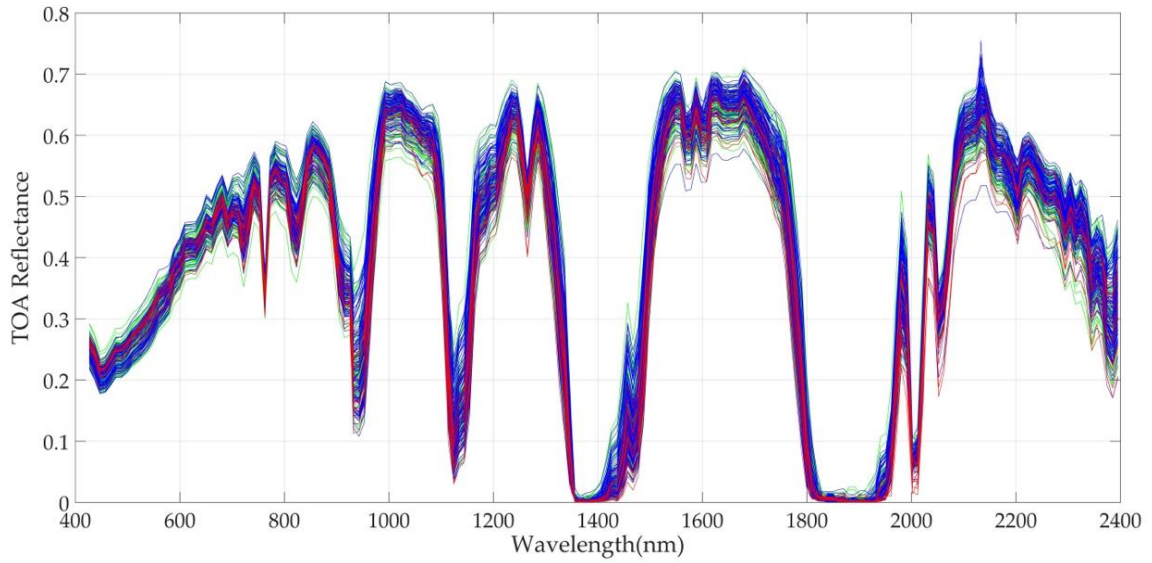


**Figure 8.** Hyperspectral data of cluster 13. Green represents the spectra from EO-1's launch to 2007. Blue represents the spectra from 2008 through 2015 and red represent the spectral from 2016 to its decommissioning in March 2017.

As seen in Figure 8, the post-2016 hyperspectral data are at decreased reflectance levels compared to the pre-2016 data. The decreasing altitude of EO-1's orbit increased its orbital precession, shifting the local acquisition time progressively earlier and resulting in larger solar zenith angles at the acquisition time; since shadow increases with solar zenith angle, the measured surface reflectance decreases. Assuming the shape of the hyperspectral profile did not significantly change from launch to decommissioning, the decrease in hyperspectral intensity over time will not significantly affect SBAF calculation, since the SBAF is defined as a ratio of reflectances derived from the same profile, in effect, the decrease is "cancelled out" in the SBAF calculation. The primary concern, then, relates to whether the hyperspectral profile shape is exhibiting any significant degree of change over time.

### 3.3 Investigation of Relative Change of HyperSpectral Profiles of Cluster 13

Figure 9 shows the absolute difference between the individual normalized hyperspectral data and the mean hyperspectral data of cluster 13. Clearly, the absolute difference between the normalized hyperspectral data before 2016 and the mean Cluster 13 data is generally constant within 0.035 reflectance units across all wavelengths, indicating no significant relative change in any hyperspectral profile. The variation in an absolute difference between the normalized individual hyperspectral profiles and mean Cluster 13 hyperspectral profile is due to the spatial variability within Cluster 13, resulting from the threshold used for the initial classification analysis. The absolute differences between three of the pre-2007 and post-2016 hyperspectral data and the mean Cluster 13 data are not constant as represented by green and red dots below 600 nm; having higher absolute difference than -0.04 and green dots which rises rapidly after 2200 nm as shown in Figure 9. These non-constant differences indicate significant relative changes at both shorter and longer wavelengths. These three relatively unstable hyperspectral profiles of Cluster 13 were excluded from further analysis as such relative instability affects the SBAF calculation. Only 185 hyperspectral profiles meet the filter criteria of look angle, cloud cover, and stability in the relative

signature. These 185 hyperspectral profiles are thus suitable for estimating the hyperspectral profile of Cluster 13.

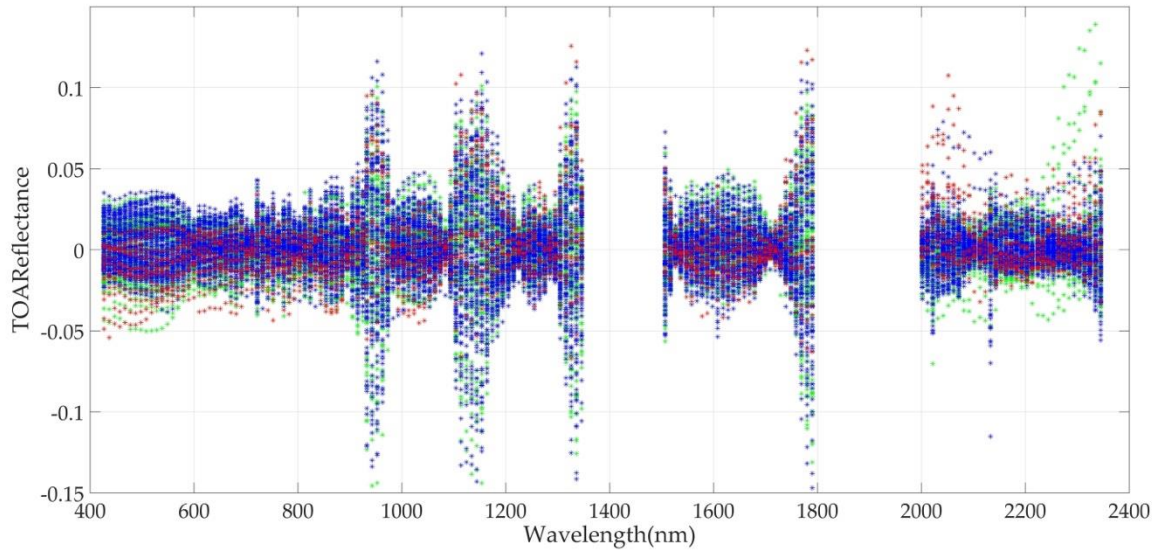


**Figure 9.** Absolute difference between the individual normalized hyperspectral data with the mean Cluster 13 hyperspectral data.

### 3.4 Estimation of a Representative Hyperspectral Profile of Cluster 13

After finding relatively stable hyperspectral measurements of cluster 13, the estimated hyperspectral profile of Cluster 13 is calculated by averaging the 185 hyperspectral data which is shown by the blue curve in Figure 10. The resultant uncertainty is calculated by taking the ratio of the standard deviation to the mean as shown by the red curve in Figure 10. The uncertainty of the VNIR region of Cluster 13 is approximately 5% whereas the SWIR region has less than 4% temporal uncertainty. These observed uncertainties are due to the combination of both temporal and spatial uncertainty of Cluster 13.

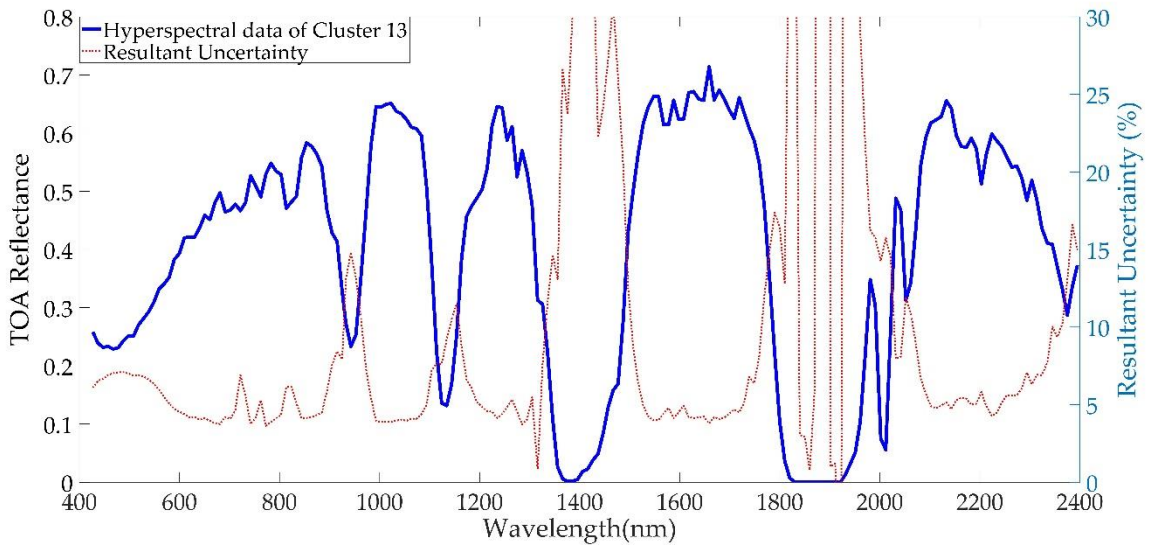


**Figure 10.** Estimated representative hyperspectral profile of Cluster 13 and its resultant uncertainty.

### 3.6 Estimation of a Representative Hyperspectral Profile for Different Reflectance Clusters

A similar methodology was used to estimate a representative hyperspectral profile of clusters exhibiting different reflectance levels. Among the clusters, Cluster 4 is the darkest cluster and is shown in Figure 11. Overall, Cluster 4 has 43 locations providing 65 spectra suitable for estimation of a representative hyperspectral profile, and another 3 locations providing 6 spectra suitable for validation. The temporal uncertainty over much of the spectral range is approximately 10%, with an additional 1-2% uncertainty at the wavelength extremes.

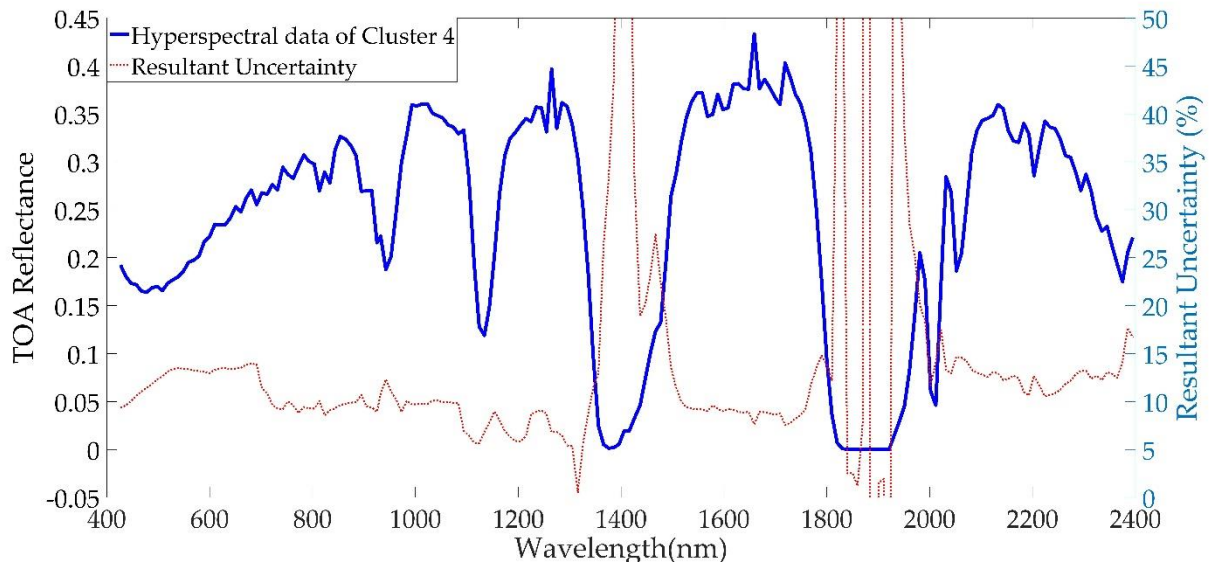


**Figure 11.** Estimated representative hyperspectral profile of Cluster 4 and its resultant uncertainty.



The intensity level of Cluster 1 is between those of Cluster 13 and Cluster 4. Cluster 1 has 161 spectra from 56 locations of North Africa which are suitable for estimation and validation of its representative hyperspectral profile. 150 hyperspectral profiles from 53 locations were used to estimate a representative hyperspectral profile of Cluster 1 as shown in Figure 12, and 3 locations provide 6 spectra suitable for validation. The temporal uncertainty for the hyperspectral profile of Cluster 1 is approximately 6 percent for most of the spectral region whereas it exhibits approximately 1% less uncertainty in the shorter wavelengths and 2-3% additional uncertainty at longer wavelengths.

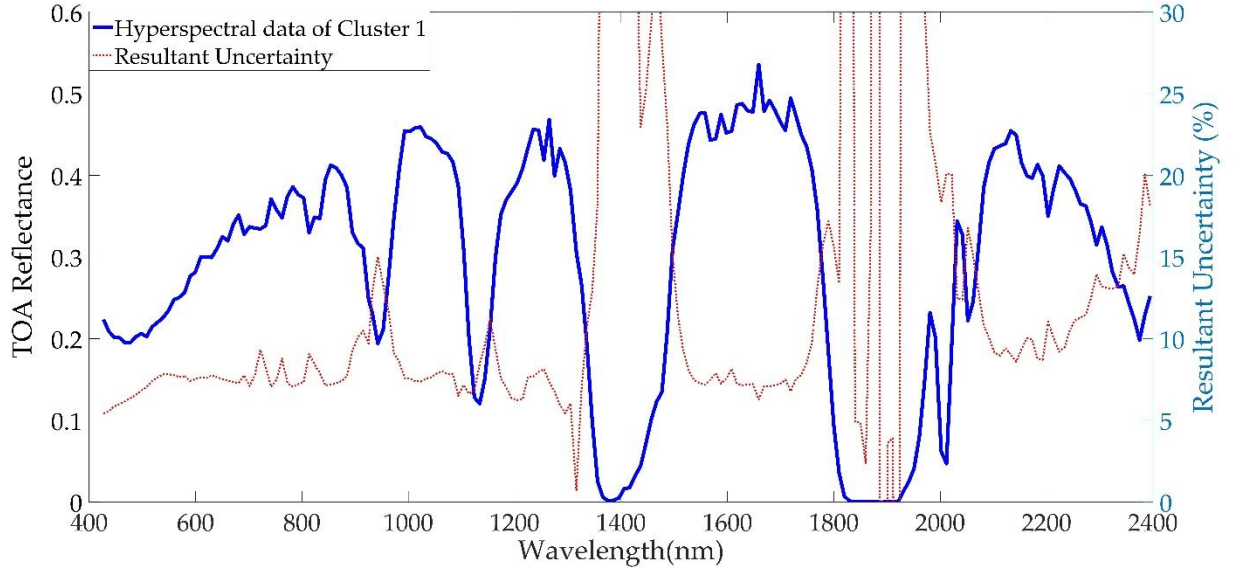


**Figure 12.** Estimated representative hyperspectral profile of Cluster 1 and its resultant uncertainty.

Hyperspectral data for the rest of the clusters are estimated with the same procedure and are included in Appendix A.

### 3.7 Validation of the Estimated Hyperspectral Profile for Cluster 13

#### 3.7.1 Hyperspectral Domain

For validating the hyperspectral spectrum of Cluster 13, spectra from Path/Row 182/42 (mean of 2 spectra), 198/47 (mean of 2 spectra), 192/38 (mean of 17 spectra), 178/43 (mean of 2 spectra), 185/48 (mean of 2 spectra) and 200/47 (mean of 2 spectra) were used. Figure 13 shows the normalized TOA reflectance of the estimated hyperspectral signature of Cluster 13 with its 2-sigma standard deviation and the normalized spectrum from the validation path/rows. The estimated hyperspectral profile of Cluster 13 is used as a reference spectrum for normalizing the hyperspectral profile. As the Cluster 13 hyperspectral profile was used as a reference spectrum for normalization, deviations from unity illustrate the difference between the Cluster 13 spectra and the validation spectra broken down by path/row. These spectra fall inside the uncertainty range of the Cluster 13 spectrum, ensuring that the hyperspectral signatures from those selected paths are the same as the estimated hyperspectral data of Cluster 13. This suggests that the estimated Cluster 13 spectrum can be used to represent the spectrum for any sub region.



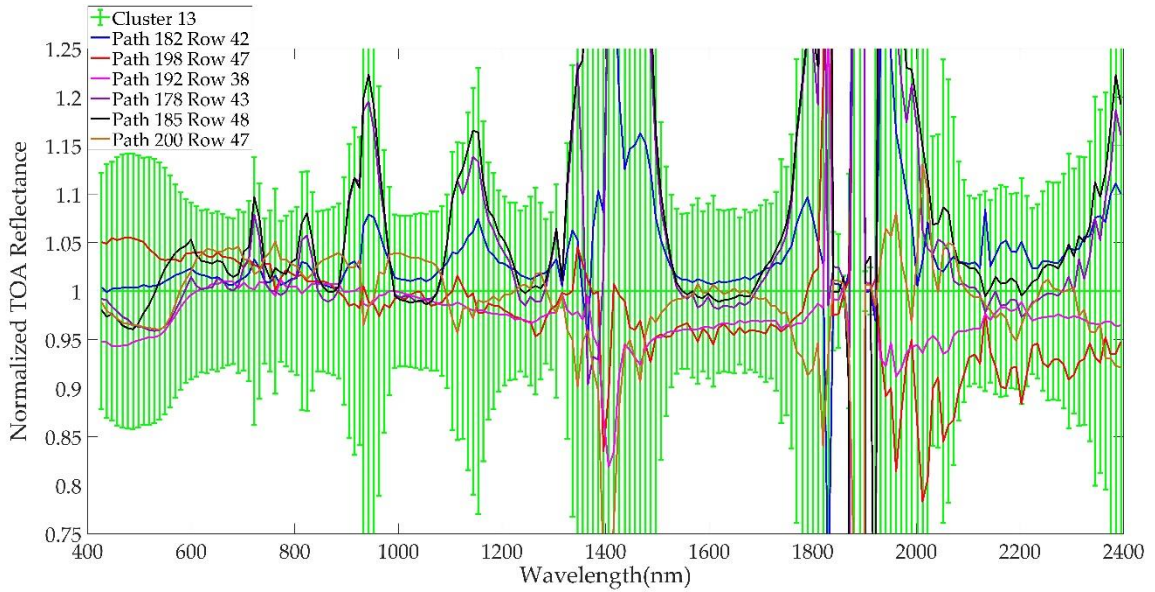


**Figure 13.** Validation of hyperspectral spectrum of Cluster 13.

To validate the representative hyperspectral profile of Cluster 4, two spectra each were derived from images of WRS-2 Path/Row 176/40, 202/42 and 198/38. The mean from these three paths/rows were used and all the spectra were normalized to the representative hyperspectral profile of Cluster 4. Figure 14 shows the normalized Cluster 4 profile with a 2-sigma standard deviation (green color), and the normalized spectra from the validation path/rows represented by the blue, red, and black profiles. These spectra lie within the Cluster 4 uncertainty range, suggesting that the estimated hyperspectral profile can be used to represent the spectrum for any of its sub-regions.

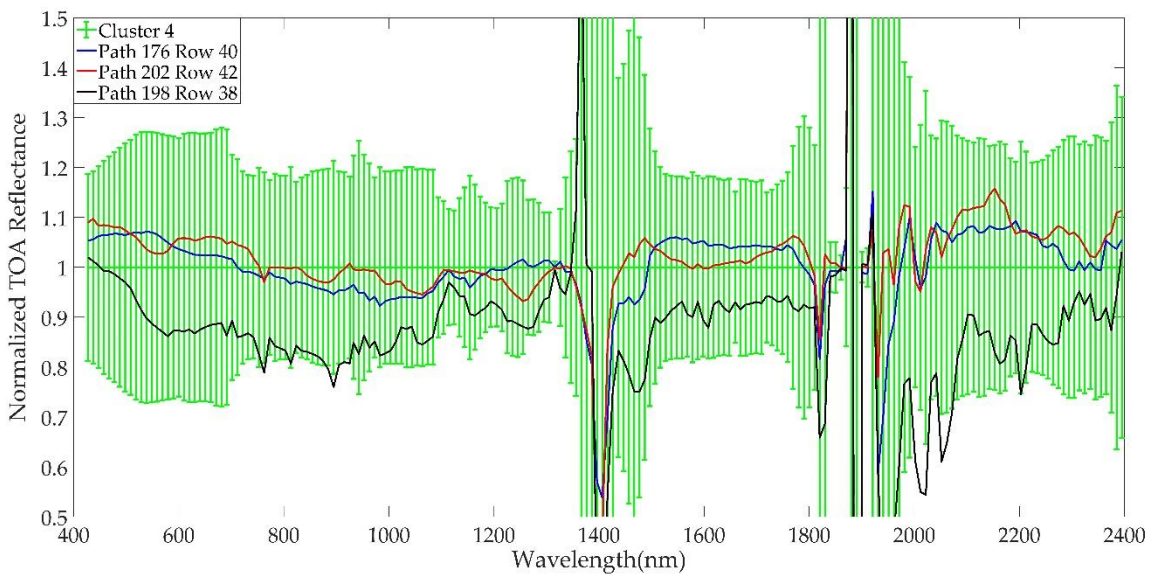


**Figure 14.** Validation of hyperspectral spectrum of Cluster 4.

Similarly, hyperspectral validation of the representative hyperspectral profile of Cluster 1 was performed by using two spectra from each of three different WRS-2 Path/Rows: 175/41, 205/44 and 190/47. Figure 15 gives the normalized hyperspectral profile of Cluster 1 (green) and the normalized spectra from the validation path/rows represented by blue, red and black. These spectra lie inside the uncertainty range of a representative hyperspectral profile of Cluster 1 implying that this estimated hyperspectral profile can be used to represent the spectrum for any of its subregions.

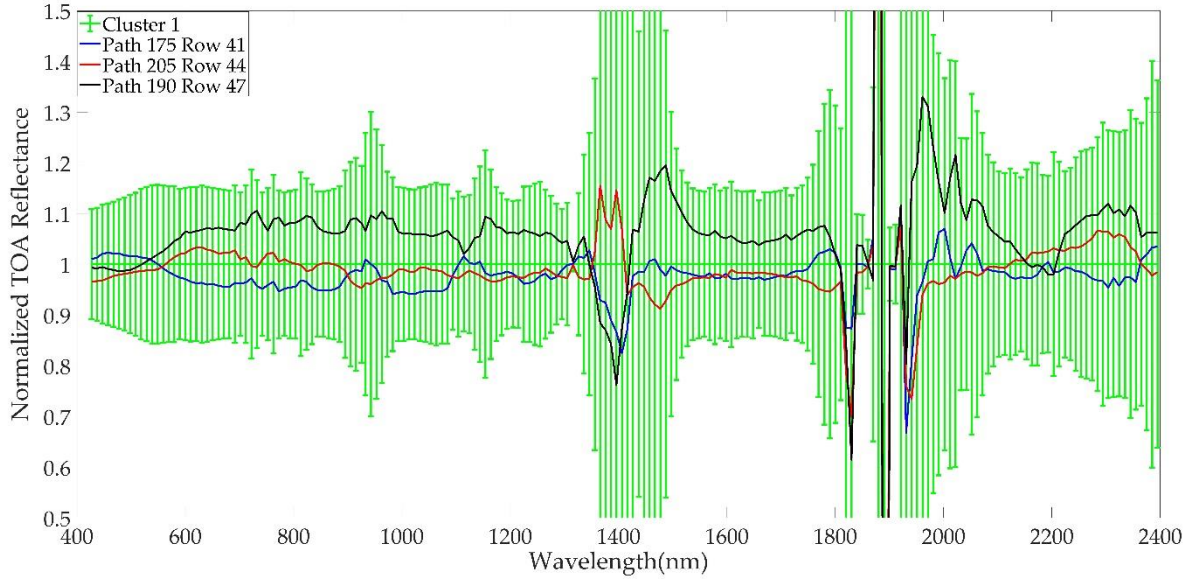


**Figure 15.** Validation of hyperspectral spectrum of Cluster 1.

### 3.7.2 Multispectral Domain

Multispectral validation was performed by comparing the SBAF derived from the hyperspectral data of Cluster 13 and the ratio of multispectral TOA reflectance from two well-calibrated sensors: Landsat 7 ETM+ and Sentinel 2A MSI. The absolute radiometric calibration uncertainty of Landsat 7 ETM+ and Sentinel 2A MSI is 5% and 3%, respectively [25, 26, 27]. It was assumed that for two well-calibrated sensors, the SBAF is equal to their TOA reflectance ratio. For a multispectral validation, the representative hyperspectral data of Cluster 13 was used and 50 near-coincident (3 days apart) Sentinel 2A MSI/Landsat 7 ETM+ scene pairs were selected from Libya 4 and Egypt 1 since both of these sites were used to estimate the hyperspectral profile of Cluster 13. Among 50 near-coincident scene pairs, 32 were from Libya 4 and the remaining 18 were from Egypt 1. Each sensor's TOA reflectance was calculated from a region common to Cluster 13 and the corresponding Hyperion images (Figure 6), Sentinel 2A MSI, and Landsat 7 ETM+ images of Libya 4 (Figures 16(a) and 16(c)) and Egypt 1 (Figures 16(b) and 16(d)).

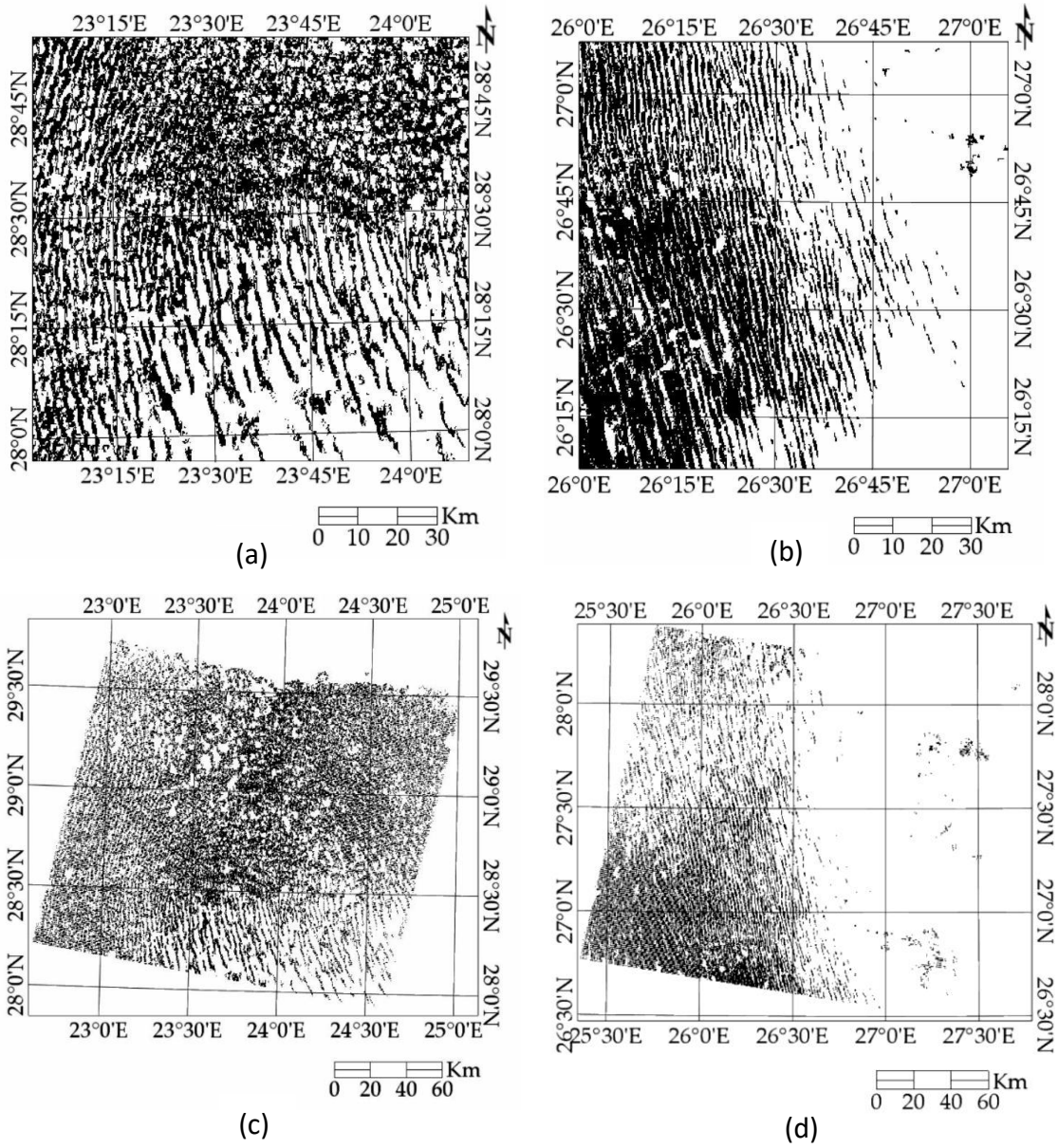


**Figure 16.** Cluster 13 binary masks (a) Sentinel 2A MSI Libya 4 (b) Sentinel 2A MSI Egypt 1 (c) Landsat 7 Libya 4 (d) Landsat 7 Egypt 1. Black color pixel represents the Cluster 13 pixels.

The multispectral SBAFs for Libya 4 and Egypt1 were calculated as the ratio of the Sentinel 2A BRDF-corrected TOA reflectance to the corresponding Landsat 7 TOA reflectances. The BRDF corrections were performed according to the model given in eq (2-3) assuming the Landsat 7 solar and sensor view geometry as the reference.

The hyperspectral SBAF for Cluster 13 was calculated as the ratio of the simulated Sentinel 2A TOA reflectances and the Landsat 7 ETM+ TOA reflectance, as follows:

$$\text{SBAF} = \frac{\rho_{\lambda, \text{Sentinel 2A}}}{\rho_{\lambda, \text{Landsat 7}}} = \frac{\frac{\int \rho_{\lambda} \text{RSR}_{\lambda}(\text{Sentinel 2A}) d\lambda}{\int \text{RSR}_{\lambda}(\text{Sentinel 2A}) d\lambda}}{\frac{\int \rho_{\lambda} \text{RSR}_{\lambda}(\text{Landsat 7}) d\lambda}{\int \text{RSR}_{\lambda}(\text{Landsat 7}) d\lambda}} \quad (5)$$

where:  $\rho_{\lambda, \text{Sentinel 2A}}$  and  $\rho_{\lambda, \text{Landsat 7}}$ , respectively, are the simulated TOA reflectance for Sentinel 2A and Landsat 7,  $\rho_{\lambda}$  is the hyperspectral profile of Cluster 13, and  $\text{RSR}_{\lambda(\text{sensor})}$  is the relative spectral response of the corresponding sensor.

Figure 17 shows the resulting simulated multispectral SBAFs between Sentinel 2A MSI/Landsat 7 ETM+ and the multispectral TOA reflectance ratios for each band, along with the corresponding  $1\sigma$  standard deviations. The error bar of the simulated multispectral SBAF is standard deviation of the SBAF calculated using 185 hyperspectral profile of Cluster 13 used to estimate the representative hyperspectral profile of Cluster 13. The error bar of the multispectral SBAF is the standard deviation of the ratio of TOA reflectance of Sentinel 2A and Landsat 7 along with their absolute radiometric uncertainty.

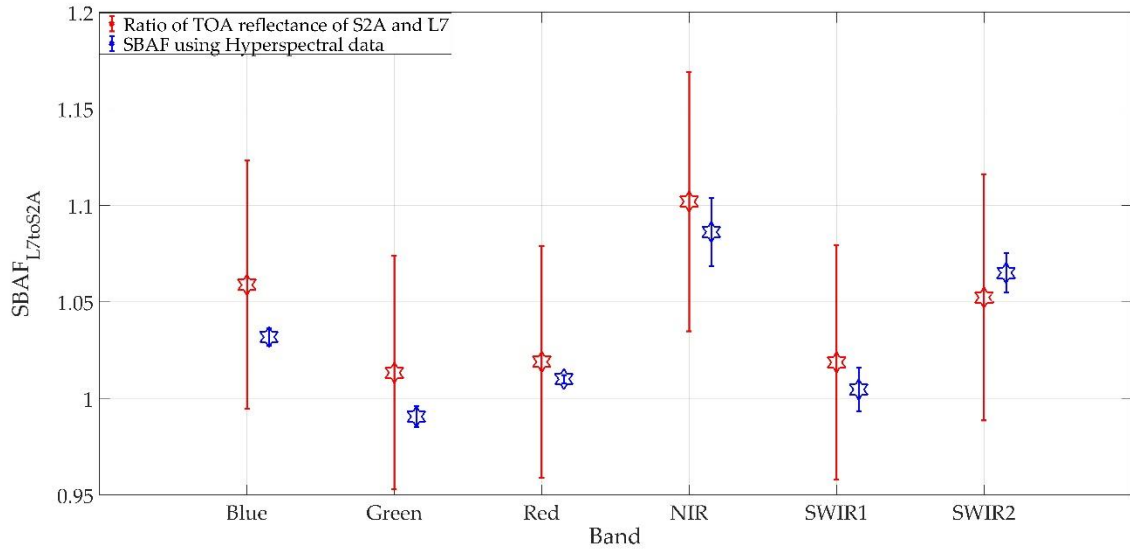


**Figure 17.** Plot of simulated multispectral SBAF / Multispectral TOA Reflectance Ratio Comparison (1 sigma).

Overall, the simulated multispectral SBAFs have lower uncertainties due to a large number of hyperspectral data of Cluster 13. The largest difference between the two can be clearly seen in Blue and Green band which is approximately 2.5% and 2.25 % whereas the Red band has the smallest different of 0.87% between the simulated multispectral SBAF, derived from hyperspectral profiles of Cluster 13, and the multispectral SBAF. Similarly, the difference between the two sets of SBAF's is approximately 1.5% for the rest of the bands. As the error bar of multispectral SBAF includes the simulated multispectral SBAF, these two sets of SBAF are statistically indistinguishable for all the bands.

#### 4. Discussion

This work focuses on estimating a representative hyperspectral profile for all clusters. With the assigned hyperspectral profile for clusters, they can be used for both EPICS based cross-calibration of optical satellite sensors and development of EPICS based absolute calibration

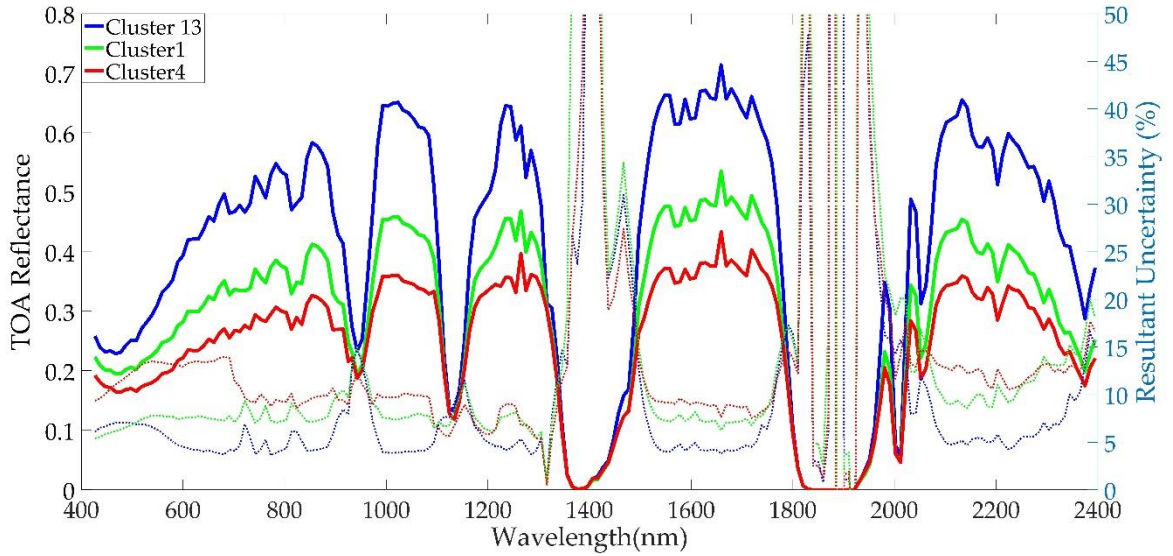
models. A representative hyperspectral profile for all the clusters was estimated by using the hyperspectral data from the intersection region of Hyperion images and corresponding clusters. The cluster images were filtered for look angles up to  $\pm 5^\circ$  and cloud cover of 10% or less, in order to reduce the uncertainty in the estimated representative hyperspectral profile. In addition to these filters, relative spectral stability of the hyperspectral profiles is also important; any change to the overall shape of the profile yields a different SBAF value, whereas any shift in the intensity level of the spectrum has no effect in SBAF calculation.

It was found that each cluster has a different number of spectra that can be used to estimate the representative hyperspectral profile of each cluster. The majority of the clusters have more than 120 filtered hyperspectral profiles as shown in Figure 3, which provides confidence for the estimated hyperspectral profile of each cluster. In addition, it was found that the largest number of pixels doesn't guarantee the largest number of hyperspectral profiles; Cluster 3 contains the largest number of pixels (4.3 million pixels), yet has only 250 useable hyperspectral profiles. Among all the clusters, Cluster 5 has the highest number of hyperspectral profiles (294), and Cluster 4 has the lowest number (71) which is still useful for estimating its hyperspectral profile.

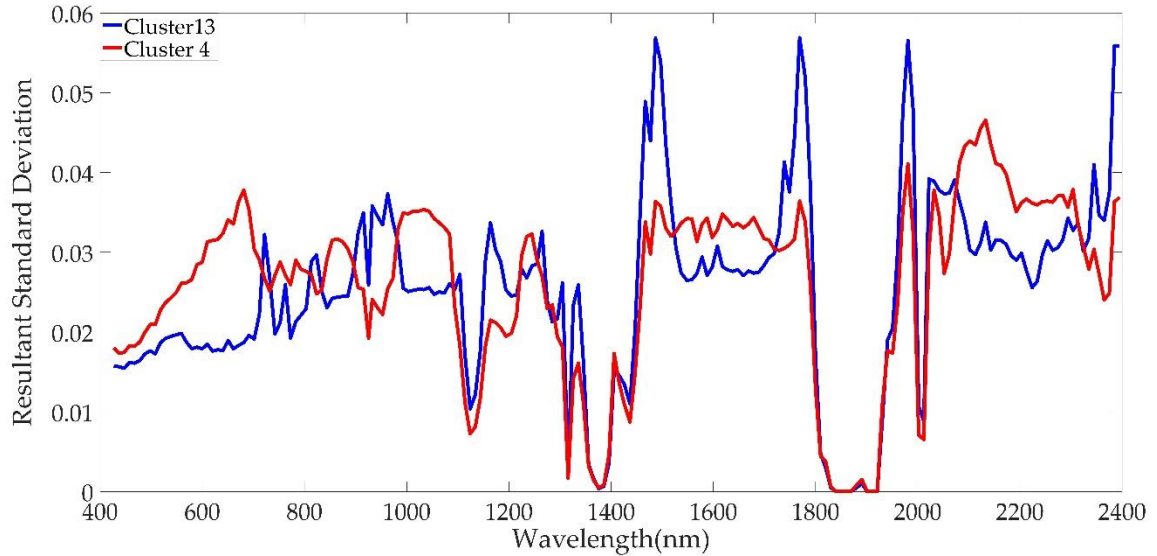
The methodology of estimating the hyperspectral profile of North African clusters was demonstrated by using Cluster 13 as it stands out as an early viable candidate for EPICS-based calibration [1]. The resultant uncertainty of the estimated hyperspectral profile of Cluster 13 is approximately 4-5% in the majority of the spectral regions. The resultant uncertainty associated with the representative hyperspectral profile is the combination of both spatial and temporal uncertainties as the representative hyperspectral profile for each cluster is estimated by using hyperspectral spectra collected from different regions of clusters over the EO-1 Hyperion lifetime. It has approximately 5% resultant uncertainty for most of the spectral regions as shown in Figure 10. It has resultant uncertainty of 6% for the wavelengths less than 600 nm which is expected as the spatial uncertainty of Cluster 13 for Coastal/Aerosol and Blue bands are approximately 5%.

Figure 18 presents the comparison of one of the brightest clusters (Cluster 13), the darkest cluster (Cluster 4) and a cluster with an intermediate intensity level. At longer wavelengths, the hyperspectral profiles exhibit more pronounced differences in intensity, providing a wider dynamic range for calibration. Among these three clusters, Cluster 13 has the lowest uncertainty (approximately 5% across all the spectral regions) and Cluster 4 has the highest uncertainty (10% across all the spectral region). The uncertainty is due to the combination of both temporal and spatial uncertainty, more driven by the spatial uncertainty of the clusters. In relative scale, the resultant uncertainty of the Cluster 4 is double to that of the Cluster 13 but in an absolute scale, both of the clusters have similar changes of 0.03 reflectance units across most of the spectral regions as shown in Figure 19.





**Figure 18.** Comparison of the hyperspectral profile of different clusters with its temporal uncertainty (1-sigma). The solid line represents a representative hyperspectral profile of a cluster and its corresponding temporal uncertainty is represented by the dotted line of the same color.



**Figure 19.** Comparison of resultant standard deviation (1 sigma) of clusters 13 and 4. The blue and red solid lines represent the resultant standard deviation of clusters 13 and 4.

Clusters 13 and 4 have approximately 5% and 12% spatial uncertainty, respectively, across the spectral regions which are expected as the initial analysis of these clusters shows a similar uncertainty level [1]. As the hyperspectral data are only filtered for relative spectral stability, hyperspectral profiles of clusters weren't filtered for temporal stability which significantly contributed to the resultant uncertainty of the estimated hyperspectral profile. Residual BRDF effects introduce some level of uncertainty into the hyperspectral profile, as the look-angle filtering and the full four-angle correction model do not provide perfect correction. In addition, BRDF

correction cannot be performed properly if the cluster doesn't have a large number of hyperspectral profiles such as Cluster 4. It has the smallest number of hyperspectral profiles (74) due to lower coverage over North Africa, suggesting that it has lower angular sampling than other clusters, which increases the uncertainty of retrieved BRDF parameters [28]. Along with all the above uncertainty, the calibration uncertainty of the EO-1 Hyperion sensor also contributes to the uncertainty of the estimated hyperspectral profiles.

During this analysis, it was observed that most of the hyperspectral profiles of all the clusters are relatively stable over time. Overall, the spectral stability of the representative hyperspectral spectrum of each cluster is similar from 600 nm to 2200 nm as shown in Figure 18 and Appendix A. The representative hyperspectral profile of Clusters 13, 5, 8, 12, 15, and 17 have more resultant uncertainty at spectral range of approximately less than 600 nm than the majority region of the spectrum, i.e. 600–2200 nm. The remaining cluster's representative hyperspectral profiles have similar resultant uncertainty across the entire wavelength range from 400 nm to 2100 nm. For all the clusters, the resultant uncertainty of the wavelengths higher than 2200 nm has very high resultant uncertainty, almost increasing exponentially as a function of wavelength.

Validation of the representative spectrum data of Cluster 13 was done in both the hyperspectral and multispectral domains. For hyperspectral validation of Cluster 13, six different regions were chosen and hyperspectral spectra from these selected regions were compared with the representative hyperspectral profile of Cluster 13. These hyperspectral profiles from the six regions spectral all lie within the uncertainty of the representative hyperspectral profile of Cluster 13. There is more deviation between the representative and validating spectra of Cluster 13 at the wavelengths less than 600 nm and more than 2000 nm than in the rest of the spectral regions as shown in Figure 13. In contrast, the deviation between the validation and representative spectra of Clusters 1 and 4 is similar across the entire spectral range as shown in Figures 14 and 15.

Similarly, for multispectral validation, 50 near-coincident scene pairs between Sentinel 2A MSI and Landsat 7 ETM+ and the representative hyperspectral profile of Cluster 13 were used. The simulated multispectral SBAF calculated using the representative hyperspectral of Cluster 13 was compared to the multispectral SBAFs (ratio of multispectral TOA reflectance of Sentinel 2A MSI and Landsat 7 ETM+). Blue and Green bands had the largest difference of approximately 2.5% and 2.25% respectively, and the Red band has the smallest difference of approximately 0.87%. These differences are driven by various factors such as spatial uncertainty of Cluster 13, atmospheric uncertainty, BRDF effects and the calibration of the sensors. As the error bar of multispectral SBAF includes the simulated multispectral SBAF, these two sets of SBAF are statistically indistinguishable for all the bands.

Figure 20 presents the mean resultant uncertainty of the representative hyperspectral profile for each North African cluster. The mean resultant uncertainty was calculated by taking the average resultant uncertainty across all the transmission bands. Since the absorption bands are loosely filtered out, it includes the uncertainty of some of the transition bands across different spectral regions; consequently, the temporal uncertainty is exaggerated and overestimated by approximately 2-3%. For example, Cluster 13 has approximately 5% resultant uncertainty across the majority of its spectral regions, but the mean resultant uncertainty is estimated as approximately 8% in Figure 20.

Figure 20 shows that a representative hyperspectral profile of Clusters 15 and 4 has the lowest and highest resultant uncertainty, respectively. Cluster 15 is one of the brightest clusters and it spreads wide across North Africa resulting in 166 spectra which helps to estimate a more stable spectrum. Similarly, other clusters such as Clusters 13, 2, 5, and 8 also have comparable uncertainties of approximately 7-8%. The majority of the clusters exhibiting higher uncertainty has lower intensity levels, such as Clusters 1 and 4. As uncertainty is a relative measurement, for the

same amount of change in absolute scale, the relative measurement (uncertainty) is higher for the clusters having low intensity than for the clusters having high intensity.

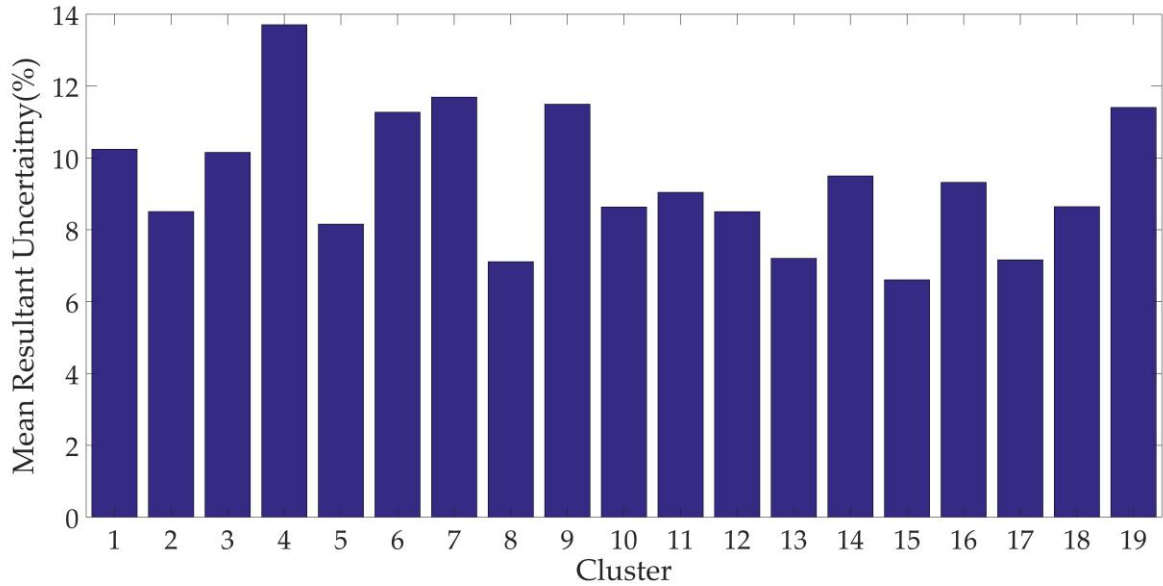


**Figure 20.** Comparison of temporal uncertainty of all 19 clusters of North Africa.

Identification of widespread clusters within North Africa provides a great opportunity to improve PICS-based calibration, as the cluster regions tend to cover much greater areas than the ROIs used in traditional PICS calibration. Overall, the uncertainties of most clusters are within 5% and some are around 10%; but still all are usable for moving from ROI-based PICS calibration to Cluster-based PICS calibration.

Potential extensions to the present work include the following:

1. Perform EPICS based cross-calibration and compare it to the cross-calibration gain and bias obtained from an ROI-based cross-calibration approach.
2. Generate a cluster-based absolute calibration model and compare its performance to the current absolute calibration model derived for an individual PICS. In contrast to the current approach, the cluster-based approach could potentially offer calibration of any optical satellite sensor on a daily or near-daily basis.

## 5. Conclusions

A large number of satellite sensors has been launched to monitor changes on the Earth surface. To take advantage of their data, they should be calibrated to a common radiometric scale. Cross-calibration of optical satellite sensors helps to put data from multiple sensors to a common radiometric scale by transferring the calibration from a well-calibrated sensor to an uncalibrated sensor using coincident or near-coincident observations of various targets on the Earth's surface selected for their temporal stability. Accurate hyperspectral characterization of a target is mandatory for performing cross-calibration as it is used for generating the SBAF required to compensate for differences in relative spectral response (RSR) between sensors.

This work presented a methodology to estimate representative hyperspectral profiles for previously derived clusters of North Africa. Cluster 13 was initially chosen to demonstrate the methodology as it possessed the largest contiguous regions that were widely distributed across



North Africa. It also exhibited the lowest overall spatial uncertainty across the VNIR and SWIR spectral range, as well as partial inclusion of the well-known Libya 4 and Egypt 1 PICS within its sub-regions.

The “representative” hyperspectral profile for Cluster 13 in North Africa was estimated for potential use as an extended PICS (EPICS), using 185 hyperspectral profiles derived from 15 WRS-2 Path/Row Hyperion images acquired over its lifetime. The profile exhibited an uncertainty of approximately 5% across all the spectral regions.

Data from WRS-2 Path/Row 182/42, 198/47, 192/38, 178/43, 185/48 and 200/47 were then used to validate the estimated profiles. As the spectra from the selected paths and rows fell within the uncertainty range of the Cluster 13 spectrum, these were used as the “representative” Cluster 13 spectrum. For validation from a multispectral banded perspective, simulated multispectral SBAFs derived from the hyperspectral data were compared to BRDF-corrected multispectral SBAFs (specified as the ratio of TOA reflectance from two well-calibrated sensors). As the error bar of the multispectral SBAFs for MSI and ETM+ includes the simulated multispectral SBAF, these two sets of SBAF are statistically indistinguishable.

Most of the rest of the clusters of North Africa exhibit a resultant uncertainty from 5-12%. Among them, Cluster 15 has the lowest resultant uncertainty of 5% whereas Cluster 4 has the highest uncertainty of around 12 %. The major source of uncertainty of the estimated hyperspectral profile is the spatial uncertainty of the cluster itself determined by the threshold used for the initial analysis of the classification of North Africa. In addition, temporal uncertainty of EPICS, residual BRDF effects, and Hyperion calibration uncertainty also contributed some of the resultant uncertainty.

With an accurate hyperspectral signature, any sub-region within Cluster 13 can be used for cross-calibration of optical satellite sensors and also for building an absolute calibration model. Furthermore, hyperspectral profiles for all the clusters found by Shrestha et al. [1], are estimated using a similar methodology, and vast regions of North Africa can be used as EPICS for performing sensor cross-calibration. Using EPICS, the number of coincident and near-coincident scene pairs between sensors to be calibrated is significantly larger than the number obtained using the traditional PICS approach. There is potential that EPICS-based sensor cross-calibration can deliver results of similar or higher quality within a much shorter timeframe than the traditional cross-calibration approach. Furthermore, EPICS-based absolute calibration models will have a significantly larger number of observations which will help to improve the accuracy and consistency of the resulting calibration.

**Author Contributions:** M.S conceived the research, developed the algorithm with the help of L.L and D.H. M.S, L.L, and D.H analyzed the data, NH generated binary mask to filter in the desired pixel of a cluster, M.S wrote the paper; and L.L and D.H edited the paper.

**Funding:** This research was funded by NASA (grant number NNX15AP36A) and USGS EROS (grant number G14AC00370).

**Acknowledgments:** The authors would like to thank Thomas Loveland for putting his insight to improve this work and Tim Ruggles for editing the manuscript.

**Conflicts of Interest:** The authors declare no conflict of interest.

## Appendix A

In this appendix, we include the estimated representative hyperspectral profile of remaining clusters of North Africa.

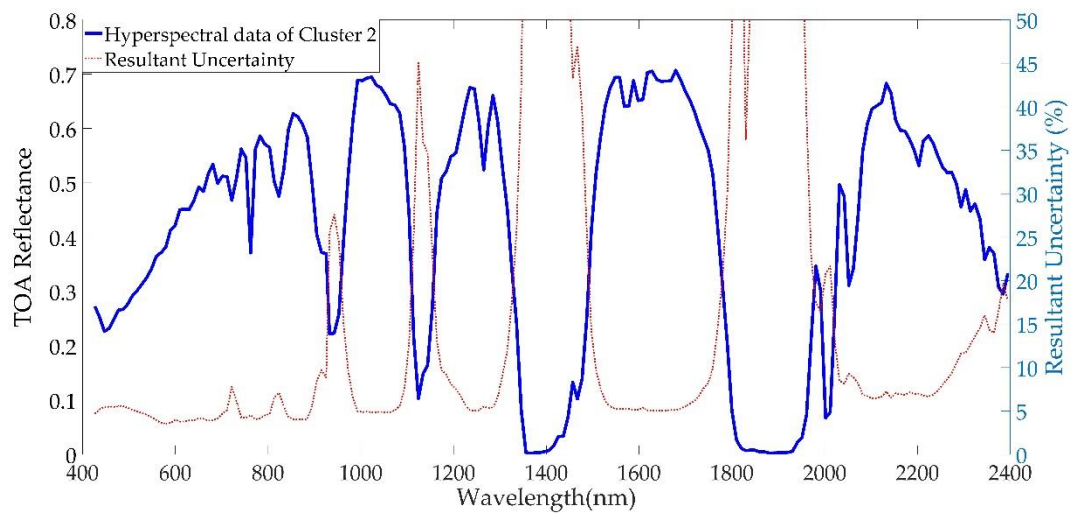


**Figure A1.** Estimated representative hyperspectral profile of Cluster 2 and its resultant uncertainty.

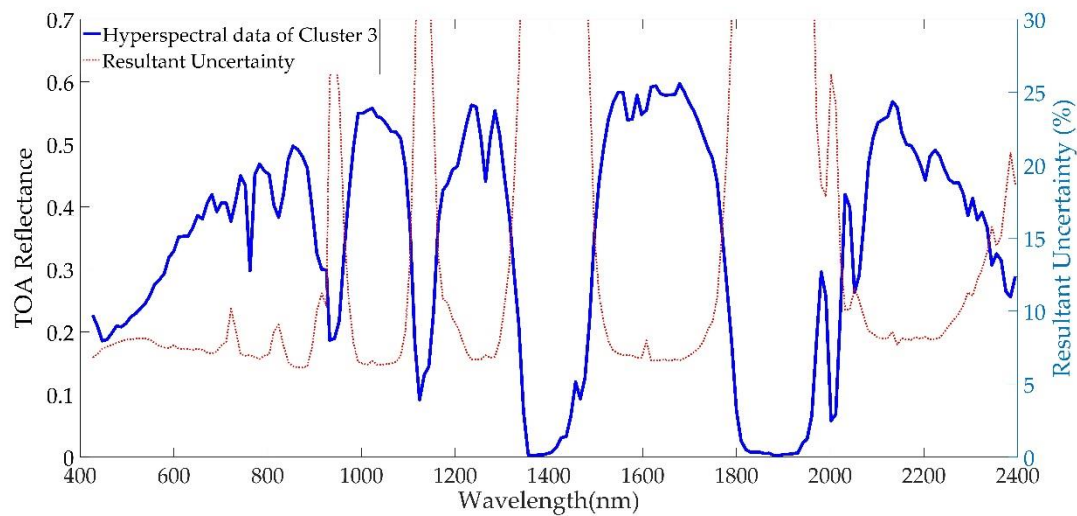


**Figure A2.** Estimated representative hyperspectral profile of Cluster 3 and its resultant uncertainty.

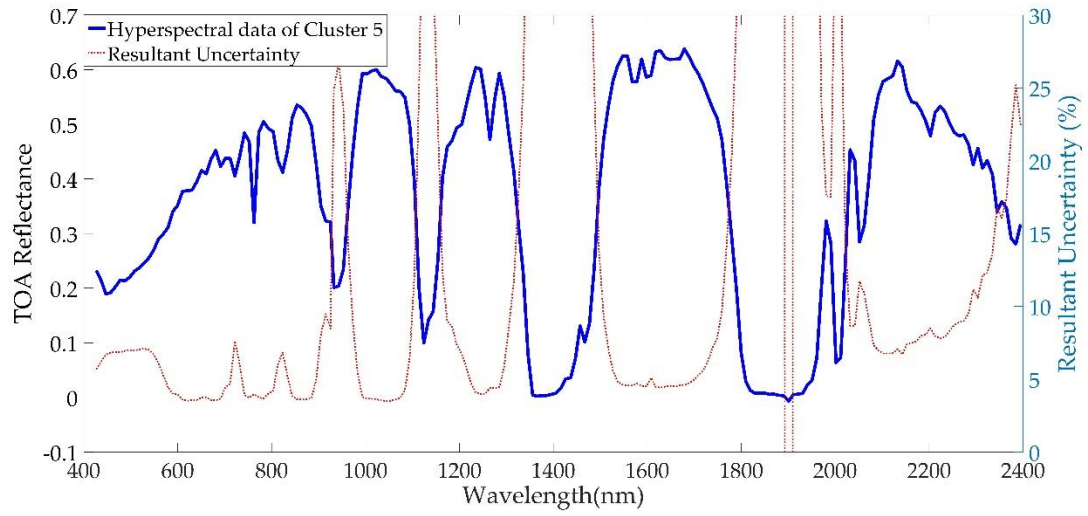


**Figure A3.** Estimated representative hyperspectral profile of Cluster 5 and its resultant uncertainty.

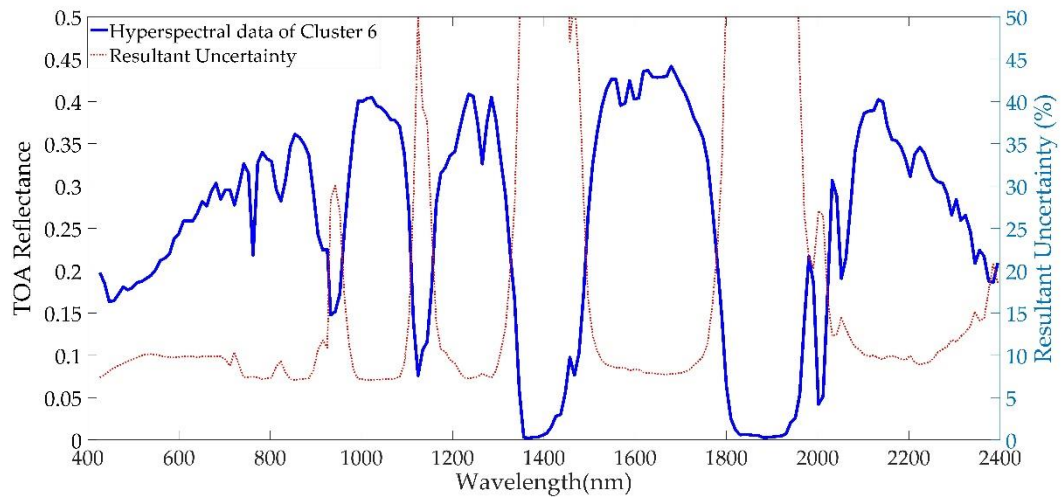


**Figure A4.** Estimated representative hyperspectral profile of Cluster 6 and its resultant uncertainty.

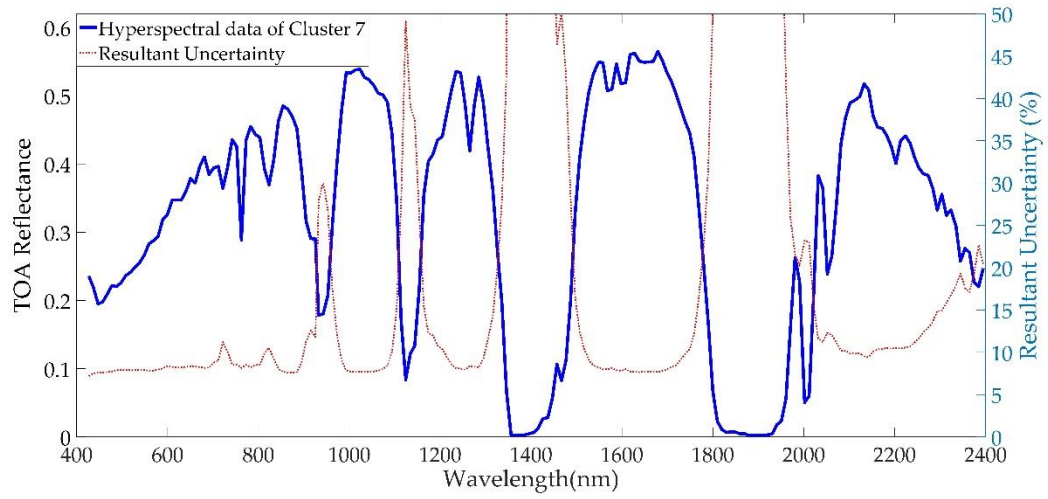


**Figure A5.** Estimated representative hyperspectral profile of Cluster 7 and its resultant uncertainty.

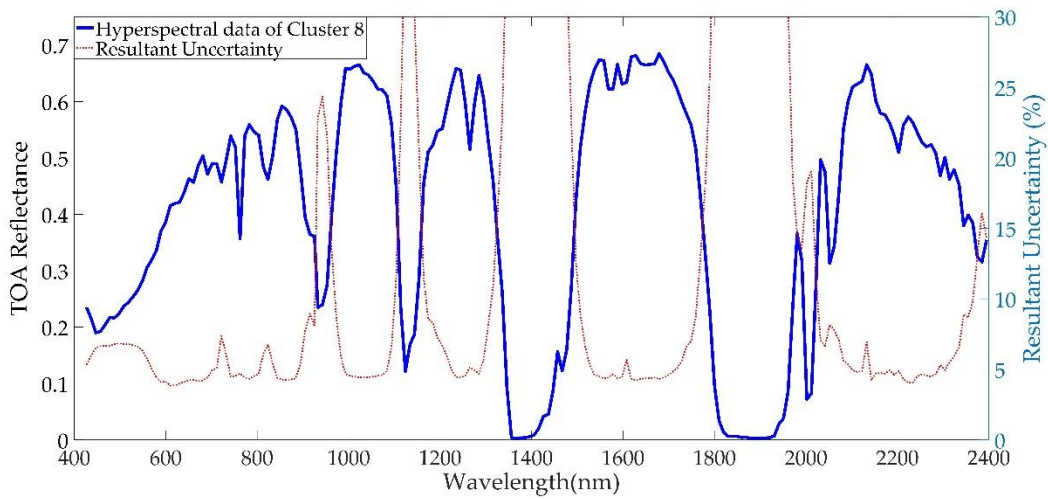


**Figure A6.** Estimated representative hyperspectral profile of Cluster 8 and its resultant uncertainty.

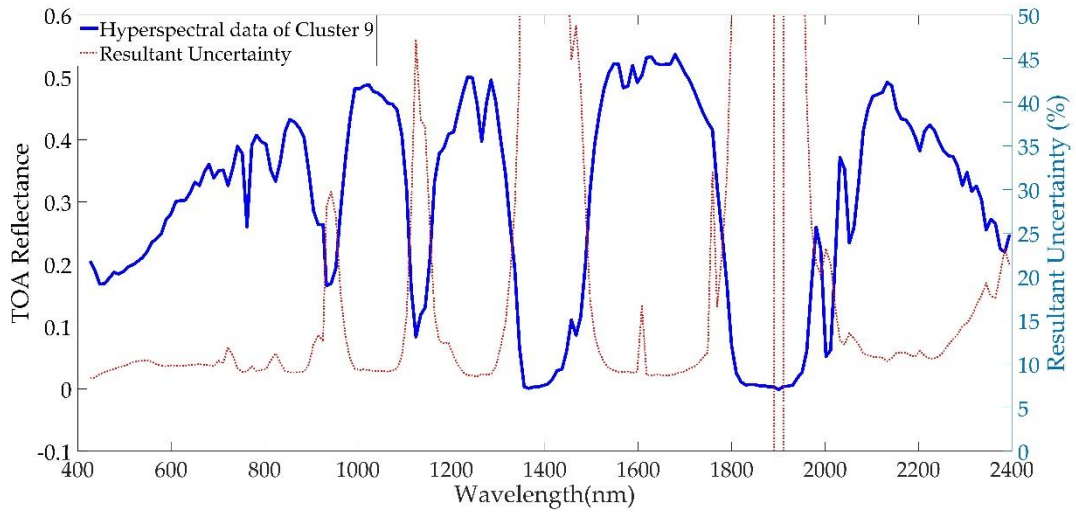


**Figure A7.** Estimated representative hyperspectral profile of Cluster 9 and its resultant uncertainty.

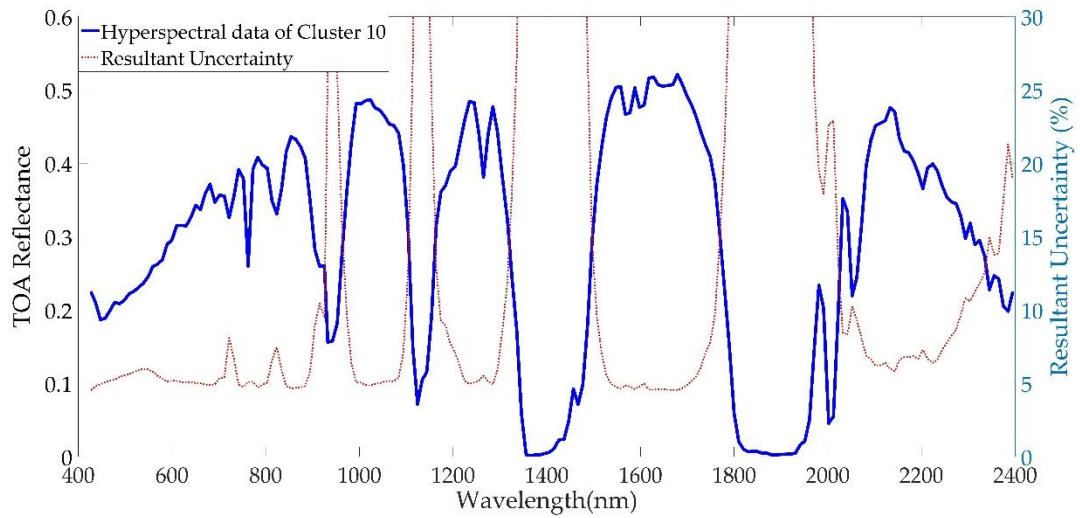


**Figure A8.** Estimated representative hyperspectral profile of Cluster 10 and its resultant uncertainty.

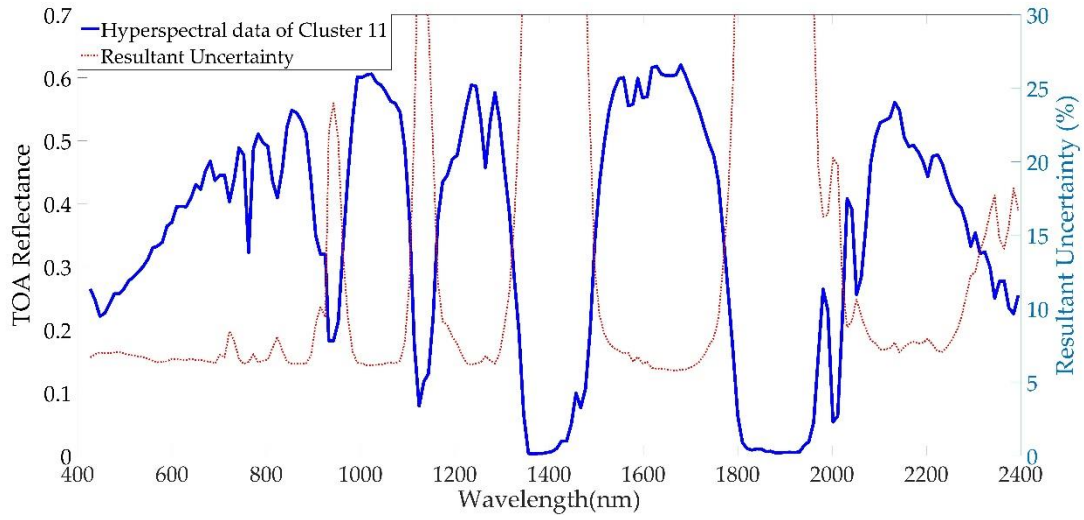


**Figure A9.** Estimated representative hyperspectral profile of Cluster 11 and its resultant uncertainty.

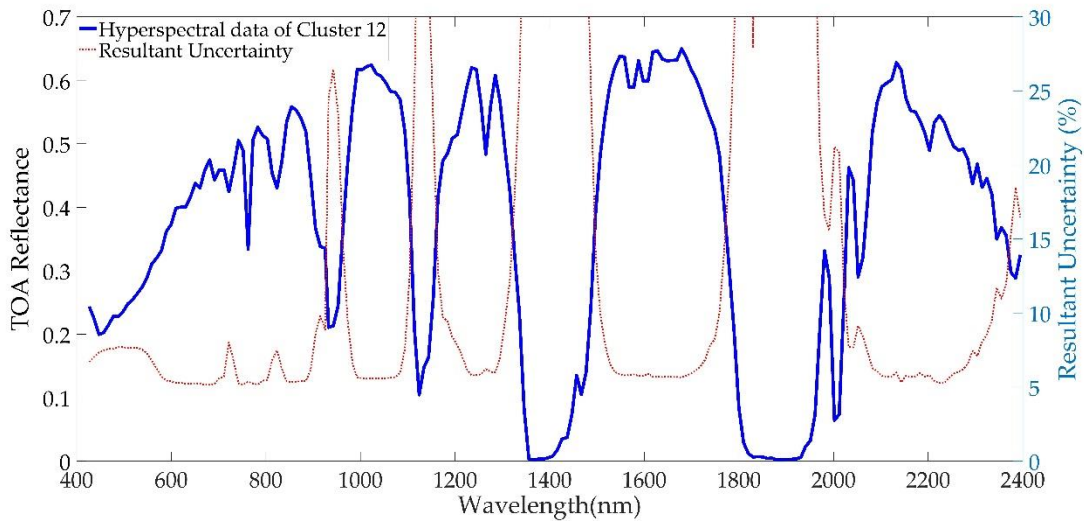


**Figure A10.** Estimated representative hyperspectral profile of Cluster 12 and its resultant uncertainty.



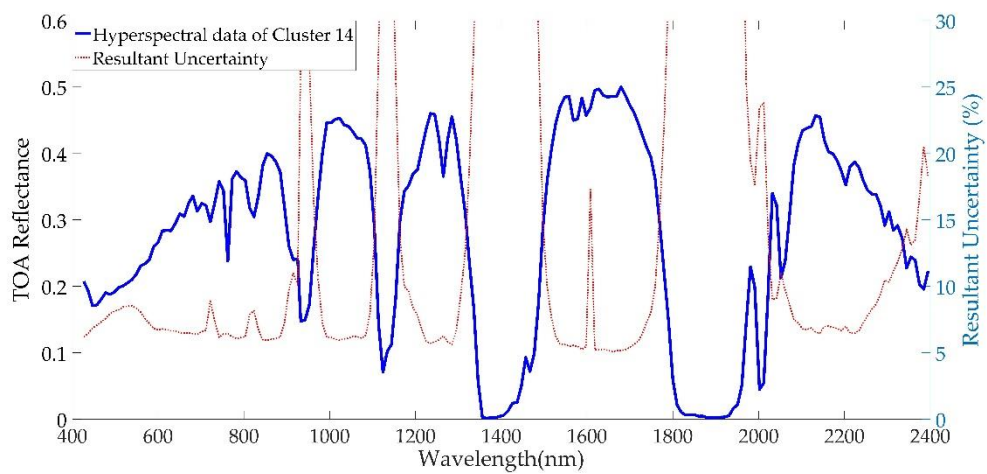


**Figure A11.** Estimated representative hyperspectral profile of Cluster 14 and its resultant uncertainty.

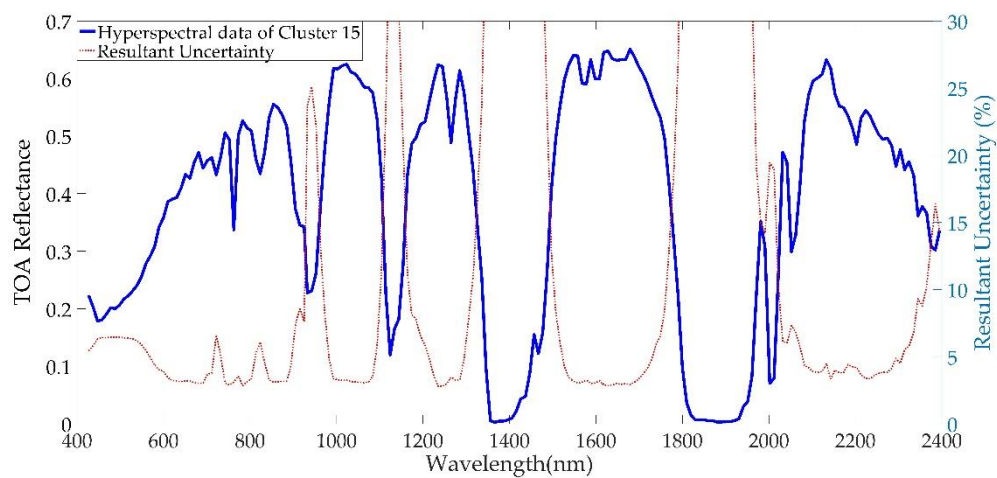


**Figure A12.** Estimated representative hyperspectral profile of Cluster 15 and its resultant uncertainty.

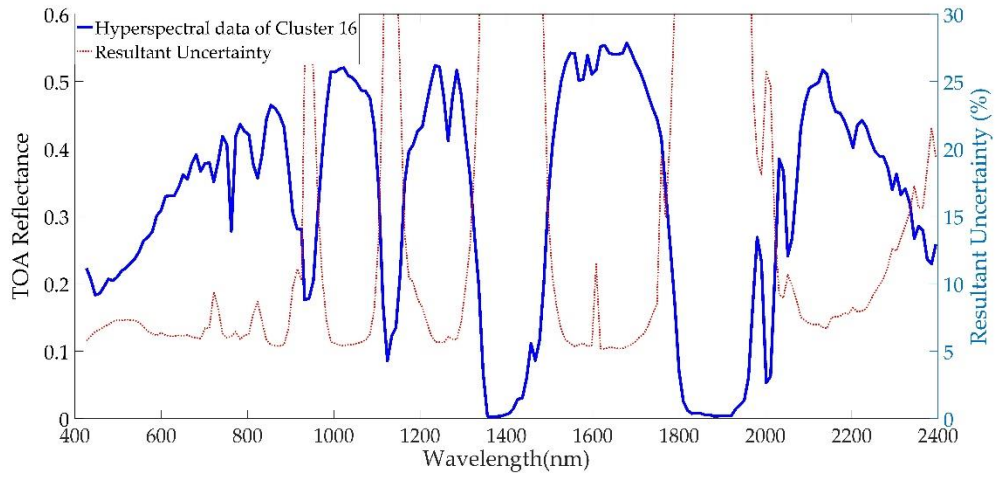


**Figure A13.** Estimated representative hyperspectral profile of Cluster 16 and its resultant uncertainty.

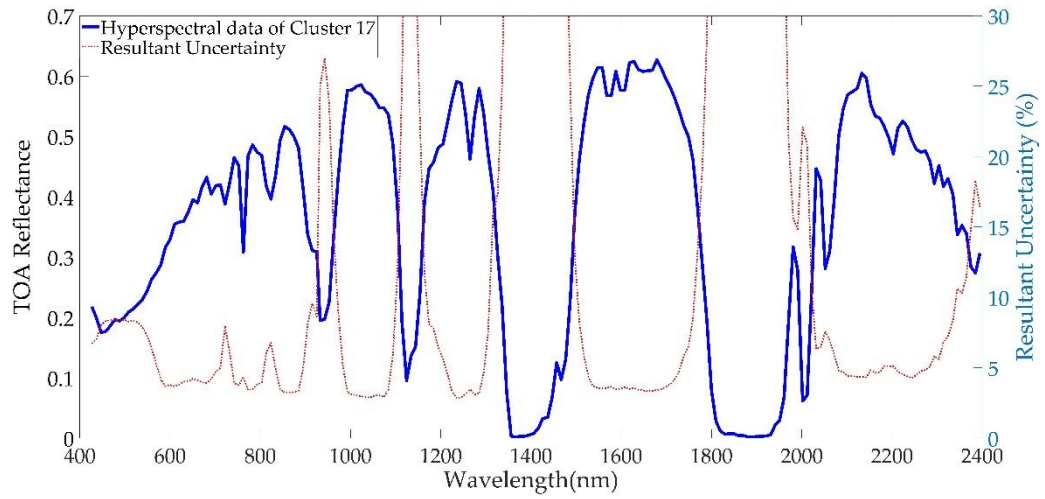


**Figure A14.** Estimated representative hyperspectral profile of Cluster 17 and its resultant uncertainty.



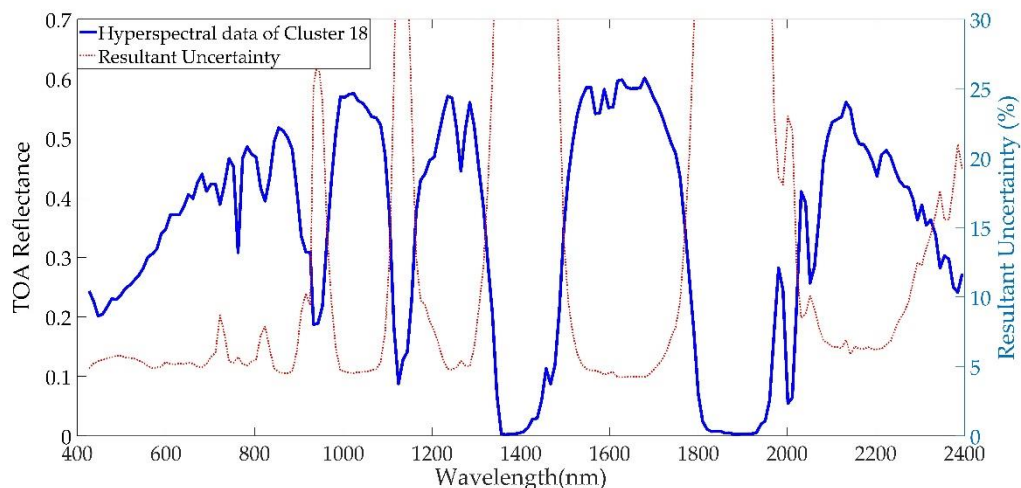


**Figure A15.** Estimated representative hyperspectral profile of Cluster 18 and its resultant uncertainty.

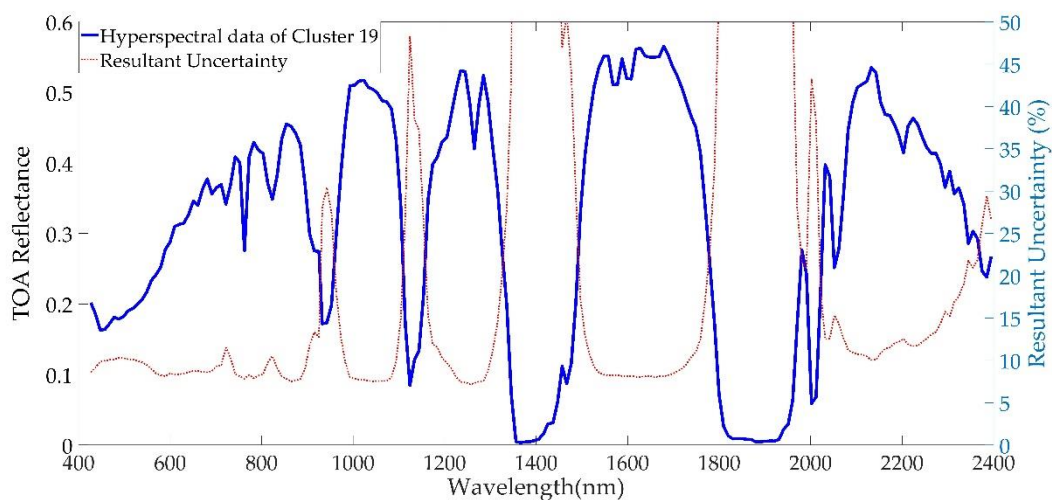


**Figure A16.** Estimated representative hyperspectral profile of Cluster 19 and its resultant uncertainty.

#### References:

1. Shrestha, M.; Leigh, L.; Helder, D. Classification of the North Africa Region for Use as an Extended Pseudo Invariant Calibration Sites (EPICS) for Radiometric Calibration and Stability Monitoring of Optical Satellite Sensors. *Remote Sensing* **2019**, *11*, 875.
2. Chander, G.; Mishra, N.; Helder, D.L.; Aaron, D.B.; Angal, A.; Choi, T.; Xiong, X.; Doelling, D.R. Applications of spectral band adjustment factors (SBAF) for cross-calibration. *IEEE Transactions on Geoscience and Remote Sensing* **2013**, *51*, 1267-1281.
3. Lacherade, S.; Fournie, B.; Henry, P.; Gamet, P. Cross calibration over desert sites: Description, methodology, and operational implementation. *IEEE Transactions on Geoscience Remote Sensing* **2013**, *51*, 1098-1113.
4. Helder, D.; Thome, K.J.; Mishra, N.; Chander, G.; Xiong, X.; Angal, A.; Choi, T. Absolute radiometric calibration of Landsat using a pseudo invariant calibration site. *IEEE Transactions on Geoscience and Remote Sensing* **2013**, *51*, 1360-1369.

5. Mishra, N.; Helder, D.; Angal, A.; Choi, J.; Xiong, X. Absolute calibration of optical satellite sensors using Libya 4 pseudo invariant calibration site. *Remote Sensing* **2014**, *6*, 1327-1346.
6. Folkman, M.A.; Pearlman, J.; Liao, L.B.; Jarecke, P.J. In *EO-1/Hyperion hyperspectral imager design, development, characterization, and calibration*, Hyperspectral Remote Sensing of the Land and Atmosphere, 2001; International Society for Optics and Photonics: 2001; pp. 40-52.
7. Pearlman, J.; Segal, C.; Liao, L.B.; Carman, S.L.; Folkman, M.A.; Browne, W.; Ong, L.; Ungar, S.G. In *Development and operations of the EO-1 Hyperion imaging spectrometer*, Earth Observing Systems V, 2000; International Society for Optics and Photonics: 2000; pp. 243-254.
8. Franks, S.; Neigh, C.S.; Campbell, P.K.; Sun, G.; Yao, T.; Zhang, Q.; Huemmrich, K.F.; Middleton, E.M.; Ungar, S.G.; Frye, S.W. EO-1 Data Quality and Sensor Stability with Changing Orbital Precession at the End of a 16 Year Mission. *Remote sensing* **2017**, *9*, 412.
9. Biggar, S.F.; Thome, K.J.; Wisniewski, W. Vicarious radiometric calibration of EO-1 sensors by reference to high-reflectance ground targets. *IEEE Transactions on Geoscience Remote Sensing* **2003**, *41*, 1174-1179.
10. Green, R.O.; Pavri, B.E.; Chrien, T.G. On-orbit radiometric and spectral calibration characteristics of EO-1 Hyperion derived with an underflight of AVIRIS and in situ measurements at Salar de Arizaro, Argentina. *IEEE Transactions on Geoscience Remote Sensing* **2003**, *41*, 1194-1203.
11. Ungar, S.G.; Pearlman, J.S.; Mendenhall, J.A.; Reuter, D. Overview of the earth observing one (EO-1) mission. *IEEE Transactions on Geoscience Remote Sensing* **2003**, *41*, 1149-1159.
12. Pearlman, J.S.; Barry, P.S.; Segal, C.C.; Shepanski, J.; Beiso, D.; Carman, S.L. Hyperion, a space-based imaging spectrometer. *IEEE Transactions on Geoscience and Remote Sensing* **2003**, *41*, 1160-1173.
13. McCorkel, J.; Thome, K.; Ong, L. Vicarious calibration of EO-1 Hyperion. *IEEE Journal of Selected Topics in Applied Earth Observations Remote Sensing* **2013**, *6*, 400-407.
14. Campbell, P.K.E.; Middleton, E.M.; Thome, K.J.; Kokaly, R.F.; Huemmrich, K.F.; Lagomasino, D.; Novick, K.A.; Brunsell, N.A. EO-1 hyperion reflectance time series at calibration and validation sites: Stability and sensitivity to seasonal dynamics. *IEEE Journal of Selected Topics in Applied Earth Observations Remote Sensing* **2013**, *6*, 276-290.
15. Czapla-Myers, J.; Ong, L.; Thome, K.; McCorkel, J. Validation of EO-1 Hyperion and Advanced Land Imager Using the Radiometric Calibration Test Site at Railroad Valley, Nevada. *IEEE Journal Of Selected Topics In Applied Earth Observations Remote Sensing* **2016**, *9*, 816-826.
16. Jing, X.; Leigh, L.; Helder, D.; Aaron, D.; Pinto, C.T. Lifetime Absolute Calibration of the EO-1 Hyperion Sensor and its Validation. *IEEE Transactions on Geoscience and Remote Sensing (TGRS)* 2019 (In Press).
17. Angal, A.; Choi, T.; Chander, G.; Xiong, X. In *Monitoring on-orbit stability of Terra MODIS and Landsat 7 ETM+ reflective solar bands using Railroad Valley Playa, Nevada (RVPN) test site*, Geoscience and Remote Sensing Symposium, 2008. IGARSS 2008. IEEE International, 2008; IEEE: 2008; pp. IV-1364-IV-1367.
18. Chander, G.; Xiong, X.J.; Choi, T.J.; Angal, A. Monitoring on-orbit calibration stability of the Terra MODIS and Landsat 7 ETM+ sensors using pseudo-invariant test sites. *Remote Sensing of Environment* **2010**, *114*, 925-939.
19. Roy, D.P.; Zhang, H.; Ju, J.; Gomez-Dans, J.L.; Lewis, P.E.; Schaaf, C.; Sun, Q.; Li, J.; Huang, H.; Kovalsky, V. A general method to normalize Landsat reflectance data to nadir BRDF adjusted reflectance. *Remote Sensing of Environment* **2016**, *176*, 255-271.
20. Chander, G.; Mishra, N.; Helder, D.L.; Aaron, D.B.; Angal, A.; Choi, T.; Xiong, X.; Doelling, D.R.I.T.O.G.; Sensing, R. Applications of spectral band adjustment factors (SBAF) for cross-calibration. *IEEE Transactions on Geoscience Remote Sensing* **2013**, *51*, 1267-1281.
21. Liu, J.-J.; Li, Z.; Qiao, Y.-L.; Liu, Y.-J.; Zhang, Y.-X. A new method for cross-calibration of two satellite sensors. *International Journal of Remote Sensing* **2004**, *25*, 5267-5281.
22. Roujean, J.L.; Leroy, M.; Deschamps, P.Y. A bidirectional reflectance model of the Earth's surface for the correction of remote sensing data. *Journal of Geophysical Research: Atmospheres* **1992**, *97*, 20455-20468.

23. Wu, A.; Xiong, X.; Cao, C.; Angal, A. In *Monitoring MODIS calibration stability of visible and near-IR bands from observed top-of-atmosphere BRDF-normalized reflectances over Libyan Desert and Antarctic surfaces*, Earth Observing Systems XIII, 2008; International Society for Optics and Photonics: 2008; p. 708113.
24. Farhad, M.M. Cross Calibration and Validation of Landsat 8 OLI and Sentinel 2A MSI. South Dakota State University: Country, 2018.
25. Markham, B.L.; Thome, K.J.; Barsi, J.A.; Kaita, E.; Helder, D.L.; Barker, J.L.; Scaramuzza, P.L. Landsat-7 ETM+ on-orbit reflective-band radiometric stability and absolute calibration. *Transactions on Geoscience Remote Sensing* **2004**, 42, 2810-2820.
26. Gascon, F.; Bouzinac, C.; Thépaut, O.; Jung, M.; Francesconi, B.; Louis, J.; Lonjou, V.; Lafrance, B.; Massera, S.; Gaudel-Vacaresse, A. Copernicus Sentinel-2A calibration and products validation status. *Remote Sensing* **2017**, 9, 584.
27. Markham, B.L.; Haque, M.O.; Barsi, J.A.; Micijevic, E.; Helder, D.L.; Thome, K.J.; Aaron, D.; Czapla-Myers, J.S. Landsat-7 ETM+: 12 years on-orbit reflective-band radiometric performance. *IEEE transactions on geoscience remote sensing* **2012**, 50, 2056-2062.
28. Franch, B.; Vermote, E.; Skakun, S.; Roger, J.-C.; Masek, J.; Ju, J.; Villaescusa-Nadal, J.L.; Santamaria-Artigas, A. A Method for Landsat and Sentinel 2 (HLS) BRDF Normalization. *Remote Sensing* **2019**, 11, 632.



1. © 2019 by the authors. Submitted for possible open access publication under the terms and conditions of the Creative Commons Attribution (CC BY) license (<http://creativecommons.org/licenses/by/4.0/>).

Article

# Extended Pseudo Invariant Calibration Sites (EPICS) for the Cross-Calibration of Optical Satellite Sensors

Mahesh Shrestha, Md. Nahid Hasan, Larry Leigh, Dennis Helder\*

Department of Electrical Engineering and Computer Science, South Dakota State University (SDSU), Brookings, SD 57007, USA; mahesh.shrestha@sdstate.edu (M.S.), mdnahid.hasan@sdstate.edu (N.H.), larry.leigh@sdstate.edu (L.L.)

\* Correspondence: Correspondence: dennis.helder@sdstate.edu (D.H.); Tel.: +01-605-688-4372

Received: 20 May 2019; Accepted: date; Published: date

**Abstract:** An increasing number of Earth-observing satellite sensors are being launched to meet the insatiable demand for timely and accurate data to aid the understanding of the Earth's complex systems and to monitor significant changes to them. To make full use of the data from these sensors, it is mandatory to bring them to a common radiometric scale through a cross-calibration approach. Commonly, cross-calibration data were acquired from selected pseudo-invariant calibration sites (PICS), located primarily throughout the Saharan desert in North Africa, determined to be temporally, spatially, and spectrally stable. The major limitation to this approach is that long periods of time are required to assemble sufficiently sampled cloud-free cross-calibration datasets. Recently, Shrestha et al. identified extended, cluster-based sites potentially suitable for PICS-based cross-calibration and estimated representative hyperspectral profiles for them. This work investigates the performance of extended pseudo-invariant calibration sites (EPICS) in cross-calibration for one of Shrestha's clusters, Cluster 13, by comparing its results to those obtained from a traditional PICS-based cross-calibration. The use of EPICS clusters can significantly increase the number of cross-calibration opportunities within a much shorter time period. The cross-calibration gain ratio estimated using a cluster-based approach had a similar accuracy to the cross-calibration gain derived from region of interest (ROI)-based approaches. The cluster-based cross-calibration gain ratio is consistent within approximately 2% of the ROI-based cross-calibration gain ratio for all bands except for the coastal and shortwave-infrared (SWIR) 2 bands. These results show that image data from any region within Cluster 13 can be used for sensor cross-calibration.

**Keywords:** Extended pseudo invariant calibration sites (EPICS); cross-calibration; Landsat 8 OLI; Sentinel 2A MSI

---

## 1. Introduction

An increasing number of satellites have been launched to measure the solar energy reflected by the Earth and to study changes on the Earth's surface. It is certain that the amount of data they generate will significantly increase over time. To utilize different satellite sensor data for the quantitative study of the Earth's surface, accurate radiometric calibration will be crucial for maintaining a common radiometric scale between them [1]. In general, radiometric calibration approaches consist of three major types: Prelaunch calibration, onboard calibration, and vicarious calibration [2, 3]. Prelaunch calibration is performed in the laboratory prior to launch. Onboard

calibration is performed after launch and regularly throughout a sensor's operating lifetime, using onboard sources such as lamps, solar diffuser panels, and even the moon for lunar calibration [4]. Vicarious calibration is also typically performed after launch throughout a sensor's operating lifetime and is based on the analysis of Earth imagery of selected target locations. Vicarious calibration can be achieved through i) surface radiance/reflectance-based approaches [5, 6, 7, 8, 9] and ii) cross-calibration approaches between multiple sensors [10, 11, 12]. Many satellite sensor systems, such as Landsat sensors, possess onboard calibration sources. Sensors which do not, typically due to additional design and mission operating costs, must rely on vicarious calibration techniques to achieve radiometric calibration.

Radiance/reflectance-based vicarious calibration methods are based on the coincident measurements of a target's surface radiance/reflectance during sensor overpass. The surface measurements are fed into a radiative transfer code (e.g., Moderate resolution atmospheric transmission (MODTRAN)) that predicts the top of atmosphere (TOA) radiance/reflectance. The predicted TOA measurement is compared to the corresponding radiance/reflectance recorded by the sensor in order to obtain radiometric calibration gains and biases for different sensor bands.

Cross-calibration provides a more indirect vicarious calibration approach based on the analysis of cloud-free imagery from selected targets coincidently (or near coincidently) acquired by two or more sensors, one of which possesses an established radiometric calibration to use as a reference. The following sections present this approach in greater detail in the context of cross-calibration using scene pairs acquired over pseudo-invariant calibration sites (PICS).

### *1.1. Pseudo-Invariant Calibration Sites (PICS)*

PICS are locations on the Earth's surface that are considered temporally, spatially, and spectrally stable over time; they provide a measure of stability or change present in the sensor's radiometric response. They are used for trending of sensor calibration gains and biases over time, sensor cross-calibration, and the development of absolute sensor calibration models.

Cosnefroy et al. [13, 14] selected 20 desert sites in North Africa and Saudi Arabia with estimated spatial uncertainties of 3% or less and temporal uncertainties of approximately 1–2%. Six of these sites (Algeria 3, Algeria 5, Libya 1, Libya 4, and Mauritania 1 and 2) were ultimately designated by the Committee on Earth Observation Satellites (CEOS) as suitable for "multitemporal, multiband, or multiangular calibration of optical satellite sensors" [15]. Helder et al. [16] developed an automated approach to identify temporally and spatially stable locations on the Earth's surface and found six individual sites in the Sahara Desert (including Libya 4) and the Middle East exhibiting spatial and temporal uncertainties on the order of 2% in the visible near-infrared (VNIR) region and 2–3% in the SWIR region.

### *1.2. Cross-Calibration of Optical Satellite Sensors*

As mentioned earlier, in cross-calibration, the response of one sensor is compared to a "reference" sensor based on the analysis of coincident or near-coincident scene pairs of the Earth's surface [8]. Cross-calibration is important for the following reasons. First, as mentioned previously, it may be the only calibration method that can be used for sensors without an onboard calibration source and for target locations where co-incident surface measurements cannot be acquired. Second, it helps to tie sensors with varying spatial, radiometric, and spectral resolutions to a common radiometric scale, which helps mission continuity and data interoperability [17].

### *1.3. Current Limitation of Cross Calibration*

The major limitation of the cross-calibration approach is identifying a sufficient number of useable coincident and/or near-coincident scene pairs. Traditionally, sensor cross-calibration was performed using a few PICS located throughout the Saharan desert with demonstrated temporal stability that also possess corresponding hyperspectral data. Depending on cloud cover at the site during each overpass and the revisit periods of the sensors of interest (e.g., 16 days for the Landsat sensors and 10 days for the Sentinel sensors), several years of coincident acquisitions are needed to construct a useful cross-calibration dataset. Chander et al. [17, 18] performed a cross-calibration of the Landsat 7 Enhanced Thematic Mapper Plus (ETM+) and Terra Moderate Resolution Imaging Spectroradiometer (MODIS) sensors using Libya 4 scene pairs; they found just nine cloud-free coincident scene pairs (within 30 minutes apart) over a five-year interval between 2004 and 2009. Farhad [19] also used Libya 4 for performing cross-calibration between the Landsat 8 Operational Land Imager (OLI) and Sentinel 2A MultiSpectral Instrument (MSI); he found just eight cloud-free coincident scene pairs (again, within 30 minutes apart) in the three-year interval between 2015 and 2018, following the launch of Sentinel-2A. Pinto et al. [20] used only one coincident scene pair from Libya 4 to perform cross-calibration between the OLI and the China-Brazil Earth Resources Satellite (CBERS)-4 Multispectral Camera (MUXCAM) and Wide-Field Imager (WFI) (within 26 minutes apart). Similarly, Li et al. [21] also used a single coincident scene pair from Algeria to perform cross-calibration between the Landsat 8 OLI and Sentinel 2A MSI. While cross-calibration can be performed with a single coincident scene pair, a more reliable calibration is achieved from the use of multiple scene pairs, as the error due to various random effects is reduced [22].

#### 1.4. Current Approach of Cluster-Based Cross Calibration

Recently, Shrestha et al. [23] presented an analysis identifying 19 distinct “clusters” with spectrally similar surface cover widespread across North Africa, as shown in Figure 1. These clusters have the potential to provide nearly daily cloud-free imaging by any sensor. Shrestha et al. [24] derived a representative hyperspectral profile for the previously identified clusters based on analysis of the corresponding Earth Observing(EO) -1 Hyperion image data. These continental scale clusters help to build a useful cross-calibration dataset within a much reduced time span and also help to reduce the uncertainties in the estimated calibration gains and biases.

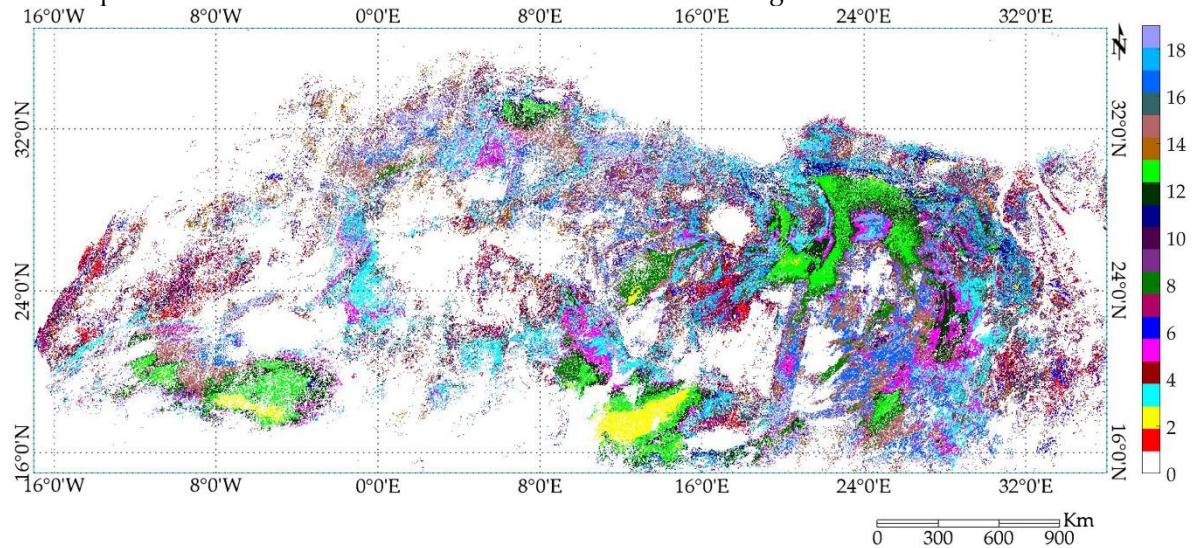


**Figure 1.** Shrestha’s K-means classification of North Africa to 5% spatial uncertainty.

This paper describes a methodology for performing EPICS based cross-calibration. The resulting estimated calibration gains and biases, along with their associated uncertainties, are compared to results obtained from the traditional region of interest (ROI)-based cross-calibration approach. For this analysis, the Landsat 8 OLI and Sentinel-2A MSI were chosen as the cross-calibration sensor pair of interest. The analysis was performed using image data from the standard Centre National d'Etudes Spatiales (CNES) ROI within Libya 4 and image data of Shrestha's Cluster 13 acquired during a one-year interval.

This paper is organized as follows. Section 1 provides a brief overview of the topic. Section 2 discusses the methodology used in the analysis. Section 3 presents the result of the comparison of calibration gain and biased from the two approaches. Section 4 further discusses the result and considers potential directions for future research into this topic. Finally, Section 5 provides a brief summary and conclusions.

## 2. Data and Methods

A comparison of the traditional ROI-based and proposed cluster-based calibration approaches was performed using Landsat 8 OLI and Sentinel 2A MSI image data. Both sensors have been well calibrated, achieving an absolute radiometric accuracy on the order of 3% and a half-pixel or less in geometric registration uncertainty [4, 25]. The key features of the OLI and MSI are summarized in Table 1, with additional descriptions provided below.

### 2.1. Sensor Description

#### 2.1.1. Landsat 8 OLI

Landsat 8 was launched on 11 February 2013 into a sun-synchronous orbit of 705 km altitude, with a mean equatorial crossing at 10:13 AM local solar time [26]. The OLI, one of two sensors onboard Landsat 8, images solar reflectance across nine spectral bands at spatial resolutions of 30 m in all bands except the panchromatic band, which images at a spatial resolution of 15 m. Its push broom design uses a focal plane containing over 69,000 detectors distributed across 14 distinct modules, allowing it to image a 185 km swath width (corresponding to a 15° field of view).

#### 2.1.2. Sentinel 2A MSI

Sentinel 2A was launched on 23 June 2015 into a sun-synchronous orbit at 786 km altitude, with a mean equatorial crossing at 10:30 am local solar time, close to Landsat 8's equatorial crossing time. The MSI is also a push broom sensor, imaging solar reflectance across 13 spectral bands with spatial resolutions ranging between 10 m and 60 m. The MSI focal plane detectors are distributed across 12 distinct modules, allowing it to image a 295 km swath width (corresponding to a 20.6° field of view).

**Table 1.** Salient features of Landsat 8 OLI and Sentinel 2A MSI.

Wavelength Range	Band Number		Center Wavelength (Average Measured) (nm)		Bandwidth (Average Measured) (nm)		IFOV (Nominal)(m)	
	OLI	MSI	OLI	MSI	OLI	MSI	OLI	MSI
Deep Blue	1	1	443	443	16	20	30	60
Blue	2	2	482	492	60	65	30	10
Green	3	3	561	560	57	35	30	10
Red	4	4	655	664	37	30	30	10
Red Edge		5		704		14		20



Red Edge		6		740		14		20
Red Edge		7		783		19		20
NIR	(5)*	8	(865)	835	(28)	105	(30)	10
NIR	5	8a	865	865	28	20	30	20
Water Vapor		9		945		19		60
Cirrus	9	10	1373	1374	20	30	30	60
SWIR 1	6	11	1609	1613	85	90	30	20
SWIR 2	7	12	2201	2200	187	174	30	20
Pan	8		590		172		15	

\*OLI band 5 is most similar spectrally to MSI band 8a; though MSI band 8 is the 10 m band most likely to be used in conjunction with the MSI visible bands, e.g., as in calculating NDVI

## 2.2. Site and Cluster Selection

### 2.2.1. Libya 4 Test Site

The Libya 4 Centre National d'Etudes Spatiales (CNES) ROI was selected for performing a traditional ROI-based cross-calibration, as this site has been extensively used for radiometric intercomparison and vicarious calibration of multiple Earth-observing sensors [15, 27, 28, 29, 30]. It is regarded as one of the best CNES PICS-based on long term trending of the North African and Arabian deserts.

Libya 4 is a high reflectance site in the Saharan desert in North Africa, located at approximately 28.55° N latitude and 23.39° E longitude; it is composed primarily of spatially organized sand dunes. It has demonstrated long-term spatial, spectral, and temporal stability, with a minimum of cloud cover over time [17, 31]. Figure 2 shows the general area and specific ROI within Libya 4 in co-located OLI and MSI images.

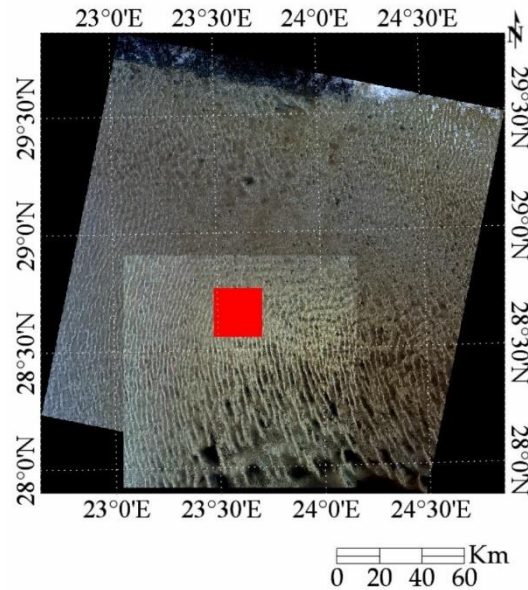


**Figure 2.** Libya 4 image by Landsat 8 OLI (larger rectangle) and Sentinel 2A MSI (smaller rectangle). The red solid rectangle represents Libya 4 Centre National d'Etudes Spatiales (CNES) region of interest (ROI).

### 2.2.2. North African Cluster 13



Shrestha et al. [23] performed an unsupervised classification of North Africa based on a 5% maximum temporal uncertainty and identified 19 clusters of distinct surface cover types. The clusters exhibited reflectances of varying intensities with different degrees of spatial stability. Cluster 13 was selected for this cluster-based calibration analysis due to the following: i) it exhibits a spatial uncertainty less than 5% across all bands; ii) it is widely distributed across North Africa, allowing for its imaging on a nearly daily basis as shown in Figure 3 and resulting in an increased number of coincident OLI/MSI scene pairs; and iii) portions of it lie within the Libya 4 and Egypt 1 sites, which provide greater opportunities for hyperspectral imaging as they are frequently observed by the EO-1 Hyperion; this hyperspectral characterization of the surface is mandatory for the accurate compensation of spectral response differences between the OLI and MSI [32].

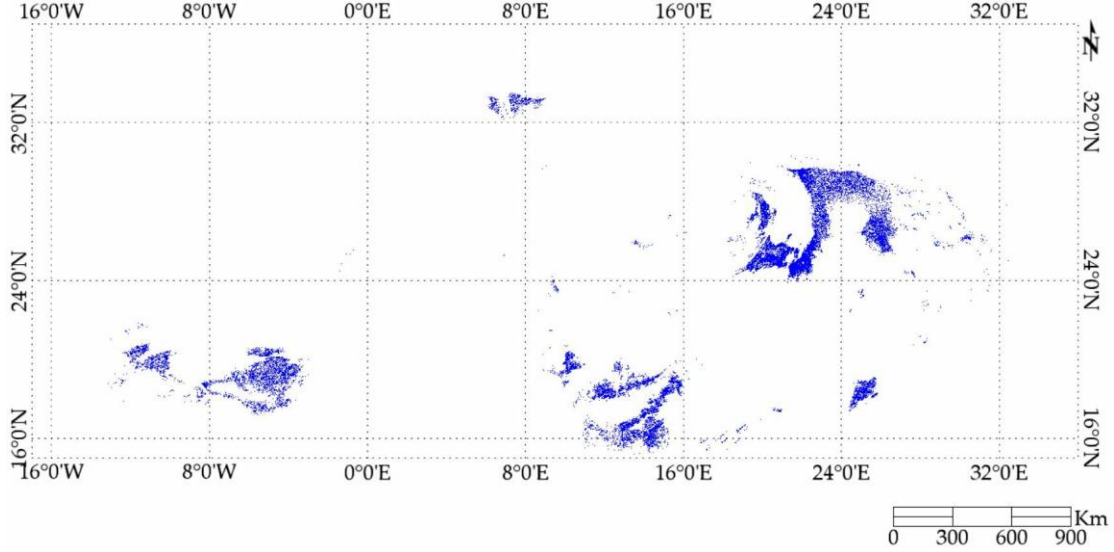


**Figure 3.** Extent Cluster 13 across North Africa. Blue color represents cluster 13 pixels.

### 2.3. Scene Pairs

The Landsat 8 and Sentinel 2A orbits result in different revisit periods (i.e., 16 days for Landsat 8 and 10 days for Sentinel 2A). Consequently, coincident scene pairs between them are acquired every 80 days, with the satellite overpasses typically occurring 16 minutes apart [33]. For this work, the calibration approaches were initially compared using coincident scene pairs; a later comparison included “near coincident” scene pairs (i.e., acquisitions within three days of each other). The three-day window was chosen for the near-coincident pairs under the assumption that no significant changes in surface and atmospheric characteristics had occurred during this period.

After selecting suitable coincident and near coincident scene pairs, Cluster 13 binary masks were generated as described in [34] in order to exclude non Cluster 13 pixels from consideration in the analysis. The remaining pixels were the processed following the procedure described in the following sections.

### 2.4. Conversion to TOA Reflectance

The OLI image data were converted to TOA reflectance as follows [35]:

$$\rho_{OLI,\lambda} = \frac{M_Q \times Q_{cal} + A_Q}{\cos(\theta_{SZA})}, \quad (1)$$

where  $\rho_{OLI,\lambda}$  is the solar zenith angle corrected Landsat 8 OLI TOA reflectance;  $M_Q$  and  $A_Q$  are, respectively, the band-specific multiplicative and additive scaling factors obtained from the

associated product metadata;  $Q_{cal}$  is the quantized and calibrated standard product pixel value (DN); and  $\theta_{SZA}$  is the per-pixel solar zenith angle as extracted from the associated product solar angle band.

The MSI image data were converted to TOA reflectance according to [36] :

$$\rho_{MSI} = \frac{Q_{cal, MSI}}{K}, \quad (2)$$

where  $\rho_{MSI}$  is the MSI TOA reflectance,  $Q_{cal, MSI}$  is the quantized calibrated standard product pixel values (DN), and  $K$  is a reflectance scaling factor obtained from the associated product metadata. In this case, the MSI calibrated pixel values account for solar angle effects.

In order to perform a direct reflectance comparison, between the sensors, the spectral difference between them must be addressed. The process used to address this issue is described next.

#### 2.4.1. Spectral Band Adjustment Factor (SBAF)

Two satellite sensors used in a cross-calibration can be designed for very different applications. Based on the application and the existing technology at the time of their development, the sensors will very likely exhibit significant differences in spectral response when observing the same source [32]. Teillet et al. [10] showed that spectral band difference effects are more dependent on surface reflectance characteristics rather than atmospheric conditions or illumination geometry. Such spectral differences can be compensated for if prior knowledge is available concerning the ground target's spectral signature during the satellite overpass time. Thus, the intrinsic band offset between sensors can be compensated by a target-specific spectral band adjustment factor (SBAF) which takes the target's spectral profile and the sensor relative spectral responses (RSRs) into account [17, 31]. For purposes of this analysis, the OLI was chosen as the calibrated "reference" sensor for SBAF determination. Consequently, the SBAF to be applied to the MSI data to "match" the OLI response was calculated as follows:

$$SBAF = \frac{\rho_{\lambda, OLI}}{\rho_{\lambda, MSI}} = \frac{\frac{\int \rho_{\lambda} RSR_{\lambda}(OLI) d\lambda}{\int RSR_{\lambda}(OLI) d\lambda}}{\frac{\int \rho_{\lambda} RSR_{\lambda}(MSI) d\lambda}{\int RSR_{\lambda}(MSI) d\lambda}} \quad (3)$$

where  $\rho_{\lambda, OLI}$  and  $\rho_{\lambda, MSI}$  are, respectively, the simulated TOA reflectances for the OLI and MSI;  $\rho_{\lambda}$  is a representative hyperspectral profile of the surface; and  $RSR_{\lambda(sensor)}$  is the relative spectral response of the corresponding sensor.

Using the derived SBAF, the TOA reflectance of Sentinel 2A MSI is converted to corresponding Landsat 8 OLI TOA reflectance using equation 4.

$$\rho'_{MSI} = \rho_{MSI} \times SBAF, \quad (4)$$

where  $\rho'_{MSI}$  is the Sentinel 2A MSI TOA reflectance equivalent to Landsat 8 OLI TOA reflectance.

In order to perform a cross-calibration and cross-comparison between optical satellite sensors, a target-specific SBAF can be derived using an EO-1 Hyperion hyperspectral data or a web-based tool for calculating SBAF from Scanning Imaging Absorption Spectrometer for Atmospheric Chartography (SCHIAMACHY) hyperspectral data. The SCHIAMACHY-based spectral band adjustment factors are computed from algorithms and online tools developed at National Aeronautics and Space Administration Langley Research Center (NASA-LaRC) with SCHIAMACHY V7.01 data obtained from the European Space Agency Envisat program [37, 38].

#### 2.4.2. Bidirectional Reflection Distribution Function (BRDF)

Bidirectional reflection distribution function (BRDF) provides the reflectance of the surface as a function of a solar and viewing geometry. Much of the Earth's surface is non-Lambertian in nature; the reflectance of the surface varies with solar illumination and sensor viewing geometry. BRDF effects increase as the sensor field of view increases; consequently, data from sensors such as the Advanced Very High Resolution Radiometer (AVHRR) and MODIS, with wider fields of view, may require significant BRDF correction [39]. For nadir looking sensors such as the OLI and MSI, the fields of view are relatively narrow (i.e., approximately  $\pm 7.5^\circ$  for the OLI and  $\pm 10.3^\circ$  for the MSI); hence, BRDF effects should be significantly less [40]. Unfortunately, due to differences in viewing and solar illumination geometry between sensors, imaging the same ground target will produce BRDF effects in the image data significant enough to require some level of correction.

Various empirical and semi-empirical BRDF models have been used for addressing BRDF effects in sensor calibration. Liu et al. [41] and Lacherade et al. [30] used Roujean's semi-empirical BRDF model [42] to remove the angular effect of solar and viewing geometry when performing the cross-calibration of MODIS and Multi-channel Visible Infrared Scanning radiometers (MVIS). Wu et al. [43] used the Ross-Li semi-empirical BRDF model to remove the angular effect while determining the calibration stability of MODIS using the Libyan Desert and Dome C Antarctic surfaces. Mishra et al. [27] and Helder et al. [28] developed the absolute calibration model using Libya 4 using empirically derived linear and quadratic functions of solar zenith angle to remove the angular effect.

The amount of BRDF correction can be improved by including all four angles, i.e., solar and view zenith and azimuth angles. The development of a full four angle model begins with the conversion of the view and solar angles from a spherical coordinate basis to a linear Cartesian basis in order to obtain TOA reflectance of the surface as a continuous function of independent variables [19]:

$$x_1 = \sin(\text{SZA}) * \cos(\text{SAA}) \quad (5)$$

$$y_1 = \sin(\text{SZA}) * \sin(\text{SAA}) \quad (6)$$

$$x_2 = \sin(\text{VZA}) * \cos(\text{VAA}) \quad (7)$$

$$y_2 = \sin(\text{VZA}) * \sin(\text{VAA}) \quad (8)$$

where SZA and SAA are the solar zenith and azimuth angles in radians, respectively, and VZA and VAA are the sensor viewing zenith and azimuth angles, respectively (also in radians). Multiple linear least-squares regression is used to derive the models, which account for higher-order and interaction effects between sets of angles.

$$\rho_{\text{model}} = \beta_0 + \beta_1 x_1 + \beta_2 y_1 + \beta_3 x_2 + \beta_4 y_2 + \beta_5 x_1^2 + \beta_6 y_1^2 + \beta_7 x_2^2 + \beta_8 y_2^2 + \beta_9 x_1 y_1 + \beta_{10} x_1 x_2 + \beta_{11} x_1 y_2 + \beta_{12} y_1 x_2 + \beta_{13} y_1 y_2 + \beta_{14} x_2 y_2, \quad (9)$$

Once the models have been generated, the mean of solar and sensor view zenith and azimuth angles were chosen as a reference in order to scale the TOA reflectance to a common level. The resulting reference angles were converted to a Cartesian basis, as in (4-8), and then used to generate a reference TOA reflectance:

$$\begin{aligned} \rho_{\text{Ref}} = & \beta_0 + \beta_1 x_{1\_Ref} + \beta_2 y_{1\_Ref} + \beta_3 x_{2\_Ref} + \beta_4 y_{2\_Ref} + \beta_5 x_{1\_Ref}^2 + \beta_6 y_{1\_Ref}^2 + \beta_7 x_{2\_Ref}^2 + \\ & \beta_8 y_{2\_Ref}^2 + \beta_9 x_{1\_Ref} y_{1\_Ref} + \beta_{10} x_{1\_Ref} x_{2\_Ref} + \beta_{11} x_{1\_Ref} y_{2\_Ref} + \beta_{12} y_{1\_Ref} x_{2\_Ref} + \\ & \beta_{13} y_{1\_Ref} y_{2\_Ref} + \beta_{14} x_{2\_Ref} y_{2\_Ref}, \end{aligned} \quad (10)$$

The reference TOA reflectance was then scaled by the ratio of the observed and model-predicted TOA reflectances to obtain the final BRDF-corrected TOA reflectance:

$$Q_{\text{site}} = \frac{Q_{\text{obs}}}{Q_{\text{model}}} * Q_{\text{Ref}} \quad (11)$$

### 3. Results

This section compares the results of ROI-based and cluster-based cross-calibration between the OLI and the Sentinel 2A MSI. The comparison was performed on coincident and near-coincident scene pairs acquired throughout 2017, and, as both of the sensors were well calibrated, this work assumed that the bias was corrected properly such that the calibration gain could be determined from only bright targets.

#### 3.1. Coincident and Near-Coincident Acquisitions

Due to the orbital patterns of Landsat 8 and Sentinel 2A, only 5.6 percent of the globe offers coincident acquisitions between the OLI and MSI every 80 days [33]. Libya 4 happens to be in the list of specific locations on the Earth's surface providing such acquisitions. Throughout 2017, four coincident scene pairs were acquired over Libya 4 CNES ROI. Table 2 provides the coincident dates along with the viewing angles for each sensor.

**Table 2.** Coincident dates between Landsat 8 OLI and Sentinel 2A MSI for Libya 4 CNES ROI. Bold are cloud-free acquisitions.

Coincident dates (yyyy.mm.dd)	Acquisition time (OLI)	Acquisition time (MSI)	OLI view angles (Zenith/Azimuth) (Degree)	MSI view angles (Zenith/Azimuth) (Degree)
2017.02.22	08:55	09:11	4.75/9.28	3.96/101.64
<b>2017.05.13</b>	08:54	09:08	4.75/9.50	3.84/103.44
<b>2017.08.01</b>	08:55	09:03	4.76/9.39	3.88/102.92
<b>2017.10.20</b>	08:55	09:05	4.75/9.37	3.87/103.16

As Cluster 13 extends across North Africa (Figure 3), it increases the opportunity to collect coincident acquisitions between Landsat 8 and Sentinel 2A. Figure 4 shows the intersections between the Cluster 13 boundaries (red boxes) and the Landsat 8 and Sentinel 2A footprints (the white boxes and blue boxes, respectively). 28 locations intersect Cluster 13 and each sensor's footprints. Among these paths and rows, only six paths and rows have cloud-free acquisitions coincident acquisitions, as shown in Table 3.

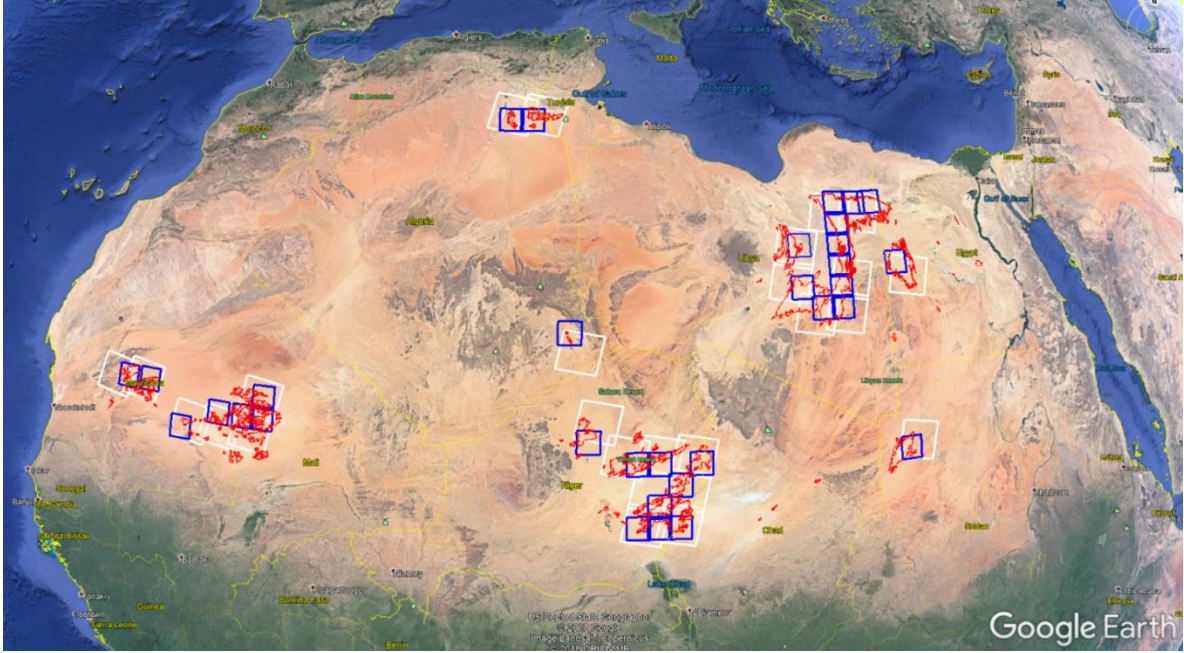


**Figure 4.** The intersection of Cluster 13, Landsat 8 OLI, and Sentinel 2A MSI. Red boundaries represent the Cluster 13 boundaries across North Africa. White and blue rectangular boxes represent Landsat 8 OLI and Sentinel 2A MSI footprints, respectively.

**Table 3.** Cloud-free Coincident acquisitions between Landsat 8 OLI and Sentinel 2A for Cluster 13.

Path/Row	Coincident dates (yyyy.mm.dd)	Acquisition time (OLI)	Acquisition time (MSI)	OLI view angles (Zenith/Azimuth) (Degree)	MSI view angles (Zenith/Azimuth) (Degree)
181/40	2017.05.13	08:54	09:08	4.75/9.50	3.80/103.44
	2017.08.01	08:55	09:03	4.76/9.39	3.80/102.92
	2017.10.20	08:55	09:05	4.75/9.37	3.80/103.44
181/42	2017.08.01	08:55	09:00	3.89/64.79	7.00/101.07
	2017.10.20	08:56	09:00	3.82/62.15	6.99/101.03
181/41	2017.05.13	08:54	09:00	4.27/14.26	8.51/103.59
	2017.08.01	08:55	09:00	4.26/13.42	8.54/103.69
	2017.10.20	08:55	09:00	4.21/11.64	8.53/103.64
185/47	2017.10.16	09:22	09:20	4.22/-1.25	8.72/102.78
186/47	2017.06.01	09:28	09:30	4.71/11.14	3.94/97.95
192/37	2017.07.13	10:01	10:10	4.54/13.14	2.73/134.34

Similarly, Libya 4 CNES ROI has eight near coincident acquisitions between Landsat 8 OLI and Sentinel 2A, as listed in Table 4. Acquisitions that are three days apart are considered as near coincident, since the surface properties and atmosphere do not change significantly within this short temporal window; Barsi et al. [44] have shown that Libya 4 CNES ROI is very stable over a six day time period for cloud-free acquisitions, which they consider suitable for cross-calibration purposes.

**Table 4.** Near-coincident data between Landsat 8 OLI and Sentinel 2A MSI for Libya 4 CNES ROI.

Coincident dates (yyyy.mm.dd)	Coincident dates MSI (yyyy.mm.dd)	Acquisition time (OLI)	Acquisition time (MSI)	OLI view angles (Zenith/Azimuth)	MSI view angles (Zenith/Azimuth)
2017.01.05	2017.01.03	08:55	09:03	4.76/9.20	3.95/101.63
2017.03.26	2017.03.24	08:54	08:56	4.76/9.30	3.96/101.64
2017.05.13	2017.05.13	08:54	09:08	4.75/9.50	3.84/103.44
2017.06.14	2017.06.12	08:54	08:56	4.76/9.35	3.92/102.05
2017.08.01	2017.08.01	08:55	09:03	4.75/9.39	3.88/102.91
2017.09.18	2017.09.20	08:55	08:56	4.75/9.48	3.85/103.44
2017.10.20	2017.10.20	08:55	09:05	4.75/9.37	3.87/103.16
2017.11.21	2017.11.22	08:55	09:13	4.75/9.30	3.92/102.12

Similarly, Cluster 13 offers 108 cloud-free scene pairs from 20 Worldwide Reference System (WRS)-2 paths and rows. The significant increase in near-coincident scene pairs usable for cluster-based cross-calibration is possible due to its widespread spatial distribution across North Africa.

After getting the cloud-free coincident and near-coincident scene pairs, OLI and MSI TOA reflectances were calculated from pixels within the CNES ROI for the traditional PICS-based calibration approach. For the cluster-based approach, the reflectances were calculated from the pixels within a region common to Cluster 13 and each sensor's footprint, as shown in Figure 5.

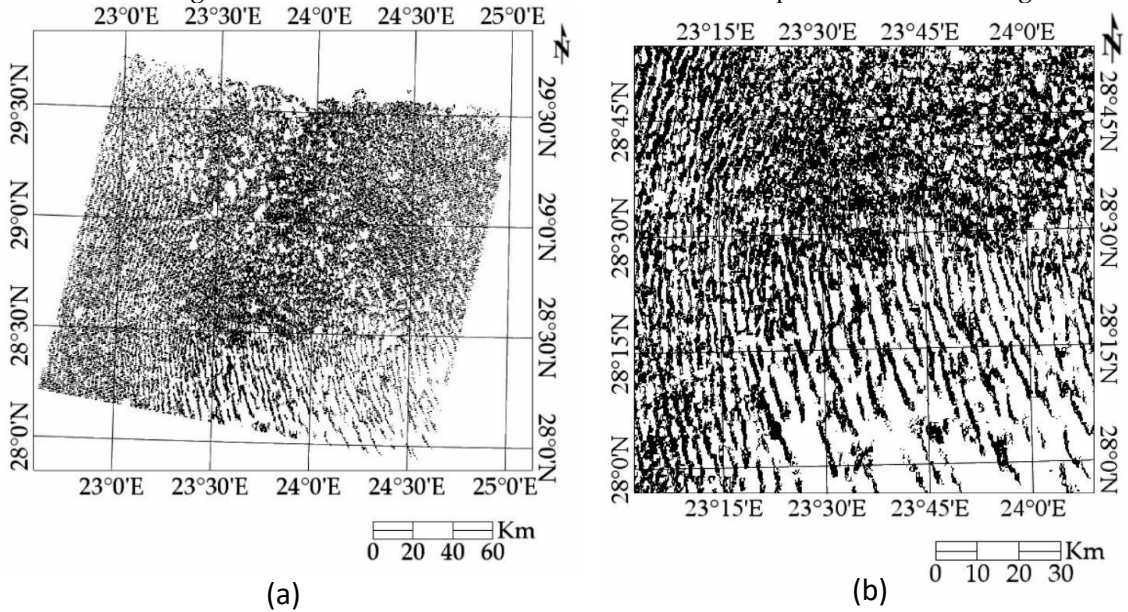


**Figure 5.** Intersection of Cluster 13 and Libya 4 (a) Landsat 8 OLI (b) Sentinel 2A MSI. Black pixels represent the cloud-free Cluster 13 pixels of Libya 4.

Once the TOA reflectances for each sensor were determined, the SBAF was applied to compensate for spectral response differences between the sensors. The next section shows the resulting SBAF distributions for the MSI.

### 3.2. SBAF for Libya 4 CNES ROI and Cluster 13

For this work, the OLI was considered as the reference to which the MSI spectral response is normalized. Libya 4 has sets of SBAFs derived from 59 hyperspectral data profiles, whereas Cluster 13 has sets of SBAFs estimated from 188 hyperspectral profiles [24]. Figure 6 shows the resulting MSI SBAF (2 sigma) for all common bands.



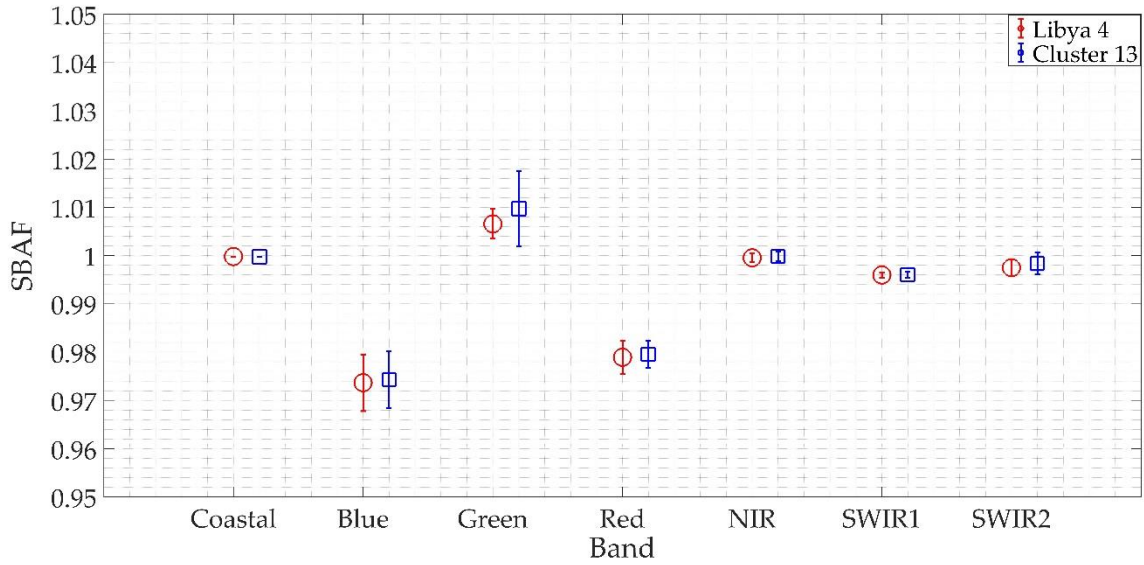


**Figure 6.** Spectral band adjustment factor (SBAF) for Sentinel 2A MSI for Libya 4 CNES ROI and Cluster 13 (Uncertainty bars,  $k = 2$ ).

Since Libya 4 is included within Cluster 13 [23, 24], the SBAFs for Libya 4 CNES ROI and Cluster 13 were similar to each other. The RSR's of coastal, NIR, SWIR1, and SWIR2 bands of these two sensors were very similar to each other, as shown in Appendix A, which resulted in an SBAF very close to one. In contrast, the SBAF for the blue and red bands differed from one because their RSR's were shifted relative to each other. In addition, the MSI SBAF mean values for both Libya 4 CNES ROI and Cluster 13 were equal for all bands except the green band, and the observed 0.35% difference was due to more discrepancy between the hyperspectral profiles of Libya 4 CNES ROI and Cluster 13 from 500 to 560 nm; some of it is presumably due to the difference in width of the RSR's of the two sensors [44]. Such a relative shift and width mismatch of the RSR between the two sensors also contributed to the higher SBAF uncertainty of the blue, green, and red bands, as shown in Figure 6. The SBAF uncertainty of the blue band was approximately 0.25% and similar for both CNES ROI and Cluster 13, whereas the SBAF uncertainty of the green band using Cluster 13 was larger by 0.24% than using the CNES ROI.

The mean SBAF difference was as large as 3.5% and 2.5% for the blue and red bands, respectively, because the OLI and MSI RSR's in these bands were shifted relative to each other with respect to hyperspectral signature of the target, as shown in Appendix A.

### 3.3. Comparison of TOA Reflectance of Landsat 8 and Sentinel 2A

After performing SBAF and BRDF correction to the MSI TOA reflectance, OLI and MSI TOA reflectances were compared with each other. The comparison of Landsat 8 OLI and Sentinel 2A MSI TOA reflectance (2 sigma) using Libya 4 CNES ROI coincident scene pairs is presented in Figures 7 (traditional ROI-based approach) and 8 (cluster-based approach). The estimated Libya 4 CNES ROI TOA reflectances from both ROI and cluster-based methods were consistent with each other. As expected, the VNIR and SWIR1 band TOA reflectances from both sensors were in better agreement than in the SWIR 2 band, suggesting there are residual spectral differences were not accounted for with the SWIR2 SBAF correction.

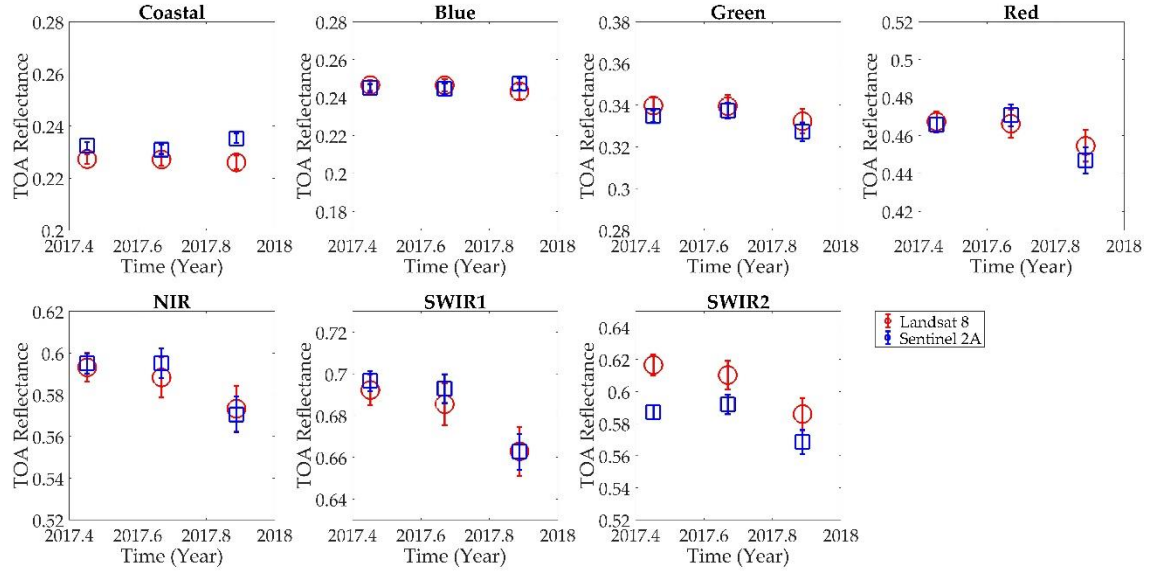


**Figure 7.** Comparison of Landsat OLI and Sentinel 2A MSI TOA reflectance (Uncertainty bars are  $k=2$ ) using Libya 4 CNES ROI coincident scene pairs.

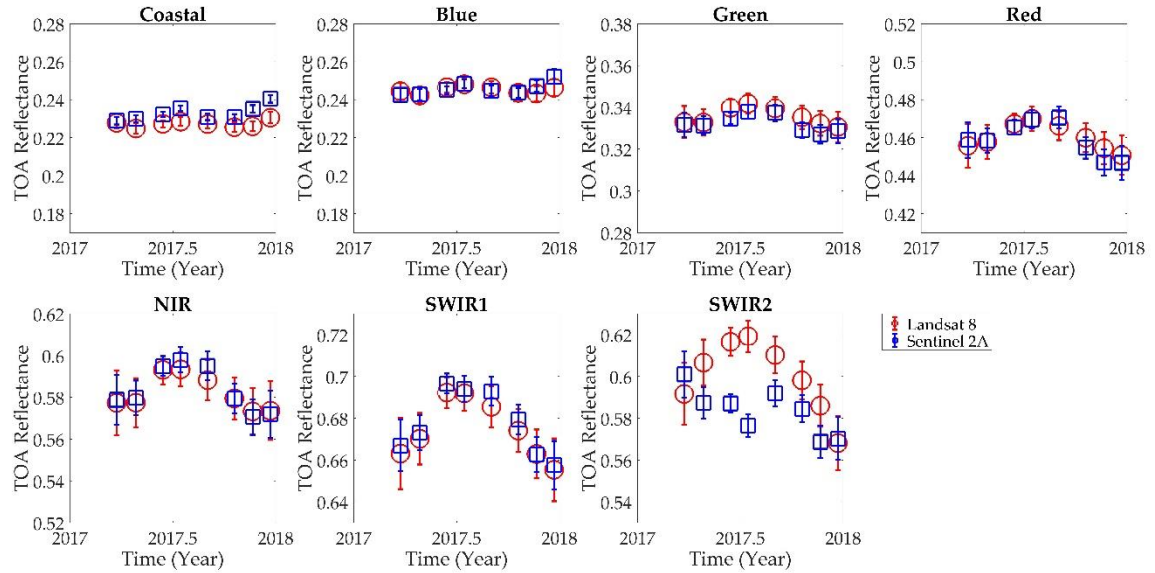


**Figure 8.** Comparison of Landsat OLI and Sentinel 2A MSI TOA reflectance (Uncertainty bars are  $k=2$ ) using Libya 4 CNES ROI near coincident scene pairs.

The comparison of OLI and MSI TOA reflectance using near-coincident scene pairs are presented in Figures 9 (traditional ROI-based approach) and 10 (cluster-based approach). As with the coincident scene pairs, the reflectances were consistent for both approaches and lied with each other's uncertainty for all bands except the SWIR 2 band. In Figure 10, the observed TOA reflectance uncertainty, such as approximately 5% for the coastal band and approximately 3% for the NIR band, was expected and equivalent to the spatial uncertainty (ratio of spatial standard derivation to spatial mean) of Cluster 13, as it was the main source of uncertainty. As in the



previous comparison using coincident scene pairs, the SWIR 2 band had more discrepancy between the TOA reflectance of OLI and MSI than the rest of the bands.

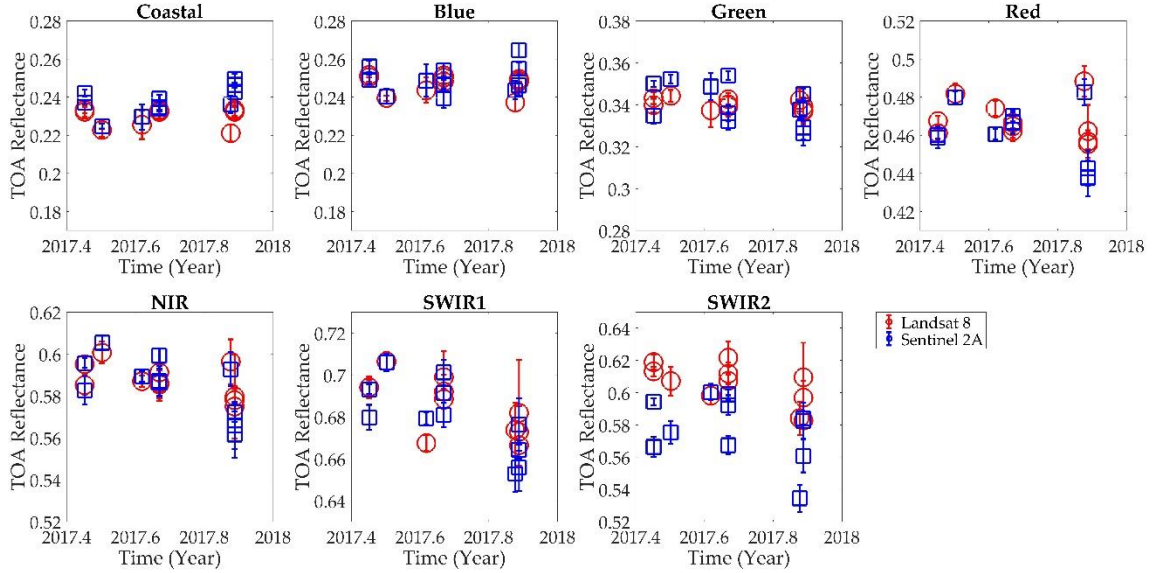


**Figure 9.** Comparison of Landsat OLI and Sentinel 2A MSI TOA reflectance (Uncertainty bars are  $k=2$ ) using Cluster 13 coincident scene pairs.

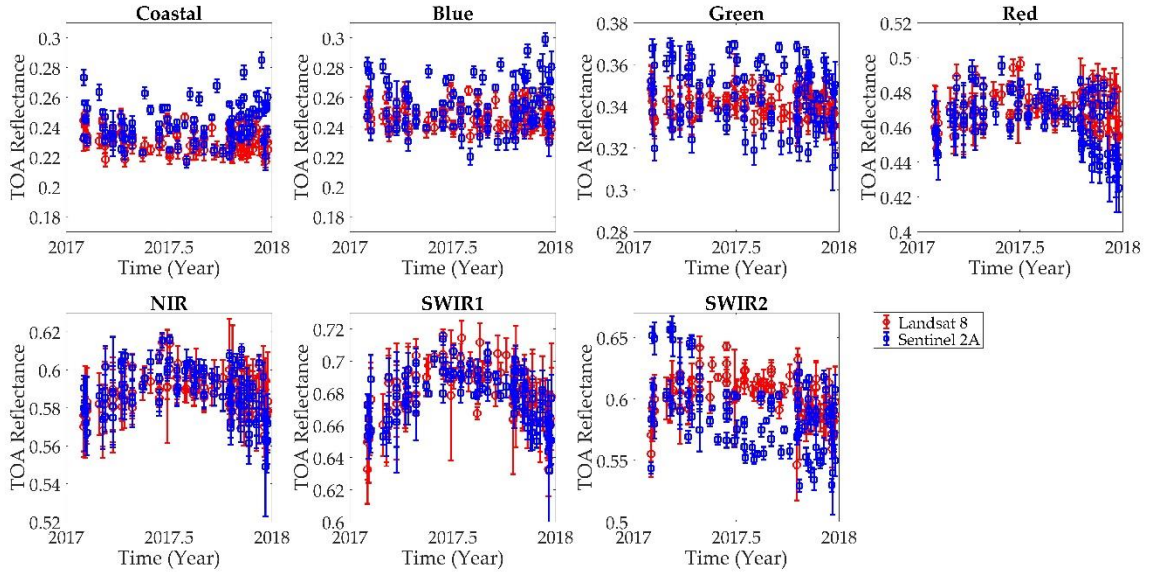


**Figure 10.** Comparison of Landsat OLI and Sentinel 2A MSI TOA reflectance using Cluster 13 near coincident scene pairs.

### 3.4. Comparison of Cross-Calibration Gain ratios from ROI-Based and Cluster-Based Approach

After correcting the MSI TOA reflectances, the cross-calibration gain ratio was calculated as the ratio of OLI TOA reflectance to MSI TOA reflectance, as shown in Figures 11 (for 3 coincident scene pairs from Libya 4 CNES ROI and 11 coincident scene pairs from the 6 WRS-2 paths/rows within Cluster 13) and 12 (for 8 near-coincident scene pairs from Libya 4 CNES ROI and 108 near-

coincident scene pairs from the 20 WRS-2 paths/rows within Cluster 13). In these figures, the red symbols represent the cross-calibration gain ratios derived from the traditional ROI-based cross-calibration method, whereas the blue symbols represent the cross-calibration gain ratios derived from the cluster-based approach.

As Cluster 13 also includes Libya 4 CNES ROI, the cluster-based and ROI-based cross-calibration gain ratios were similar to each other. The cross-calibration gain ratios derived from the traditional ROI-based approach using coincident scene pairs tended to exhibit less scatter than the corresponding gain ratios derived from the cluster-based approach, as the Libya 4 CNES ROI had less uncertainty than Cluster 13. Figures 11 and 12 show that, among all the bands, the cross-calibration gain ratios of the NIR band were more consistent, as both of the sensors had a very good agreement on their TOA reflectance; there was only 1.56% variability using cluster-based near coincident scene pair. In contrast, the cross-calibration gain ratios of the SWIR 2 band had the maximum variability of approximately 5% (using cluster-based near coincident scene pairs) as the TOA reflectance from OLI and MSI had a broader range in this band, as presented in Figures 8 and 10.

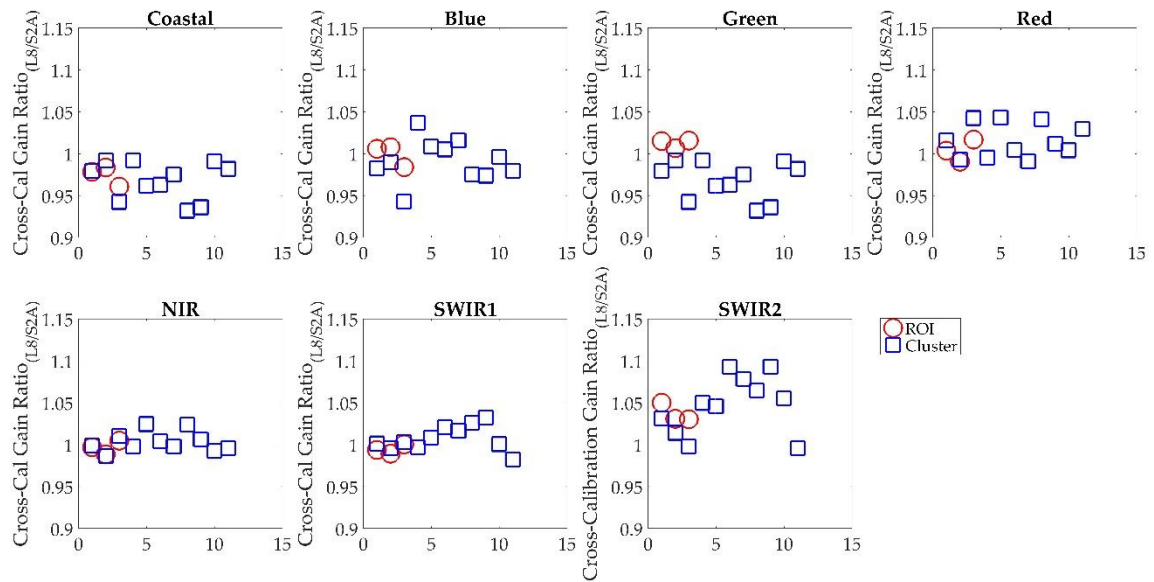


**Figure 11.** Comparison of Landsat OLI and Sentinel 2A MSI TOA cross-calibration gain ratios using Libya 4 CNES ROI coincident scene pairs.

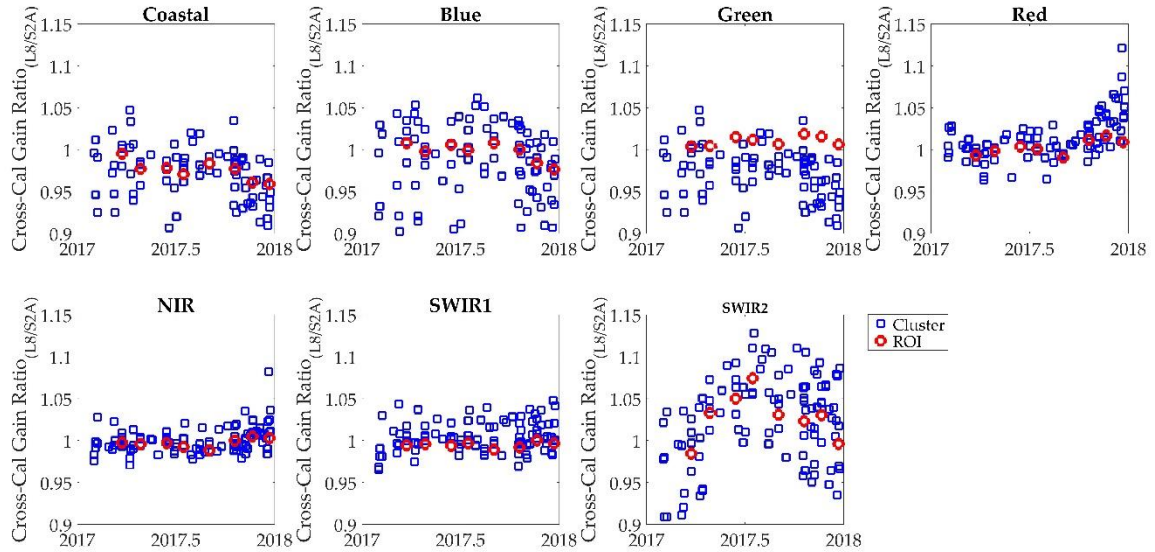


**Figure 12.** Comparison of Landsat OLI and Sentinel 2A MSI TOA cross-calibration gain ratios using Cluster 13 near coincident scene pairs.

Figures 13 and 14, respectively, represent the mean cross-calibration gain ratio and associated standard deviation derived for both cross-calibration approaches. The mean cross-calibration gain ratio was calculated by taking an average of temporal cross-calibration gain ratios, as shown in Figures 11 and 12, and plotted with its corresponding 2-sigma standard deviation in Figures 13 and 14. Ideally, after application of the SBAF and BRDF corrections, the cross-calibration gain ratios for two well-calibrated sensors should have been equal to 1. The cross-calibration gain ratios derived from both approaches deviated from 1 due to the sensor absolute radiometric uncertainty, uncertainties associated with the SBAF and BRDF corrections themselves, and uncertainties due to the atmosphere. In general, both approaches tend to produce consistent cross-calibration gain ratio estimates. The cross-calibration gain ratio derived from the cluster-based approach had consistently higher uncertainty across all the bands. Though the green band had a lower spatial uncertainty (3%) than the coastal and blue bands (5%), the cross-calibration gain ratio had a similar uncertainty. In general, the error bars of the cross-calibration gain ratio derived from both methods overlapped, implying that the cluster-based cross-calibration provided consistent results with the ROI-based cross-calibration approach.

Figure 14 shows that the cross-calibration gain ratios derived from the cluster-based approach were similar to the cross-calibration gain ratios derived from an ROI-based approach but are not consistent, as they have higher uncertainty across all the bands. The cross-calibration gain ratio for shorter wavelengths had higher uncertainty than the longer wavelength as the spatial uncertainty of Cluster 13 was higher in the shorter wavelengths than the rest of the bands. The cross-calibration gain ratios of the blue and NIR bands had the highest and lowest uncertainty of approximately 11% and 3%, respectively. For the SWIR 2 band, both sensors appeared to exhibit inherently more variation in TOA reflectance than in the other bands, increasing the uncertainty in cross-calibration gain ratio estimated with both approaches. Though the larger number of scene pairs available with the cluster-based approach tended to average out the random BRDF and atmospheric effects, resulting in a more accurate cross-calibration gain estimate, the spatial uncertainty of Cluster 13 drove up the cross-calibration gain uncertainty.

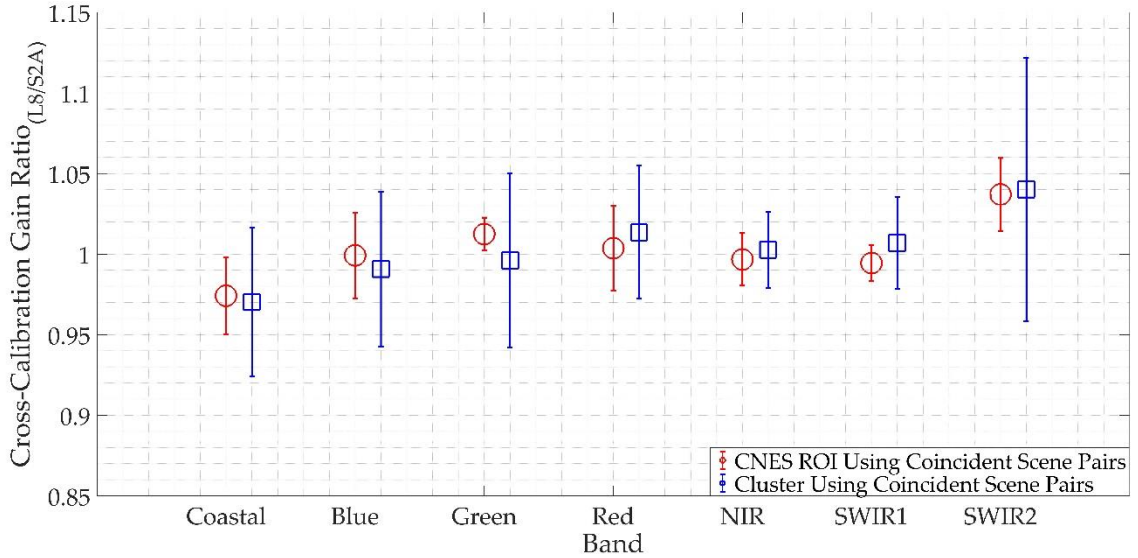


**Figure 13.** Cross-calibration gain comparison of Landsat 8 OLI and Sentinel 2A MSI using a traditional ROI-based approach and a cluster-based approach from Libya 4 CNES ROI coincident scene pairs (Uncertainty bars,  $k = 2$ ).

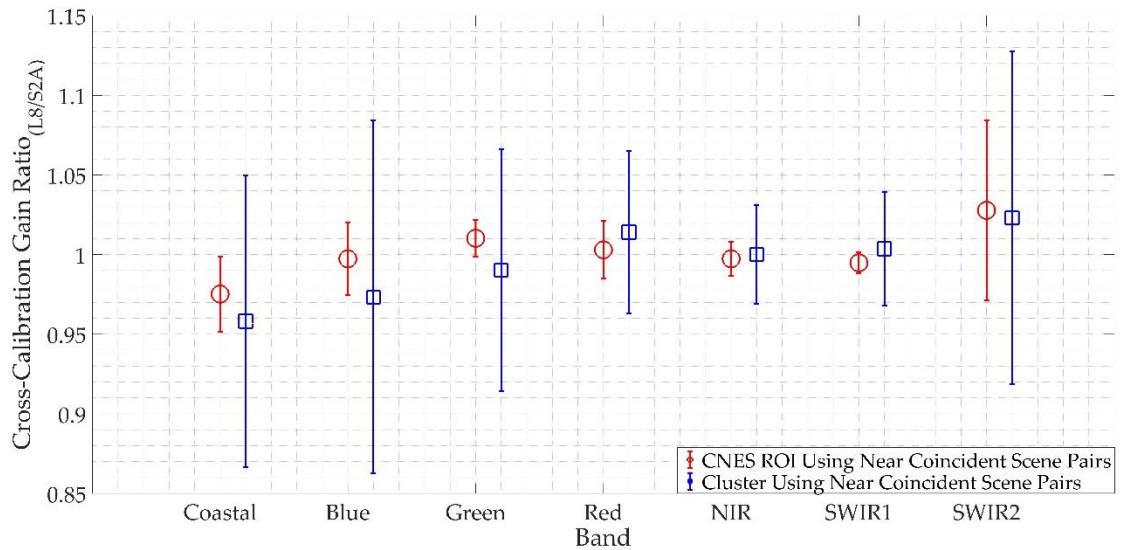


**Figure 14.** Cross-calibration gain comparison of Landsat 8 OLI and Sentinel 2A MSI using a traditional ROI-based approach and a cluster-based approach using Cluster 13 near coincident scene pairs (Uncertainty bars,  $k = 2$ ).

#### 4. Discussion

PICS have been extensively used by multiple researchers for sensor inter-comparison and cross-calibration [11, 12, 17, 18]. In cross-calibration, the response of one sensor is compared with the response of another well-calibrated sensor using coincident and/or near-coincident scene pairs of a selected area on the Earth's surface. Traditionally, a limited number of spatially and temporally stable regions in North Africa with corresponding hyperspectral information were used for sensor cross-calibration. Given limitations in imaging frequently due to sensor revisit time and the

occurrence of adverse cloud cover potentially obscuring the site, a much longer time period is required to acquire suitable coincident and/or near-coincident cross-calibration scene pairs. This is the major limitation of the existing ROI-based cross-calibration method.

Recently, Shrestha et al. [23, 24] found 19 distinct “clusters” of spectrally similar surface cover throughout North Africa, which can be considered temporally and spatially stable. They also estimated a representative hyperspectral profile of these clusters for use as EPICS targets suitable for sensor cross-calibration purposes. These clusters are distributed across the continent such that they can be imaged on a daily or nearly a daily basis by any satellite sensor. Since these EPICS are more frequently imaged than an individual PICS, the number of candidate cross-calibration opportunities using coincident and near coincident scene pairs increases significantly.

As clusters provide a larger number of coincident scene pairs, the current work focused on developing a technique to use EPICS for cross-calibration purposes. To analyze this technique, two individually well-calibrated sensors, the Landsat 8 OLI and Sentinel 2A MSI, were chosen, and a single year time frame was selected for the test purpose. Libya 4 CNES ROI was selected as a representative “traditional” PICS, as its temporal and spatial stability has been well established in earlier work. Shrestha’s Cluster 13 was chosen, as it is widely distributed across North Africa and possesses lower spatial uncertainty across all bands. Cluster 13 also includes Libya 4 CNES ROI, thus facilitating comparison between the traditional ROI-based approach and the proposed cluster-based cross-calibration approach.

For this work, the near-coincident scene pairs were acquired approximately three days apart. For such a short time interval, it can be assumed that surface response does not appreciably change. Furthermore, Barsi et al. [44] showed that Libya 4 CNES ROI was temporally and spatially stable over a six day period, assuming cloud-free conditions. Consequently, image pairs did not necessarily need to be acquired on the same date to be considered for cross-calibration purposes. Even using a spatial extent of Cluster 13, there were only 11 coincident scene pairs due to the sensor revisit time and imaging schedules.

OLI and MSI TOA reflectance from Libya 4 CNES ROI exhibits some random variations about a mean value but are very consistent, using both coincident and near coincident scene pairs as shown in Figures 7 and 8. The TOA reflectance from these two sensors lies within each other’s uncertainty range for all bands except the SWIR 2 band. Within the study period, it had a maximum difference between the TOA reflectance of CNES ROI of an approximately 0.04 reflectance unit for both using coincident and near-coincident scene pairs. One of the reasons for these observed differences was due to spectral difference not accounted by SBAF corrections, and another reason was the change in the site or a sensor with respect to time. Barsi et al. [44] showed that both OLI and MSI have positive slopes of TOA reflectance over time using data from June 2015 to May 2017, which might have contributed to the observed TOA reflectance in Figures 7 and 8.

Figures 9 and 10 show the comparison of OLI and MSI TOA reflectance of Cluster 13 using coincident and near-coincident scene pairs. The TOA reflectance of both the sensors had less variation using coincident scene pairs than using near-coincident scene pairs because only six locations of Cluster 13 offered coincident scene pairs between the two sensors, whereas 20 locations offered the near-coincident scene pairs, which increase the likelihood of higher spatial uncertainty. For example, the TOA reflectance of the coastal band had a difference of 0.02 reflectance using only coincident scene pairs, whereas it had a difference of 0.04 reflectance while using near-coincident scene pairs. The change of 0.04 absolute reflectance was approximately 16% (3 sigma) in a relative scale. The spatial uncertainty of Cluster 13 was approximately 5% (1 sigma), which would be equivalent to the change in variation that is being observed. As such, the observed amount of variation in TOA reflectance using the near-coincident scene pairs is expected in a cluster-based approach.

As this is an initial attempt to use EPICS for cross-calibration, the cross-calibration gain ratio was calculated simply by taking the ratio of TOA reflectance of two sensors for each band. The cross-calibration gain ratio derived using both coincident and near-coincident scene pairs had variation as expected due to a Cluster 13 spatial uncertainty of approximately 5% in the coastal and blue bands and 3% for the rest of the bands, as shown in Figures 11 and 12. Using coincident scene pairs, the uncertainty of the cluster-based cross-calibration gain ratio was within 3 % for all the bands except for the SWIR 2 band, as shown in Figure 13. When using near coincident scene pairs, the uncertainty was within 5% for all bands except the Blue and SWIR2 bands, as shown in Figure 14. Note that Cluster 13 has 11 coincident scene pairs obtained from 6 WRS-2 paths/rows and 108 near coincident scene pairs are obtained from 20 paths/rows. The increased uncertainty in calibration gain derived using near coincident scene pair was more due to spatial uncertainty of Cluster 13 than the three-day window used to consider the acquisition as near coincident scene pairs.

As the purpose of this work was to demonstrate the technique of using cluster-based cross-calibration, a comparison was made between the cross-calibration gain ratio using the Libya 4 CNES ROI, Cluster 13, and the cross-calibration gain using lifetime data of the OLI and Sentinel 2A MSI at different locations [19]. The cross-calibration gain ratio obtained from this work was compared with the calibration gains obtained by Farhad [19]. Figure 15 shows the estimated cross-calibration gain ratio between the OLI and Sentinel-2A MSI for each band. The red symbols represent the cross-calibration gain ratios obtained by using the eight near coincident scene pairs of the Libya 4 CNES ROI. The brown symbols represent the cross-calibration gain ratio obtained by using the 11 coincident scene pair of Cluster 13, and the blue symbols represent the cross-calibration gain ratio obtained by using the 108 near coincident scene pairs of Cluster 13. The green symbols represent the average lifetime ratios for the common spectral bands of OLI and MSI using Libya 4 CNES ROI; six acquisitions collected on the same day and 28 acquisitions collected up to six days apart [44]. Finally, the black symbols represent the estimated calibration gains using the traditional ROI-based method using PICS with varying intensity levels [19]. In general, the cross-calibration gain ratios obtained in this work using Cluster 13 are consistent with the calibration gains obtained by Farhad. The NIR band had the best agreement between the mean values of cross-calibration gain, as all of them were within 1%. In the coastal/aerosol band, there was a maximum offset of approximately 4% between the mean cross-calibration gain values that was more likely due to the spatial uncertainty of Cluster 13. The cluster-based mean cross-calibration gain ratio of SWIR 2 band had an offset of approximately 4% using coincident scene pairs and 2.5% using near coincident scene pair (assuming the cross calibration gain ratio should be 1 as both of the sensors are well calibrated), which was also most likely due to the greater uncertainties in TOA reflectance for these sensors in this spectral region. A similar amount of differences was observed between the cross-calibration gain ratios using the cluster-based approach and the cross-comparison results across all spectral regions [44]. Despite some discrepancy, the cluster-based cross-calibration gain ratio encompassed the cross-calibration gain values obtained by previous cross-calibration works, which implies that the cross-calibration gain ratio obtained from these different approaches are statistically indistinguishable.



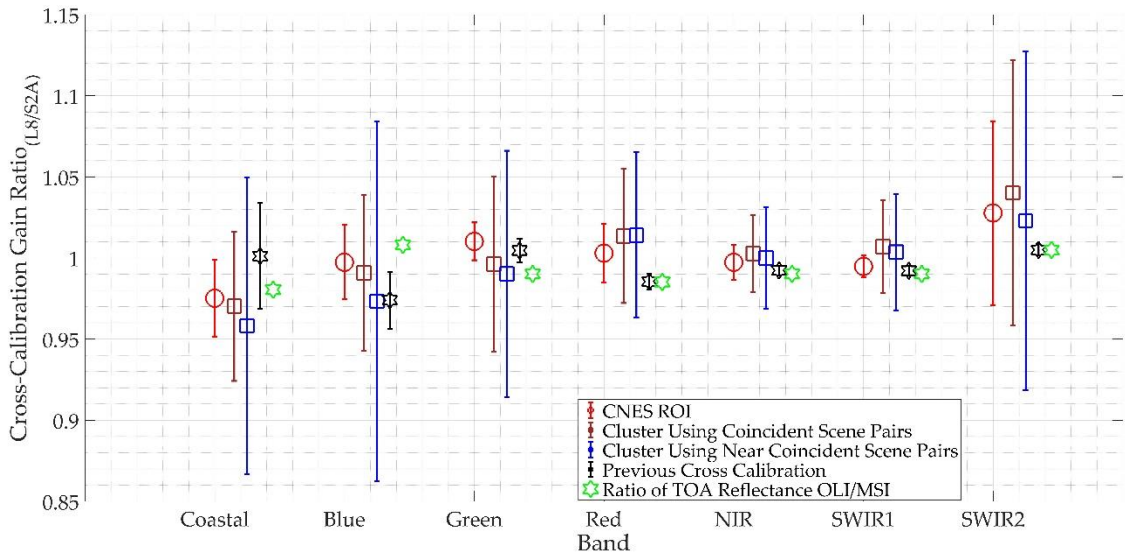


**Figure 15.** Comparison of cluster-based cross-calibration gain ratio with ROI-based cross calibration gain (Uncertainty bars,  $k = 2$ ).

Along with the spatial uncertainty within the Cluster 13 regions, atmospheric uncertainty and uncertainty due to BRDF effects also contribute to the overall cross-calibration gain uncertainty. Atmospheric effects are believed to contribute 1–2% towards the overall uncertainty [28]. The MSI field of view (FOV) was approximately  $20^\circ$  vs  $15^\circ$  for the OLI, and the view zenith angle was approximately  $2.5^\circ$  more than the OLI's ( $10^\circ$  vs  $7.5^\circ$ ); in some extreme cases, the viewing angles could differ up to  $20^\circ$  [45]. Gao et al. [46] concluded that for sensors with narrower FOVs (such as the OLI and MSI), the major BRDF effects result from variation in solar illumination, which is date-dependent. These types of angular effects in TOA reflectance can be corrected, but a narrow angular sampling of moderate resolution sensors complicates BRDF coefficient retrieval, potentially limiting the degree of BRDF correction in the image data, particularly at shorter wavelengths. However, for longer-wavelength bands where atmospheric effects are reduced and BRDF correction is adequate (such as the NIR and SWIR1 bands), the cluster-based calibration gains are more consistent with previously cross-calibration results, despite the greater uncertainty.

From the above discussion, it is clear that the cluster-based calibration gains are comparable to the results of previous cross-calibration works in terms of accuracy but currently exhibit greater uncertainty. This suggests that the cluster-based cross-calibration approach can deliver results consistent with traditional ROI-based cross-calibration results once the uncertainty is properly considered. In addition to efforts to reduce overall uncertainty, future work could include using multiple clusters with varying intensity levels different than Cluster 13 so that both cross-calibration gain and bias can be observed. In order to minimize random noise in the cross-calibration gain ratio, it could be calculated using the lifetime mean TOA reflectance data of both sensors instead of using individual coincident and near coincident scene pairs.

## 5. Conclusions

This article presents the methodology for a cluster-based cross-calibration of optical satellite sensors. The cluster-based calibration uses spectrally similar regions, such as Cluster 13, for finding coincident scene pairs. Since these regions are widely spread across North Africa, it offers a

significantly increased number of cross-calibration opportunities as compared to the traditional ROI-based approach from distinct PICS. The greater number of cross-calibration opportunities helps to average out random errors and estimate more accurately the calibration gains between sensors.

Cluster 13 was chosen to demonstrate the methodology because it has a large number of contiguous regions widely distributed across North Africa and it includes the well-known Libya 4 PICS (CNES ROI) which has been extensively used for radiometric calibration purposes. Two well-calibrated sensors, the Landsat 8 OLI and Sentinel 2A MSI, were chosen as the sensor pair. The comparison was performed using image data acquired in 2017. For these sensors during this time period, Libya 4 CNES ROI offered just three coincident and eight near coincident cloud-free scene pairs; on the other hand, Cluster 13, which includes Libya 4 CNES ROI, offered 11 coincident and 108 cloud free near coincident scene pairs.

The results of this work indicate that, for most bands, a cluster-based cross-calibration approach produces similar results to the traditional ROI-based cross-calibration result. Using coincident scene pairs, the cluster-based cross-calibration gain ratio was within 2% of the gain derived from previous ROI-based cross calibration gain for all bands except the coastal and SWIR 2 bands. The difference in the SWIR 2 band gain was most likely due to greater uncertainty in TOA reflectance of both sensors. Similarly, with the near-coincident scene pairs, the cluster-based cross-calibration gain difference was within 2% for most of the bands but exhibited greater uncertainty, by 2%, than that of the ROI-based method at this time. The greater uncertainty was mainly due to spatial uncertainty within Cluster 13 regions, which was approximately 4% for the coastal band; some of the overall uncertainty was also due to residual atmospheric and BRDF effects. However, despite the greater uncertainty, the cross-calibration gain ratio estimated with the cluster-based approach had similar accuracy with the cross-calibration gain ratio derived from the traditional ROI-based approach.

The use of EPICS clusters can significantly increase the number of cross-calibration opportunities within a much shorter time period. Based on these results, any region within Cluster 13 could, in principle, be used for sensor cross-calibration purposes; the level of accuracy provided by the proposed method is comparable to that provided by the traditional ROI-based method.

**Author Contributions:** M.S. conceived the research and developed the algorithm with the help of L.L. and D.H. M.S., L.L., and D.H. analyzed the data. N.H. generated binary mask to filter in the desired pixel of a cluster. M.S. wrote the paper. L.L. and D.H. edited the paper.

**Funding:** This research was funded by NASA (grant number NNX15AP36A) and USGS EROS (grant number G14AC00370).

**Acknowledgments:** The authors would like to thank Tim Ruggles for editing the manuscript and reviewers for their comments that improved the quality of this paper.

**Conflicts of Interest:** The authors declare no conflict of interest

## Appendix A

In this appendix, we include the RSR comparison of different bands of Landsat 8 OLI and Sentinel 2A MSI.



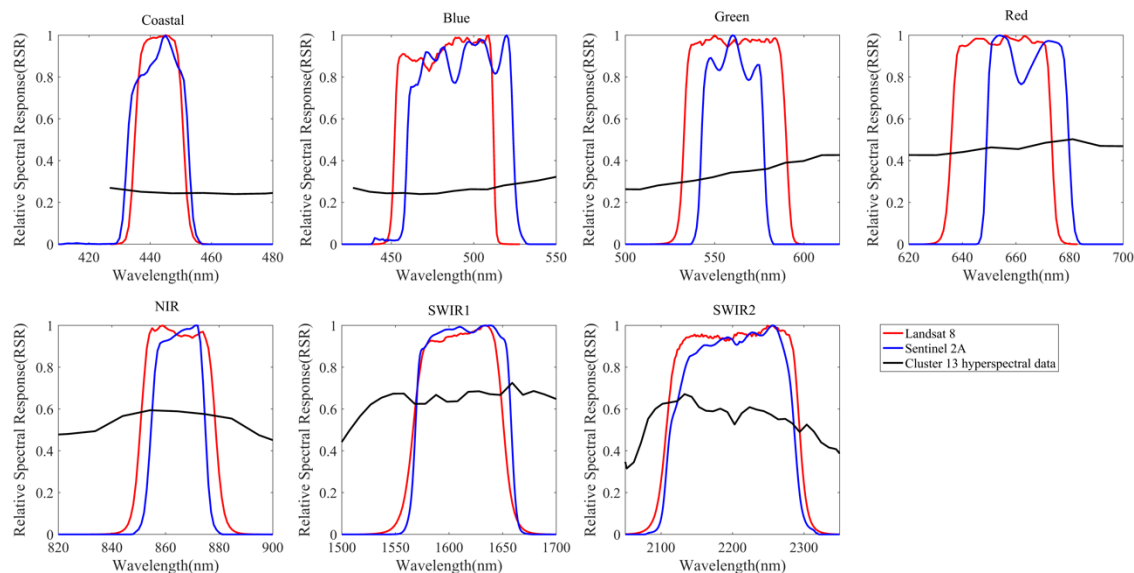


**Figure A1.** Relative Spectral Response (RSR) of Landsat 8 OLI and Sentinel 2A.

## References

2. Slater, P.N.; Biggar, S.F.; Palmer, J.M.; Thome, K.J. Unified approach to absolute radiometric calibration in the solar-reflective range. *Remote Sensing of Environment* **2001**, *77*, 293-303.
3. Dingirard, M.; Slater, P.N. Calibration of space-multispectral imaging sensors: A review. *Remote Sensing of Environment* **1999**, *68*, 194-205.
4. Thome, K.; Markham, B.; Barker, P.S.; Biggar, S. Radiometric calibration of Landsat. *Photogrammetric Engineering Remote Sensing* **1997**, *63*, 853-858.
5. Markham, B.; Barsi, J.; Kvaran, G.; Ong, L.; Kaita, E.; Biggar, S.; Czapla-Myers, J.; Mishra, N.; Helder, D. Landsat-8 operational land imager radiometric calibration and stability. *Remote Sensing* **2014**, *6*, 12275-12308.
6. Slater, P.; Biggar, S.; Holm, R.; Jackson, R.; Mao, Y.; Moran, M.; Palmer, J.; Yuan, B. Reflectance-and radiance-based methods for the in-flight absolute calibration of multispectral sensors. *Remote sensing of environment* **1987**, *22*, 11-37.
7. Thome, K. Absolute radiometric calibration of Landsat 7 ETM+ using the reflectance-based method. *Remote Sensing of Environment* **2001**, *78*, 27-38.
8. Thome, K.J.; Gustafson-Bold, C.; Slater, P.N.; Farrand, W.H. In *In-flight radiometric calibration of HYDICE using a reflectance-based approach*, Hyperspectral Remote Sensing and Applications, 1996; International Society for Optics and Photonics: Bellingham, WA, USA, 1996; pp. 311-320.
9. Teillet, P.; Slater, P.; Ding, Y.; Santer, R.; Jackson, R.; Moran, M. Three methods for the absolute calibration of the NOAA AVHRR sensors in-flight. *Remote sensing of Environment* **1990**, *31*, 105-120.
10. Czapla-Myers, J.; McCorkel, J.; Anderson, N.; Thome, K.; Biggar, S.; Helder, D.; Aaron, D.; Leigh, L.; Mishra, N. The ground-based absolute radiometric calibration of Landsat 8 OLI. *Remote Sensing* **2015**, *7*, 600-626.
11. Teillet, P.; Barker, J.; Markham, B.; Irish, R.; Fedosejevs, G.; Storey, J. Radiometric cross-calibration of the Landsat-7 ETM+ and Landsat-5 TM sensors based on tandem data sets. *Remote sensing of Environment* **2001**, *78*, 39-54.
12. Chander, G.; Angal, A.; Choi, T.J.; Meyer, D.J.; Xiong, X.J.; Teillet, P.M. In *Cross-calibration of the Terra MODIS, Landsat 7 ETM+ and EO-1 ALI sensors using near-simultaneous surface observation over the Railroad*

- Valley Playa, Nevada, test site, Earth Observing Systems XII, 2007; International Society for Optics and Photonics: Bellingham, WA, USA, 2007; p. 66770Y.
13. Chander, G.; Meyer, D.J.; Helder, D.L. Cross calibration of the Landsat-7 ETM+ and EO-1 ALI sensor. *IEEE Transactions on Geoscience and Remote Sensing* **2004**, *42*, 2821-2831.
  14. Cosnefroy, H.; Briottet, X.; Leroy, M.; Lecomte, P.; Santer, R. In *In field characterization of Saharan sites reflectances for the calibration of optical satellite sensors*, Proceedings of IGARSS'94-1994 IEEE International Geoscience and Remote Sensing Symposium, Pasadena, CA, USA, 8–12 August 1994; IEEE: Piscataway, NJ, USA, 1994; pp. 1500-1502.
  15. Cosnefroy, H.; Leroy, M.; Briottet, X. Selection and characterization of Saharan and Arabian desert sites for the calibration of optical satellite sensors. *Remote Sensing of Environment* **1996**, *58*, 101-114.
  16. Bouvet, M. Radiometric comparison of multispectral imagers over a pseudo-invariant calibration site using a reference radiometric model. *Remote sensing of environment* **2014**, *140*, 141-154.
  17. Helder, D.L.; Basnet, B.; Morstad, D.L. Optimized identification of worldwide radiometric pseudo-invariant calibration sites. *Canadian Journal of Remote Sensing* **2010**, *36*, 527-539.
  18. Chander, G.; Mishra, N.; Helder, D.L.; Aaron, D.B.; Angal, A.; Choi, T.; Xiong, X.; Doelling, D.R. Applications of spectral band adjustment factors (SBAF) for cross-calibration. *IEEE Transactions on Geoscience and Remote Sensing* **2013**, *51*, 1267-1281.
  19. Chander, G.; Angal, A.; Choi, T.; Xiong, X. Radiometric cross-calibration of EO-1 ALI with L7 ETM+ and Terra MODIS sensors using near-simultaneous desert observations. *IEEE Journal of Selected Topics in Applied Earth Observations and Remote Sensing* **2013**, *6*, 386-399.
  20. Farhad, M.M. Cross Calibration and Validation of Landsat 8 OLI and Sentinel 2A MSI. Master's Thesis, South Dakota State University: Brookings, SD, USA, 2018.
  21. Pinto, C.; Ponzoni, F.; Castro, R.; Leigh, L.; Mishra, N.; Aaron, D.; Helder, D. First in-flight radiometric calibration of MUX and WFI on-board CBERS-4. *Remote Sensing* **2016**, *8*, 405.
  22. Li, S.; Ganguly, S.; Dungan, J.L.; Wang, W.; Nemani, R.R. Sentinel-2 MSI radiometric characterization and cross-calibration with Landsat-8 OLI. *Advances in Remote Sensing* **2017**, *6*, 147.
  23. Doelling, D.; Helder, D.; Schott, J.; Stone, T.; Pinto, C. Vicarious Calibration and Validation. In S. Liang (Ed.), *Comprehensive Remote Sensing*, vol. 1, pp. 475-518. Oxford: Elsevier. ISBN: 9780128032206. Chapter Title: Vicarious calibration and validation **2018**.
  24. Shrestha, M.; Leigh, L.; Helder, D. Classification of the North Africa Region for Use as an Extended Pseudo Invariant Calibration Sites (EPICS) for Radiometric Calibration and Stability Monitoring of Optical Satellite Sensors. *Remote Sensing* **2019**, *11*, 875.
  25. Shrestha, M.; Leigh, L.; Helder, D.; Loveland, T. Large area Saharan PICS developemnt for calibration and stability monitoring of optical satellite sensors. In *Proceedings of the Pecora 20*, Sioux Falls, SD, USA, 13–16 November 2017.
  26. Gascon, F.; Bouzinac, C.; Thépaut, O.; Jung, M.; Francesconi, B.; Louis, J.; Lonjou, V.; Lafrance, B.; Massera, S.; Gaudel-Vacaresse, A. Copernicus Sentinel-2A calibration and products validation status. *Remote Sensing* **2017**, *9*, 584.
  27. Irons, J.R.; Dwyer, J.L.; Barsi, J.A. The next Landsat satellite: The Landsat data continuity mission. *Remote Sensing of Environment* **2012**, *122*, 11-21.
  28. Mishra, N.; Helder, D.; Angal, A.; Choi, J.; Xiong, X. Absolute calibration of optical satellite sensors using Libya 4 pseudo invariant calibration site. *Remote Sensing* **2014**, *6*, 1327-1346.
  29. Helder, D.; Thome, K.J.; Mishra, N.; Chander, G.; Xiong, X.; Angal, A.; Choi, T. Absolute radiometric calibration of Landsat using a pseudo invariant calibration site. *IEEE Transactions on Geoscience and Remote Sensing* **2013**, *51*, 1360-1369.
  30. Chander, G.; Xiong, X.J.; Choi, T.J.; Angal, A. Monitoring on-orbit calibration stability of the Terra MODIS and Landsat 7 ETM+ sensors using pseudo-invariant test sites. *Remote Sensing of Environment* **2010**, *114*, 925-939.

31. Lacherade, S.; Fougnie, B.; Henry, P.; Gamet, P. Cross calibration over desert sites: Description, methodology, and operational implementation. *IEEE Transactions on Geoscience and Remote Sensing* **2013**, *51*, 1098-1113.
32. Henry, P.; Chander, G.; Fougnie, B.; Thomas, C.; Xiong, X. Assessment of spectral band impact on intercalibration over desert sites using simulation based on EO-1 Hyperion data. *IEEE Transactions on Geoscience Remote Sensing* **2013**, *51*, 1297-1308.
33. Teillet, P.; Fedosejevs, G.; Thome, K.; Barker, J.L. Impacts of spectral band difference effects on radiometric cross-calibration between satellite sensors in the solar-reflective spectral domain. *Remote Sensing of Environment* **2007**, *110*, 393-409.
34. Li, J.; Roy, D. A global analysis of Sentinel-2A, Sentinel-2B and Landsat-8 data revisit intervals and implications for terrestrial monitoring. *Remote Sensing* **2017**, *9*, 902.
35. Hasan, M.N.; Shrestha, M.; Leigh, L.; Helder, D. Evaluation of an Extended PICS (EPICS) for Calibration and Stability Monitoring of Optical Satellite Sensors. Unpublished work, **2019**.
36. USGS Landsat 8 (L8) Data Users Handbook. Available online: <https://www.usgs.gov/media/files/landsat-8-data-users-handbook> (accessed on 25 April 2019).
37. ESA Sentinel-2 User Handbook. Available online: [https://sentinel.esa.int/documents/247904/685211/Sentinel-2\\_User\\_Handbook](https://sentinel.esa.int/documents/247904/685211/Sentinel-2_User_Handbook) (accessed on 5 March 2019).
38. Scarino, B.R.; Doelling, D.R.; Minnis, P.; Gopalan, A.; Chee, T.; Bhatt, R.; Lukashin, C.; Haney, C. A web-based tool for calculating spectral band difference adjustment factors derived from SCIAMACHY hyperspectral data. *IEEE Transactions on Geoscience Remote Sensing* **2016**, *54*, 2529-2542.
39. Bovensmann, H.; Burrows, J.; Buchwitz, M.; Frerick, J.; Noël, S.; Rozanov, V.; Chance, K.; Goede, A. SCIAMACHY: Mission objectives and measurement modes. *Journal of the atmospheric sciences* **1999**, *56*, 127-150.
40. Strahler, A.H.; Muller, J.; Lucht, W.; Schaaf, C.; Tsang, T.; Gao, F.; Li, X.; Lewis, P.; Barnsley, M.J. MODIS BRDF/albedo product: algorithm theoretical basis document version 5.0. *MODIS documentation* **1999**, *23*, 42-47.
41. Roy, D.P.; Zhang, H.; Ju, J.; Gomez-Dans, J.L.; Lewis, P.E.; Schaaf, C.; Sun, Q.; Li, J.; Huang, H.; Kovalsky, V. A general method to normalize Landsat reflectance data to nadir BRDF adjusted reflectance. *Remote Sensing of Environment* **2016**, *176*, 255-271.
42. Liu, J.-J.; Li, Z.; Qiao, Y.-L.; Liu, Y.-J.; Zhang, Y.-X. A new method for cross-calibration of two satellite sensors. *International Journal of Remote Sensing* **2004**, *25*, 5267-5281.
43. Roujean, J.L.; Leroy, M.; Deschamps, P.Y. A bidirectional reflectance model of the Earth's surface for the correction of remote sensing data. *Journal of Geophysical Research: Atmospheres* **1992**, *97*, 20455-20468.
44. Wu, A.; Xiong, X.; Cao, C.; Angal, A. In *Monitoring MODIS calibration stability of visible and near-IR bands from observed top-of-atmosphere BRDF-normalized reflectances over Libyan Desert and Antarctic surfaces*, Earth Observing Systems XIII, 2008; International Society for Optics and Photonics: Bellingham, WA, USA, 2008; p. 708113.
45. Barsi, J.A.; Alhammoud, B.; Czapla-Myers, J.; Gascon, F.; Haque, M.O.; Kaewmanee, M.; Leigh, L.; Markham, B.L. Sentinel-2A MSI and Landsat-8 OLI radiometric cross comparison over desert sites. *European Journal of Remote Sensing* **2018**, *51*, 822-837.
46. Franch, B.; Vermote, E.; Skakun, S.; Roger, J.-C.; Masek, J.; Ju, J.; Villaescusa-Nadal, J.L.; Santamaria-Artigas, A. A Method for Landsat and Sentinel 2 (HLS) BRDF Normalization. *Remote Sensing* **2019**, *11*, 632.
47. Gao, F.; He, T.; Masek, J.G.; Shuai, Y.; Schaaf, C.B.; Wang, Z. Angular effects and correction for medium resolution sensors to support crop monitoring. *IEEE Journal of Selected Topics in Applied Earth Observations Remote Sensing* **2014**, *7*, 4480-4489.



© 2019 by the authors. Submitted for possible open access publication under the terms and conditions of the Creative Commons Attribution (CC BY) license (<http://creativecommons.org/licenses/by/4.0/>).

## Chapter 4: Conclusions

A large number of satellite sensors has been launched to monitor changes on the Earth surface. Thus, the quality of data produced by previous and currently operational sensors is a primary concern, as it critically depends on accurate radiometric calibration for each sensor. PICS based calibration method is one of the most widely used vicarious calibration approach to monitor post launch degradation. Traditionally, only a few locations in North Africa have been used due to the lack of knowledge about the temporal stability of most of North Africa. This work demonstrated the potential of using the whole of North Africa as a continental PICS. This work analyzed each and every pixel of North Africa and found that the majority of North Africa is temporally stable and could potentially be used for radiometric calibration of satellite sensors.

Conventionally, all these pixels were broadly categorized as a “barren” surface type which includes soil, sand, and rock. This work developed a first-ever high-resolution classification of this “barren” surface type of North Africa using Landsat 8 OLI image data and sub classified it into finer classes using an unsupervised classification algorithm. The algorithm identified 19 clusters each representing a distinct surface type having different spectral characteristics. The range of TOA reflectance at shorter wavelengths is narrow, but wider at longer wavelengths which offers a wide dynamic range to calibrate optical satellite sensors.

PICS are widely used for long term trending, cross-calibration and development of absolute calibration model. Accurate hyperspectral characterization of a target is mandatory for performing cross-calibration and developing absolute calibration model as

it is used for generating the SBAF required to compensate for differences in relative spectral response (RSR) between sensors.

This work also presented a methodology to estimate representative hyperspectral profiles for previously derived clusters of North Africa. Cluster 13 was initially chosen to demonstrate the methodology as it possessed the largest contiguous regions that were widely distributed across North Africa. It also exhibited the lowest overall spatial uncertainty across the VNIR and SWIR spectral range, as well as partial inclusion of the well-known Libya 4 and Egypt 1 PICS within its sub-regions. Due to their spatial extent, most of the clusters allowed multiple imaging opportunities per day in contrast to a typical once during the sensor's revisit time. Multiple imaging opportunities obtained through a cluster, or EPICS, approach increases the temporal resolution of a calibration time series which leads to increased sensitivity for quicker identification of changes in sensor response.

The "representative" hyperspectral profile for Cluster 13 in North Africa was estimated for potential use as an extended PICS (EPICS), using 185 hyperspectral profiles derived from 15 WRS-2 Path/Row Hyperion images acquired over its lifetime. The profile exhibited an uncertainty of approximately 5% across all the spectral regions. Most of the rest of the clusters of North Africa exhibit a resultant uncertainty from 5-12%. Among them, Cluster 15 has the lowest resultant uncertainty of 5% whereas Cluster 4 has the highest uncertainty of around 12 %. The major source of uncertainty of the estimated hyperspectral profile is the spatial uncertainty of the cluster itself determined by the threshold used for the initial analysis of the classification of North Africa. In addition,

temporal uncertainty of EPICS, residual BRDF effects, and Hyperion calibration uncertainty also contributed some of the resultant uncertainty.

This work also presents the methodology for a cluster-based cross-calibration of optical satellite sensors. The cluster-based calibration uses spectrally similar regions, such as Cluster 13, for finding coincident scene pairs. Since these regions are widely spread across North Africa, it offers a significantly increased number of cross-calibration opportunities as compared to the traditional ROI-based approach from distinct PICS. The greater number of cross-calibration opportunities helps to average out random errors and estimate more accurately the calibration gains between sensors.

Cluster 13 was chosen to demonstrate the methodology of EPICS based cross calibration. Two well-calibrated sensors, the Landsat 8 OLI and Sentinel 2A MSI, were chosen as the sensor pair. The comparison was performed using image data acquired in 2017. For these sensors during this time period, Libya 4 CNES ROI offered just three coincident and eight near coincident cloud-free scene pairs; on the other hand, Cluster 13, which includes Libya 4 CNES ROI, offered 11 coincident and 108 cloud free near coincident scene pairs.

The results of this work indicate that, for most bands, a cluster-based cross-calibration approach produces similar results to the traditional ROI-based cross-calibration result. Using coincident scene pairs, the cluster-based cross-calibration gain ratio was within 2% of the gain derived from previous ROI-based cross calibration gain for all bands except the coastal and SWIR 2 bands. The difference in the SWIR 2 band gain was most likely due to greater uncertainty in TOA reflectance of both sensors. Similarly, with the near-coincident scene pairs, the cluster-based cross-calibration gain difference was within 2% for most of

the bands but exhibited greater uncertainty, by 2%, than that of the ROI-based method at this time. The greater uncertainty was mainly due to spatial uncertainty within Cluster 13 regions, which was approximately 4% for the coastal band; some of the overall uncertainty was also due to residual atmospheric and BRDF effects. However, despite the greater uncertainty, the cross-calibration gain ratio estimated with the cluster-based approach had similar accuracy with the cross-calibration gain ratio derived from the traditional ROI-based approach.

The use of EPICS clusters can significantly increase the number of cross-calibration opportunities within a much shorter time period. Based on these results, any region within Cluster 13 could, in principle, be used for sensor cross-calibration purposes; the level of accuracy provided by the proposed method is comparable to that provided by the traditional ROI-based method.